MSc Geomatics Graduation Thesis

Filling the white gap on the map

Photoclinometry for glacier elevation modelling

Student:
Ing. Bas Altena

Delft University of Technology
Department of Geoscience & Remote Sensing
Optical and Laser Remote Sensing

Graduation Professor:
Prof. Dr. Massimo Menenti
Supervisor:
Dr. Ben Gorte
Co-reader:
Dr. Andrew Hooper

University of Oslo
Department of Geosciences
Geomatics and Remote Sensing

Supervisor:
Prof. Dr. Ir. Andreas Kääb
Supervisor:
Dr. Christopher Nuth

Executive summary

Keywords: Photoclinometry, Glacier mapping, Optical and Laser Remote Sensing

In this study the limits and potentials of the principle of photoclinometry for glacier elevation modelling is assessed. A combination of optical and laser remote sensing instruments are used to map the surface of different remote ice bodies.

Loss and gain of a glaciers' mass is a good indicator for local climate. If mass-balances of glaciers are known on a world-wide scale, they can give a better understanding of global climate change. Due to the remoteness and harsh environments at which glaciers are located a mass-balance is difficult to maintain or even startup. Therefore, the use of optical and laser remote sensing can be of great value.

The focus of this thesis is to identify options in which optical and laser remote sensing instruments can reliably map the surface of a glacier. It will use the technique of photoclinometry, also known as shape-from-shading, onto optical acquisitions. Estimated surface and topographic information will be integrated with spaceborne laser altimetry. These methodologies will compose a workflow, which produces elevation estimates of a glaciers' surface.

Snow has a homogeneous reflection pattern, therefore the perceived reflection of a surface is primarily dependent on the amount of received sunlight per unit area. In that sense brightness values, perceived by an optical spaceborne sensor, may directly be related to surface orientation. This relation is used in this study to estimate a surface model from an optical image. Estimation of this model is done through the relations of a *Lambertian* reflection function and inverse theory. Only small patches of imagery can be processed, as its estimation is limited in size due to accumulating elevation errors and computational limitations.

The methodology was tested on the high mountain glacier of Zhadang, on the Tibetan Plateau. An optical acquisition from the Earth Observation (EO-1) satellite with the on board Advanced Land Imager (ALI) was used. The estimated surface model was assessed and validated with another elevation dataset and leveling transects from a surveying campaign.

The resulting surface model needs transformation to be of use for elevation modelling. Different strategies are used to resolve the residual unknowns of the transformation. Registration of surface models was conducted on the icefield of Lomonosovfonna,

Svalbard. Laser altimetric measurements from the Ice, Cloud and Elevation Satellite (ICESat) with the on board Geoscience Laser Altimeter System (GLAS) instrument are used for this registration problem. Both geometric and temporal relations are included into the registration model, but only under specific circumstances the registration is reliable.

A profile based approach of photoclinometry is also investigated. It may give topographic correction to resolve errors due to miss-alignment of the ICESat GLAS laser profiler. However, assumptions on terrain geometry were too optimistic to resolve in a reliable correction.

Contents

Map of glaciers in this study

The glaciers measured in this thesis are scattered around the globe. The map below gives an impression of their wherabouts.

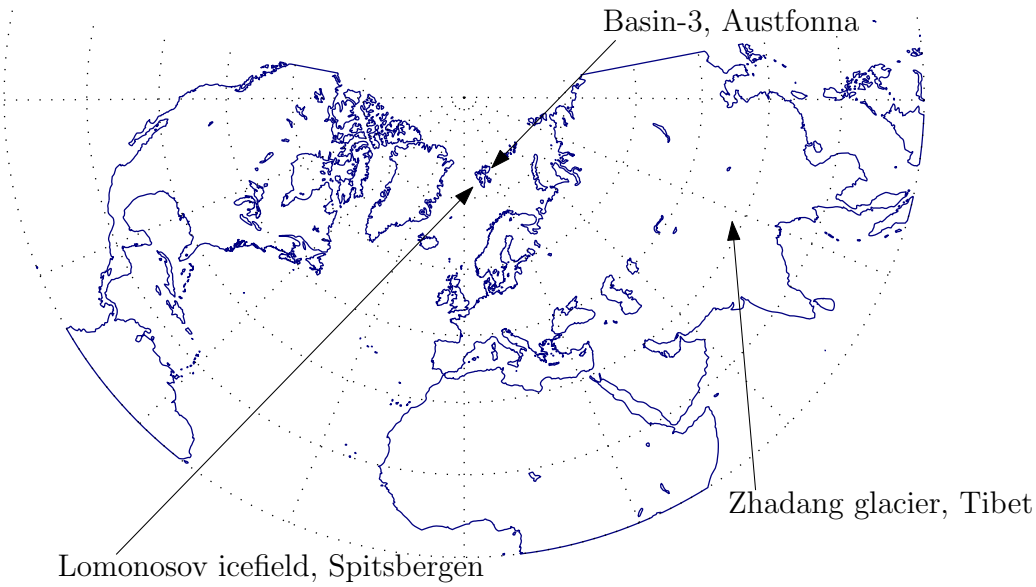

Figure 1: Coastline of the Northern Hemisphere illustrated by a Lambert conformal conic projection.

Chapter 1

Introduction

1.1 Research context

The size and movement of a glacial system are related to climate. A positive contribution of mass is formed by precipitation, avalanches or windblown transportation, while a negative contribution is caused by (basal) melt, evaporation and calving. Especially the precipitation and melting influence of a glacier's budget are climate dependent. If the budget (*i.e.:* mass balance) is not even, the glacier will change its water storage capacity [Cuffey and Paterson, 2010]. The volume response of a glacier can be estimate through a ratio between the representative thickness of a glacier and its mass balance rate [Jóhannesson and Raymond, 1989]. An indication of thickness of frozen hydrological systems is illustrated in figure 1.1.

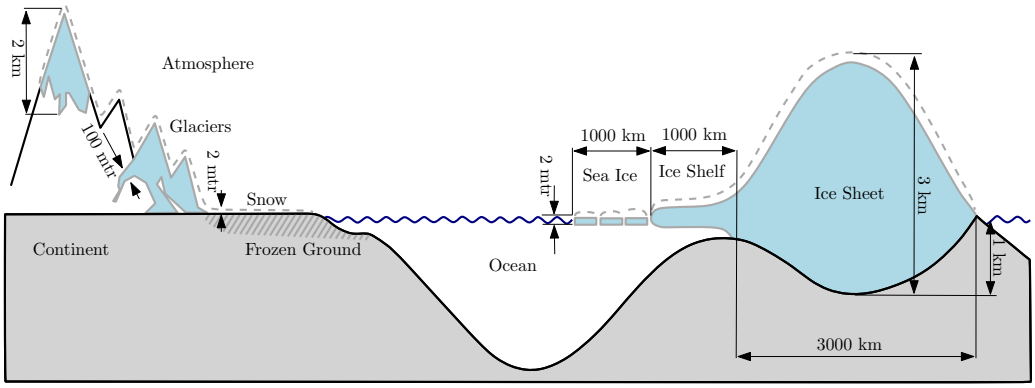

Figure 1.1: Vertical spatial dimension of different snow and ice systems, illustration taken from [Lemke et al., 2007]

As temperatures increase, partly due to the interglacial and the increase of CO_2, this will cause a retreat in glaciers' volume. If the response time is taken into account, one can clearly see that small alpine glacier will melt away more quickly than the large ice-

caps of Greenland and Antarctica. The total water storage of Greenland and Antarctica, is equivalent to an approximate sea level equivalent of 64 meter [Lemke et al., 2007]. Compared to these ice sheets, the contribution of glaciers and ice fields is only a small fraction *i.e.:* 0.15 - 0.37 m. However, these smaller reservoirs are of importance to near future prospects, as their response time is sensitive.

The use of remote sensing helps acquiring a better understanding of the current climatic situation and global glacial processes. Remote sensing instruments can capture a sample over a vast area, within a short period of time. In recent years several satellites have been launched carrying more advanced and precise instruments. By these means it became possible to measure various glacier characteristics and changes in them which otherwise would have been difficult to acquire in the field.

1.1.1 Optical imaging and photogrammetry

The retreating or advancing of a glacier front over time can be a proxy for local climate change. These changes can be mapped by examining the age of moraines in the field, by terrestrial photogrammetry of old photos or even paintings. However the data is biased, being mostly restricted to the European alps [Leclercq et al., 2011]. To obtain a global view of glacier area change or centerline evolution over time, remote sensing is of great value. Initiatives to automate glacier outline detection are still ongoing research [Paul, 2011], but an archive is emerging covering an almost global inventory.

Glacier mapping from space can also be conducted with the use of optical instruments, which follow the principles of photogrammetry. In photogrammetry an acquisition is taken at a certain instance (t_i) with an orientation ($\theta_i, \phi_i, \kappa_i$) and position ($X_i, Y_i, Z_i$). A second acquisition (t_j) is taken from the same scene, but at a different position and angle. These three points define a plane, where the angles (α_P, β_P) and the distance (l_{ij}) to these acquisitions centers is known. The point of interest (P), can then be estimated by solving the collinearity equations. For more details on the subject and its workflow, see [Polman and Salzmann, 1996].

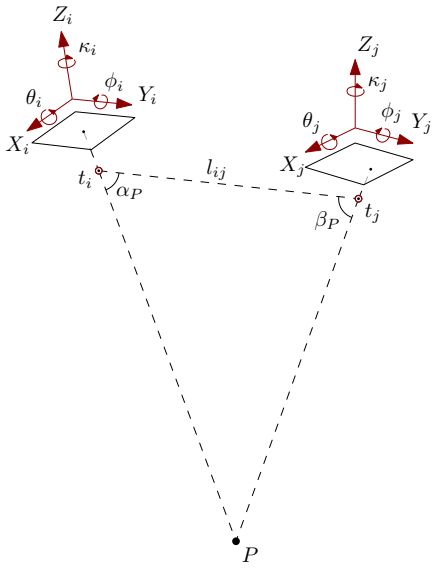

Cameras are used to record an optical acquisition, which resolves in a projection of the observed scene. The point of interest is identified in both acquisitions. Through these measurements it is possible to construct the colinieariy equations. When acquisitions are in digital form, the identification of a point is done through image matching algorithms.

Photosensitive instruments can be saturated if snow is recorded, because its reflectance is high. Only when the gain of these instruments is set less sensitive, will good sampling be possible over snow covered terrain [Raup et al., 2000]. However, these snow covered areas are fairly homogeneous, as the elevation over the terrain is slowly undulating. Then a unique match is not always found. Therefore photogrammetry over snow covered terrain can be troublesome, as is clearly visible in figure 1.2.

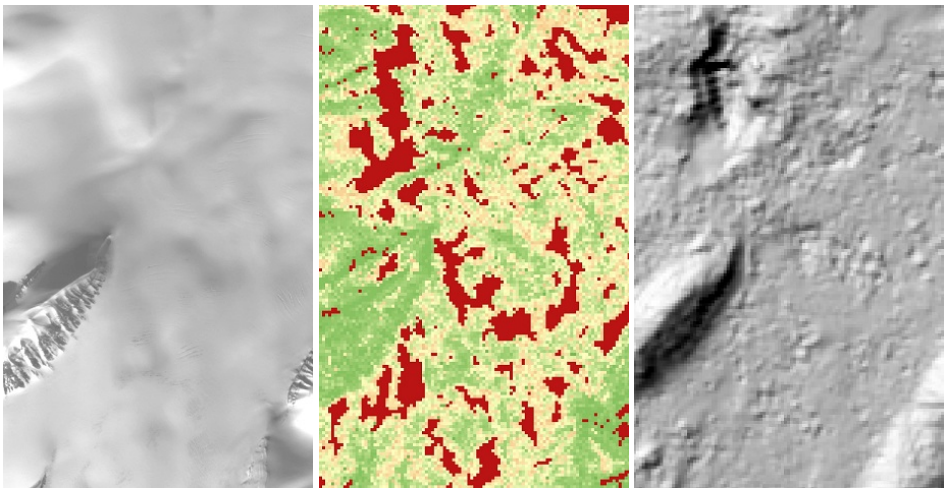

(a) optical image (b) correlation score (c) hillshade

Figure 1.2: On the left hand side is a SPOT acquisition over a small part of Lomonosovfonna, with a small section of a ridge on the left. The image is acquired on the first of September 2007. This acquisition is used together with an other acquisition and photogrammetry to extract a digital elevation model (DEM). Due to the homogeneity of snow reflection, the correlation of each match is not optimal. This can be seen in the illustration in the middle; it highlights the correlation score. It ranges from a low correlation value indicated in dark red, to a highly correlated match in dark green. On the right hand side is a hillshade derived from the DEM, the bumpy pattern in the hillshade are highly correlated with the low matching quality.

1.1.2 Photoclinometry

A closer look at the outer image of figure 1.2 can reveal something about the shape of this ice mass. The observed shading depends on the position of the sun and on the orientation of the local terrain. Oddly enough, two different shapes can be seen, this depends on the position of the sun. If one assumes the sun to shine from the lower part of the image, a ridge is perceived. While a ravine is perceived when the light is assumed to come from the top of the image.

Although image matching fails, there is still usable information within an optical acquisition. The goal of this thesis is to use this information. Photoclinometry is the

method that extracts these inferences. This method may have the potential to complement photogrammetry, or it may be of use as an aid to other remote sensing techniques.

1.2 Research objectives

The objective of this thesis is an explorative study to the limits and potential of photoclinometry for snow covered terrain. Where a methodology is constructed to extract topographic information from a spaceborne optical acquisition. And a procedure is written down to transform this information into elevation estimates that can be of use for glacier elevation modelling, through the use of spaceborne laser altimetry. This objective is formulated into the main research question of this thesis as,

Can elevation measurements of a glacier surface be extracted through a combination of optical and laser remote sensing techniques?

In order to answer the main research question the following subquestions are formulated:

- *What kind of information is needed for glaciological research?*
  Different types of geometric information can be extracted from optical and laser remote sensing instruments. The specification of this information is dependent on the application. Therefore it is of importance to know what information is needed from these instruments. Knowing this, one can specify the type of information and to what extent, how precise and how reliable it should be.

- *Is it possible to derive a unique surface of normals from a optical image of snow covered terrain, through photoclinometry? And what are the preferable circumstances concerning surface characteristics, sun direction and sensor?*
  The subquestion is focused on the amount of topographic information extractable from an optical acquisition. This is of importance for the photoclinometric methodology and the algorithms that will be established in this thesis. The quality of the information content is dependent on the specifications of the components within the workflow.

- *Can additional information from laser remote sensing resolve the ambiguity present in the estimation of a photoclinometric elevation model?*
  Topographic information extracted through photoclinometry may not give all answers needed for glacial research on itself. Complementing this information with other sources may resolve in better or more extractable content. This subquestion focuses on which information is needed to enhance the information content extracted from photoclinometry.

- *Is photoclinometry capable of improving the information content of measurements from a spaceborne laser profiler?*

Information extracted from laser instruments may be difficult to compare with each other or with different geometric data. Consequently, assumptions on the terrain need to be made to overcome problems in, for example, repetitivity and alignment. This subquestion explores the potential of the information extracted from photoclinometry, to spatial and temporal sampling problems.

1.3 Significance

If an adequate mapping methodology is found then it will improve the understanding of the geometry changes of remote ice masses. In that sense, expensive ground truth is not essential to extract elevation changes, due to an independent spaceborne approach. This opens up the possibility to extract elevation changes world-wide. Furthermore the data used may be accessible for low costs, or is even freely available. For example, the ordering of optical imagery of LANDSAT from the archives of USGS[1] is without expenses. Likewise, data from the ICESat GLAS laser campaigns can freely be accessed through NSIDC[2]. In that sense, data is available and can be transformed into useful information.

This study examines the relation between electromagnetic radiation and topographic surface orientation. Only snow surfaces are considered. However if this approach is sufficient, its methodology may be extended to different reflecting surfaces. Furthermore, this study investigates the possibilities of modelling the dynamic surface of a glacier. However other earth surfaces may have similar behavior, *e.g.*: subsidence, in that sense the methodology may also be of use in these fields.

Image matching algorithms in photogrammetry use an area of several pixels wide and long. Consequently, it estimates elevations in a grid with a wider spacings. Inclination information used by photoclinometry can be on an individual pixel basis, in this sense photoclinometry can complement photogrammetry. It can give additional information, increasing the spatial resolution [Kirk, 1987].

Currently, methods exist that can compare elevation differences from spaceborne laser profilers for glacial surfaces. However, their limitations are found in the small selection of usable measurements, for example with crosstracks [Slobbe et al., 2008]. Alternatively assumptions can be made about the terrain characteristics, such as, for example, that the ice surface is locally close to planar [Moholdt et al., 2010b]. The help of other elevation products for topographic correction can be used, e.g.: [Moholdt et al., 2010a], but not everywhere in the world these elevation products have a good spatial detail to be used in a sufficient manner. The method in this study has the potential to extract a more precise estimate of glacial elevation changes. It may not be limited to crosstrack overpasses, or dependent on other geometric data sources.

The measurement campaigns of ICESat GLAS profiler occurred between 2003 and 2008. Its applicability could be found in short term glacial geometry changes. One can think of processes such as surging or glacial outbursts and drainages. For processes with more slowly changing characteristics this technique could also be of use. However,

[1] http://earthexplorer.usgs.gov
[2] http://nsidc.org/data/icesat/order.html

other campaigns should be included to extract a significant signal, for example, the new ICESat2 mission could be included. This follow-up satellite mission is planned for the beginning of 2016. Furthermore the method can be used to do analysis backwards in time. Old campaigns like the SLA-2 mission from 1997 could be used. Unfortunately this experimental mission had sparse global coverage, and only a limited amount of ice-masses can be included in such a study. This thesis aims to construct a general method to conduct such analysis. The benefit is found in its wide applicability as it is not bound to a certain constellation of instruments.

1.4 Structure

The structure of this work will be as follows, at first an overview of the processing chain of this work is given. It will introduce the different sensors, the reflection properties of snow and the final glaciological implementation. Chapter 3 gives an overview of the different computational methods that are of help for the proposed methodologies. These are used in chapter 4 to describe the implementation of several ideas. Result of these implementations are given in chapter 5, and this work finishes with conclusions and recommendations.

Chapter 2

Research approach

The workflow used in this study is illustrated in figure 2.1. The first component of the workflow is the acquisition of data by a sensor, in this case a spaceborne remote sensing instrument. The acquired data need to be processed: a transition needs to be made from sensor readings to geometric data. This is done through relations that link different physical processes and properties to each other. The last chain in the workflow involves the transformation of geometric data into sensible information for a given application.

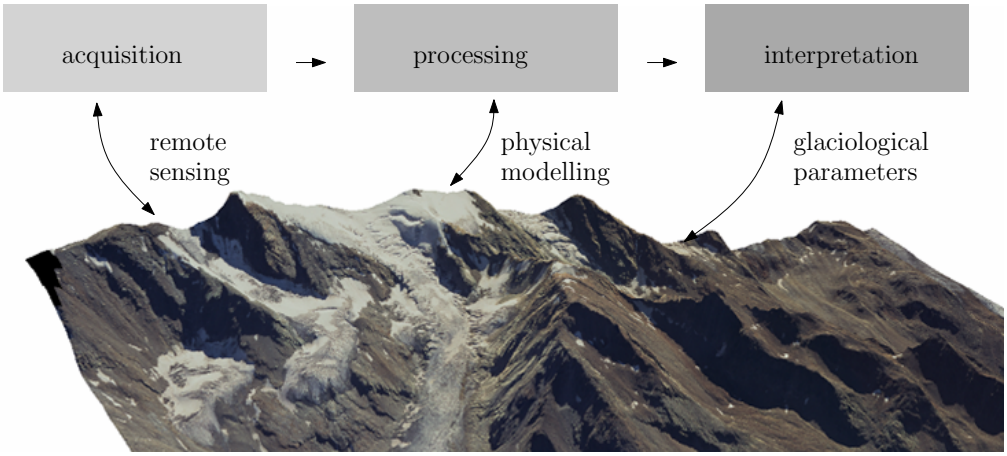

Figure 2.1: Geomatics workflow used in this work, in the background an aerial image is draped over a elevation model of Gruben glacier, Switzerland.

In this section the components of the workflow will be described more closely. It will highlight remote sensing instruments, then reflection properties of snow and finish with glaciological parameters.

2.1 Acquisition

The instruments used in this study are mounted on satellite platforms, orbiting the earth. There are two different satellite instruments used in this study. An active case, where an instrument can send a signal and measure its reflection. And a passive measurement set up, where the instrument measures another energy source.

2.1.1 Optical Instruments

Optical instruments measures the radiometric energy that is received by their photo sensitive area. The instrument has an optical system similar to a normal camera, with lens and focal plane. But the photo detectors have a different spectrum and configuration. Incoming photons enter the detector and cause an electric signal. The amplitude of the signal is related to the amount of photons. Their spectral response is in the visible- till thermal infrared parts, *i.e.:* wavelength of $\approx 0.1\mu\text{m} - 10\mu\text{m}$.

The acquisition of reflections of the surface can be done in different configurations. One photo sensitive element can be used, and a mechanical mirror sweeps perpendicular to the track. This case is called a whiskbroom configuration. Multiple photosensitive elements can be aligned into an array, and placed cross-track to the flight path. In this case the sensor has a pushbroom configuration, figure 2.2 illustrates this example. In both configurations this results in a recording of a linear portion of the earth surface. Which is usually oriented perpendicular to the direction of motion of the satellite platform. Subsequent recordings of multiple lines leads to coverage of a surface area.

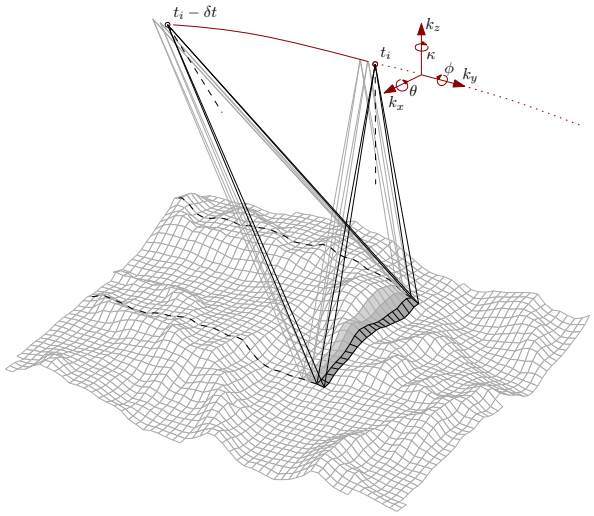

Figure 2.2: Schematic view of a pushbroom sensor with multiple viewing angles and multiple channels, illustration taken from [Kääb, 2005].

Sensors measure the radiation within a small fraction of the spectrum. Energy re-

ceived on the sensor is collected and registered onto a digital scale. Its range is depend on the bit length, but the radiometric range is mostly 2^8 or 2^{12}. The sensitivity of the sensor is adaptable in modern instruments, thus there are mostly several operation modes, that adjust to the energy input.

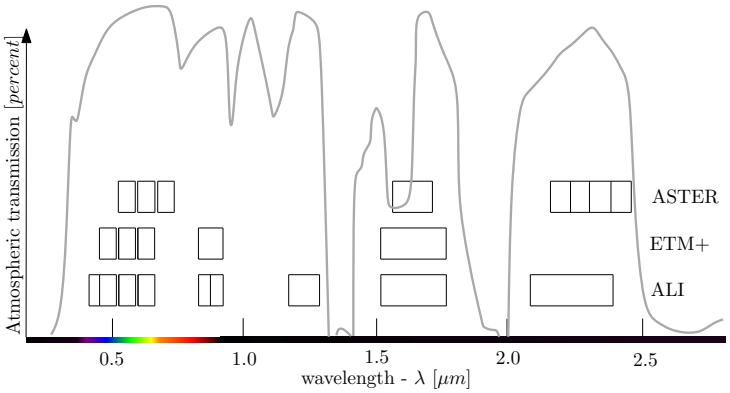

Figure 2.3: The ratio of electro magnetic transmission through the atmosphere in respect to its wavelength. Superimposed on the figure are the bands of several optical instruments on board of low orbiting satellite platforms (stacked: eo1, landsat & terra). Illustration taken from [Kääb, 2005].

Apart from a spatial resolution, the relation between ground coverage and pixel element, there are other specifications. The spectral resolution is the interval of measured radiation within the frequency domain. A specific domain of frequencies is detected by the CCD elements of the instrument, as illustrated in figure 2.3. These bands may not be too narrow, as there is a physical limit on the amount of radiative energy entering the sensor. Instruments with a narrow spectral band, will have a relatively wide spatial resolution.

The temporal resolution is the revisit time of an acquisition system. For which the orbit flown by the satellite is most important. This revisit frequency can increase if the swath width is large, or if the looking angle of the instrument is adjustable. In this manner the BRDF of surfaces can be measured from space. The platforms used in this study have sun-synchronous orbits, which results in a revisit time of approximately sixteen days, see table 2.1.

vehicle	instrument	type	bands	spatial res. [m]	swath [km]	radiometry [bit]
Terra	ASTER	pushbroom	9	15	60	8
Landsat	ETM+	whiskbroom	8	30	185	8
EO1	ALI	whiskbroom	10	30	37	12
ALOS	PRISM	pushbroom	1	2.5	35	8

Table 2.1: properties of different remote sensing platforms and there optical instruments

2.1.2 Laser ranging instruments

Active sensors send a signal, and the time of flight until the reflection returns is measured. This precise time interval (t) is transformed to physical length (d) by the speed of electromagnetic radiation (c);

$$d = c \cdot t \tag{2.1}$$

Each measured time interval can be transformed to a distance measurement. If in addition to that, the position and rotation angles of the instrument are known. It will be possible to calculate the three dimensional coordinate of the point at the surface where the laser beam was reflected.

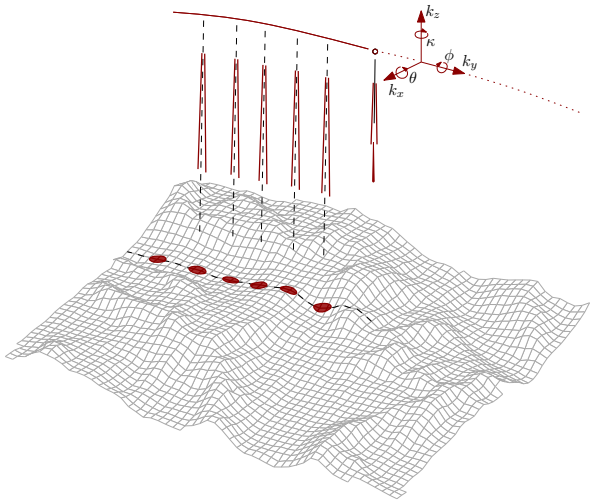

Figure 2.4: Schematic view of a laser altimeter in profiling mode, illustration taken from [Kääb, 2005].

The configuration of a laser profiler is illustrated in figure 2.4. Most range systems send out pulses in a regular repetition. This results in a resolution, that is related to the flight velocity above the surface and the pulse repetition rate. Simple space or airborne laser altimeters use a threshold on the received energy to pinpoint the time of flight. But the sampling can also be done by a waveform digitizer, in this way more information is collected. The relation above can be refined, as techniques evolve and more specifications can be included. For example, the acquisition processes can be seen as a convolution of the transmitted waveform, its footprint, and its pulse length. Then, the geometric and reflectance properties, and at last the atmosphere follow. If these components are included into a model, more specific information can be extracted. By modeling these building blocks, it is possible to isolate other information, from within the signal.

Thus a laser altimeter measurement can be seen as a convolution. First the laser produces a very high energy pulse. This power is released within a few nanoseconds. Ideally, the waveform should have a steep start and ending, aiming on a block-shaped

waveform. Unfortunately this is technically very difficult, thus the waveform is more similar to a bell shape.

Apart from the time dependent element, there is also a spatial element of importance. This is the beam profile of a laser, and it gives the spatial coverage of its energy distribution. It depends on the pump source, the optical resonator, and the laser medium [Stilla and Jutzi, 2009]. They are modeled as a two dimensional elliptical Gaussian.

Then the geometric properties of a surface deforms the waveform, while its reflectivity reduces the intensity of the waveform. The reflectors that compose the waveform are weighted samples equally scattered throughout the footprint. However the reflectors are mostly the first encounters, thus one should take into account that the top surface is measured. For glacier mapping this is of minor importance, as vegetation is absent.

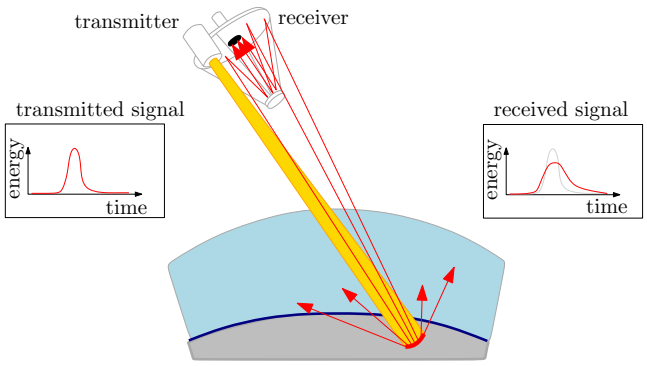

Figure 2.5: Schematic overview of a spaceborne laser ranger, credit ESA.

Spaceborne laser profilers are relatively new instruments. The first spaceborne measurements were trial flights on board of Space Shuttles, but in recent years some laser profilers have been launched, and will be launched. A few examples of spaceborne laser profilers are given below.

vehicle	instrument	inclination [*deg*]	height [*km*]	footprint [*mtr*]	prr [*Hz*]	vertical sampling [*mtr*]
Discovery	SLA2	57	278	100	10	0.75
ICESat	GLAS	94	600	70	40	0.15
CALIPSO	CALIOP	98	705	100	20.25	30

Table 2.2: properties of different remote sensing platforms and there laser ranging instruments, taken from [Carabajal et al., 1999], [Duong, 2010] & [Hunt et al., 2009]

2.2 Processing

The second component within the workflow consists of the processing of remote sensing measurements to geometric data. For this study it will involve optical acquisitions in the form of raster data and meta data for photoclinometry, as well as, point samples from the laser profiler. This section will start by highlighting the reflection pattern of snow in the visible spectrum, followed by an overview of methods using the photoclinometric principle.

2.2.1 Optical properties of snow

States of snow Snow is precipitation of star-like ice crystals, grown from water vapor. Snow crystals have various morphologies, where the temperature during formation, is the main factor of influence. Fresh precipitated snow is highly porous, and has fragile bindings. If temperature conditions are well below the melting temperature of ice, crystals are highly branched. They will undergo fewer transformations, thus this dry snow condition will result in a highly spaced snow pack. This low density material has a high reflectivity, due to easy penetration of radiative energy.

If conditions are close to the melting point of ice, the snow crystals exhibit more metamorphism. Decaying processes already start when a snow crystal hits the ground. The branches of the crystals disappear, and the crystal changes to a grain-like structure. The rate of this process is mostly influenced by both temperature and compression of the pack. Through time the optical properties change, where consecutive melt and freezing are most influential. The size of snow crystals or grains ranges from 50 μm for fresh snow, growing to 1 *mm* for melting old snow [Wiscombe and Warren, 1980].

Radiometric interaction Electromagnetic energy has three different interactions with matter, being absorption, reflection and transmission. The amount of absorption into media is dependent on the permittivity and permeability of the subjected matter. Permeability can be left out of the equation, as the relative magnetic permeability of snow is roughly equal to that in free space. Absorption is best related through the dielectric constant (ϵ). However this constant is dependent on wavelength. A wave with a certain wavelength (λ) travels through a medium, the wave will reduce the intensity of its amplitude. The absorption length is the distance a wave travels until it is reduced by a factor *e* ($\approx 2,718$), for a physical description see [Rees, 2001].

The other interactions concern the reflection and transmission of energy through matter. This reflection boundary phenomena is covered by *Snellius* law:

$$n_{\lambda,i} \cdot sin\theta_i = n_{\lambda,e} \cdot sin\theta_e \tag{2.2}$$

Where the subscript i denotes the incidence and e the exitance, while θ is the angle. The two homogeneous media have a refractive index n_λ, where $n_\lambda^2 = \epsilon_\lambda$. However one can imagine that reflection modeling of snow, can become very complex within a few

reflection steps. The exotic shapes of snow crystals, and the low absorption rate, make the interactions accumulate rapidly, resulting in complex volume scattering.

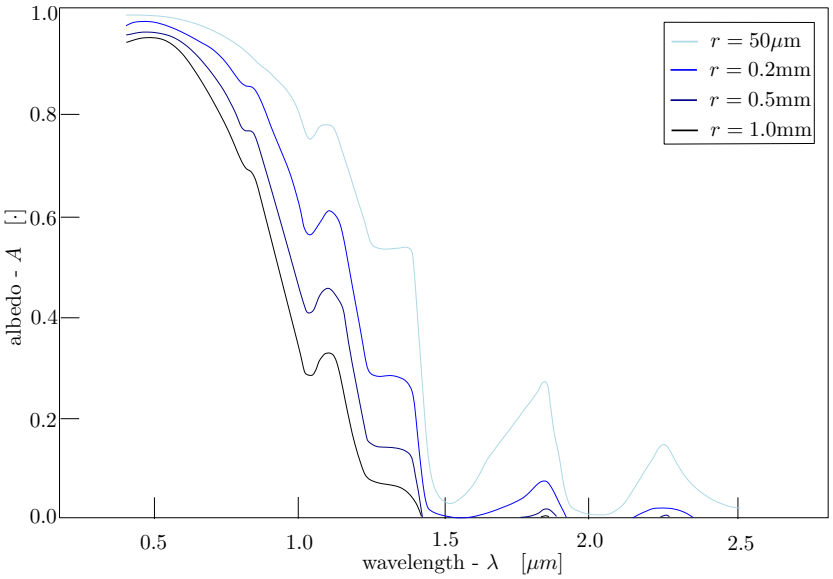

Figure 2.6: The reflectivity of snow within the spectrum, as a function of grain size. Illustration taken from [Rees, 2006]

Grain size is a main component that influences the amount of reflection, as can be seen in figure 2.6. Although the principle shape in this graph is rooted from the dielectric constant, the influence of grain size is relevant in certain parts of the spectrum. Looking at the reflectivity in general, there are mostly high values in the visible spectrum, and it has its maximum at 0.46 μnm. The small decline later on, results in the white, though blue tinted perception of snow by the human eye.

Bi-directional reflectance distribution function Apart from influences by grainsize, another component of great importance is the direction of incidence and exitance of energy. This relation is known as Bi-directional reflectance distribution function (BRDF). It is the ratio (ρ) between incoming (E) and outgoing (L) radiance at certain angles [Warren, 1982];

$$\rho(\theta_i, \phi_i, \theta_e, \phi_e, \lambda) = \frac{L(x, y, \theta_e, \phi_e, \lambda)}{E(\theta_i, \phi_i, \lambda)} \tag{2.3}$$

The spectral albedo is defined as the integral of the BRDF over the upper hemisphere of the surface, *i.e.:* all exitance angles, given as [Dumont et al., 2010];

$$A(\theta_i, \lambda) = \int_0^{2\pi} \int_0^{\pi/2} (\rho(\theta_i, \phi_i, \theta_e, \phi_e, \lambda) \cdot cos\theta_e \cdot sin\theta_e) d\theta_e d\phi_e \tag{2.4}$$

The influence of volume scattering on albedo is illustrated in figure 2.7. It shows that, if energy comes in at a low incidence angle, it can escape more easily to the surface. An ascendancy of incidence angle becomes clearly noticeable starting from wavelengths greater than one micrometer. Visible wavelengths penetrates up to half a meter into the pack. However only the upper five to ten centimeters have a prominent effect on the signal [Zhou et al., 2003].

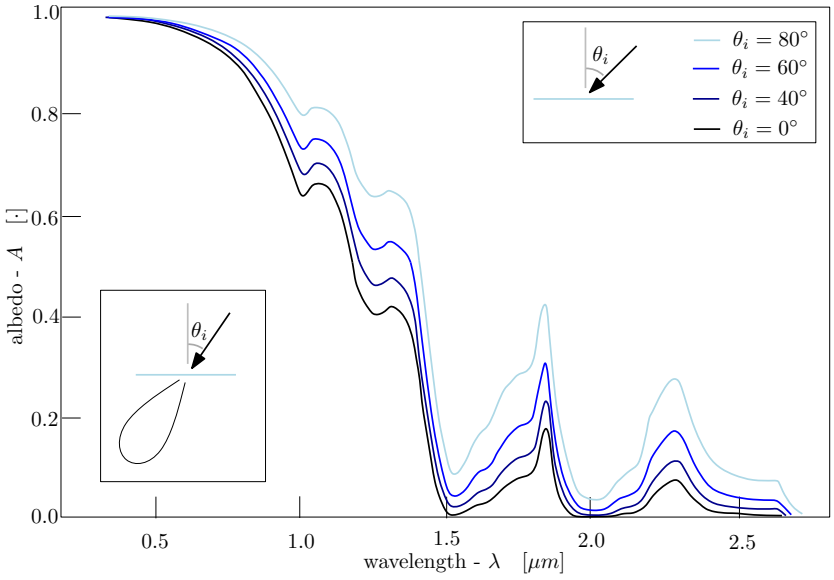

Figure 2.7: Albedo of a snowpack with a mean grainsize of 100 μm. Colors represent different incidence angles of illumination. Illustration taken from [Warren, 1982]

Uni-directional reflection The effect of liquid water in snow is similar to an increase in grain size. This minor effect is due to the high similarity of refractive index between water and snow, within the visible spectrum. [Steffen, 1987] measured the BRDF in the range of 0.5 - 0.6 μm, for different snow types. They found that powder snow had a nearly isotropic reflectance, while new and old snow showed forward scattering. A measure for the anisotropic reflection pattern of snow is illustrated in figure 2.8.

The configuration of reflection of snow is measured in a high radiometric resolution by [Peltoniemi et al., 2005]. They found a strong forward spike in the principle plane of the sun, smoothing to its azimuths, close to a bowl shaped BRDF, as can be seen in figure 2.9.

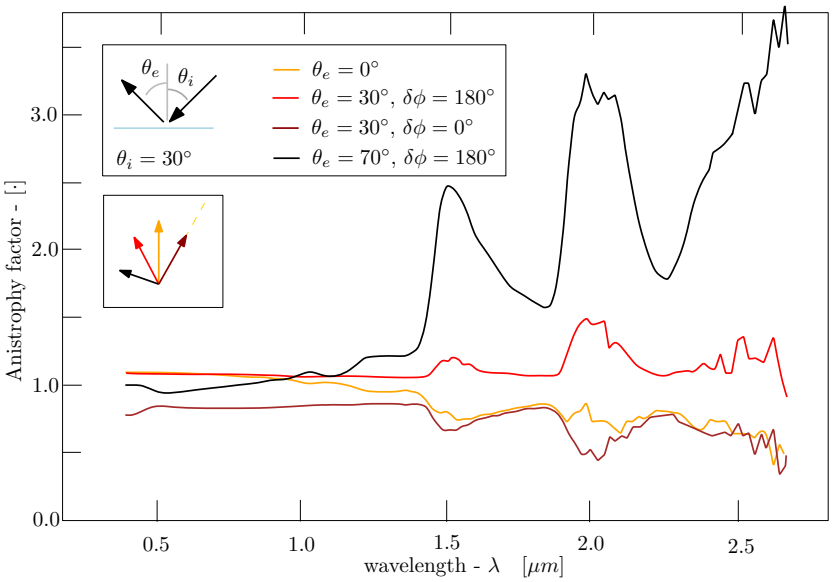

Figure 2.8: The anisotropy factor is a normalized BRDF value. This factor is the BRDF divided by the albedo, multiplied by a constant. When the anistropyfactor is at unity, it describes a *Lambertian* reflection function. The graph is the result of measurements from a sample of new wet snow, illustration taken from [Dumont et al., 2010]

Snow transport The effect of aging snow is not the only component that influences the reflection function. Wind is a complex component that transports vast amounts of small snow grains. A blizzard, which is a combination of hard winds with heavy precipitation, can form snow dunes that can be as big as ten meters. But apart from these dramatic events, wind is gradually transporting snow grains most of the time. For alpine areas wind is chilled by the glacier ice, it builds up, and in the afternoon result in katabalic winds, blowing downstream.

On a smaller scale, topographic features are fairly similar to sand dunes. Snow is taken from the windward side and deposited on the lee side. At the windward side sastrugi can emerge. They are made by the wind, that carves into the snowpack. This happens when the snow surface is harder than its underlying layers, and the wind is strong enough. At the lee side ripples can emerge, these features are smaller in magnitude, and its effect on reflection can be neglected.

Surface roughness like, windblown features and sun cups have a strong directional component. Measurements of their influence on the BRDF has been assessed [Warren et al., 1998], [Mondet and Fily, 1999]. Roughness in the terrain result in form shadow and cast shadow. Especially cast shadow reduces the forward scattering, this phenomena is at its maximum when the sun is perpendicular to the sastrugi. If the sun angle is in an intermediate configuration perpendicular or parallel to the sastrugi, the reflection pattern becomes asymmetric. However in nadir view, most of these effects are of less significance.

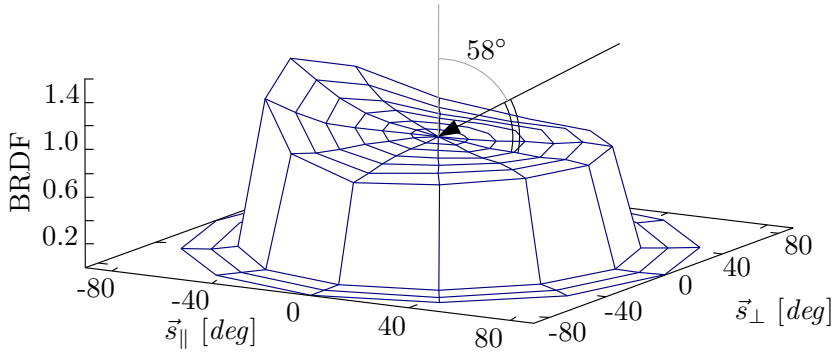

Figure 2.9: Plot of BRDF measurements of loose snow with a wavelength of 0.56 μm, the black arrow indicates the sun incidence vector. The illustration is taken from [Peltoniemi et al., 2005].

The reflection pattern may be corrupted by other matter. Except from water there is dirt, *e.g.*: dust particles, industrial pollutants or red algae, within the snow pack [Dozier and Painter, 2004]. This interference is most notable in wavelengths smaller than one micrometer.

2.2.2 Photoclinometry

The intensities within an optical satellite acquisitions are the effect of interplay of several components, being: geometry, reflectance, illumination and viewpoint. Most of these components can be approximated by models that are based on *e.g.:* satellite ephemeris, reflection modelling, physical constants. The geometry of the terrain is unknown, but if this component can be isolated, it is possible to use the relation of photoclinometry to estimate it. Photoclinometry is a composition of three Greek words, namely *phos* meaning light, *clino* meaning slant and *metron* meaning measure. It directly relates the dependency of incidence angle to surface gradient. The surface gradient of different pixels can directly be used or integrated into elevation measurements. The extracted information from this principle can be in three different dimensions, namely point, profile or area. These three concepts and methodologies are highlighted below;

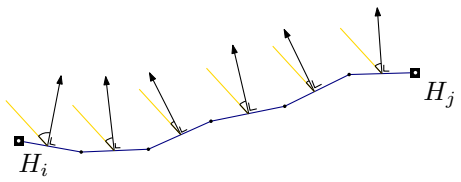

Point samples The intensity value depends on the relative angle between the sun vector and the normal vector of the terrain. When the steepest slope of a surface is in the

direction of the sun, intensity values may directly be related slope. Slopes with another azimuth will be projected on this solar plane. Consequently, the estimated slope will be shallower than the real surface. For a reliable estimate, the topography needs to be simple and its main change oriented in this direction. If this condition can be satisfied, an optical acquisition can give an idea of the surface roughness [Beyer et al., 2003].

Profiles Slope estimates, as described above, can be used to estimate a profile along the suns' direction, a photoclinometric lane. Cumulation of aligned integrated slope estimates along this lane give a elevation profile. Each elevation estimate will have an error, due to the model and measurement noise. Through the summation of these elevations errors will accumulate.

Area Aggregation of neighboring photoclinometric lanes result in a surface. The discrepancy in azimuth does not occur as more orientations can be chosen. Ambiguity in the azimuth direction exist, however this may be solve as a smooth surface is estimated. Conceptually the area based method is simpler, however an increase in computational power is proportional to the size of the sampling area. Multiple methodologies exist to resolve the azimuth ambiguity.

The relations between the reflection function and small variations in height should be known in order to explain the small variations in brightness. If these relations are given, the help of an initial curve can give all ingredients to estimate shape. This is the approach for photoclinometry through characteristic strips [Horn, 1990].

For implementation of this approach, it is necessary to search for situations where the function is zero. Thus, where the normal and sun vector have the same direction. The method assumes a sun vector parallel to the viewing direction. In that sense it is easier to formulate the differential equations. Consequently, the characteristic strips will have the same elevation. From these initial curves, integration in an outward direction will result in an estimate. However this method is very sensitive to noise, and there is propagation of errors along its curves.

Using the calculus of variations, a condition can be added to the problem statement. This condition restricts the outcome, resulting in one solution. For shape recovery, this condition is mostly stating a curvature constraint. Thus the function that minimizes the overall curvature is sought. In the field of calculus of variations, the aim is in finding an extreme of a functional [Sagan, 1992]. A functional is a collection of functions. Thus the function that minimizes a quantity, here curvature, will be selected.

2.2.3 Laser altimetry

Laser technology can operate in different configurations, *e.g.:* ranging, profiling or scanning. The raw measurements that result from a campaign can be used in two manners. At first the geometrical properties can be used, making use of the ranging principle. Or

the reflection of the received signal is interpreted, by analyzing the scattering response. These different interpretations can be applied on different scales, the following sections will give a brief overview of these. Where the main focus will lay on the implementation of spaceborne instruments.

Full waveform An individual laser range measurement is a waveform that describes the received energy of a reflected pulse over time. It is a convolution over time of the transmitted pulse, atmospheric absorption, reflection and instrument sensitivity. Apart from the time domain, the spatial construction of the sensor and the configuration of the sensed objects are also part of the final waveform.

An experimental laser profiling mission on board of the space shuttle *Endavour* on January 1996, was one of the first full waveform campaigns in space. The echoes showed correspondence with vegetation cover, reflectivity, influences of slope and ruggedness. Thus inferences from the waveform itself could be made [Garvin et al., 1998]. With the GLAS instrument on board of ICESat these correspondences were taken further, and classification based on the waveform, was showed to be possible [Duong, 2010], [Molijn et al., 2011].

Information of a phenomenon can be extracted if that specific component can be isolated. First instrumental properties need to be extracted from the metadata, and the atmospheric absorption should be modeled. Then it is possible to address the energy variation over time to geographic features, or reflection properties.

Due to the high precision in orientation parameters (*i.e.*: attenuation and flightpath of the satellite) of ICESat, its sampled location on the earth surface can be estimated within a range of two arcsec. For the vertical accuracy, there is a vertical sampling precision of 15 centimeter, with a range bias that can be as low as 2 cm [Martin et al., 2005]. This makes it possible to extract withinfootprint characteristics. Most research in this approach is found in biomass parameter estimation, such as vegetation height and crown depth [Harding and Carabajal, 2005].

Point samples A waveform can be too specific for certain applications, thus laser data can be processed to extract a more generic product. In that case, the waveform is fitted with a Gaussian curve, to extract the centroid of elevation. Dependent on the terrain characteristics, different approaches can be chosen, *i.e.*: amount of fitted gaussians. These products can than be used to evaluate changes in the terrain, for example lake levels [Zhang et al., 2011] .

Profiles The individual samples are aimed along a reference track, sampling a profile along the terrain. These tracks are repeated, so comparison along the profile can be made. Changes within this plane could be extracted in that manner.

Technology is emerging, and with ICESat-II a more advanced laser profiler will come into orbit, at the beginning of 2016 [Abdalati et al., 2010]. However more advanced in-

struments have already been tested, which use a flash LIDAR. These instruments have an array of receivers instead of a single antenna, thus both imaging and ranging capabilities are possible [Ramond et al., 2011]. This will improve the spatial sampling of the terrain, making it easier to extract information.

2.3 Interpretation

The next step in the workflow consists of transforming the geometric data derived from the sensors to usable information for glaciological study. Therefore a relation need to be establish between geometry and glacier dynamics, describing the influencing factors of a glacial system.

The mass of a glacier changes through time. Accumulation of water is added to the system through avalanches, wind transport, and precipitation. Ablation is caused by melt, calving discharge or evaporation. These processes occur independent of each other. The net balance at a given time is the sum of gain and loss of these processes over a given point. Accumulation and ablation is effected by seasonality, this results in a cyclic behavior for the net balance. A balance year is the time between two minimums, it is variable over space and time and therefore difficult to formalize. Measurements are typically conducted at the end of the winter season (t_m), and at the end of the summer season (t_i). The net balance for any point on the glacier is the integral of the accumulation rate ($\dot{c}$) plus the ablation rate ($\dot{a}$) over that period. For a measurement campaign of summer and winter balance, the net balance is given by [Paterson, 1994]:

$$b_n = \int_{t_1}^{t_m} (\dot{c} + \dot{a})dt + \int_{t_m}^{t_2} (\dot{c} + \dot{a})dt \tag{2.5}$$

The pattern of these rates are different from point to point. However the factors that influence these patterns are partly known. For example, elevation is a principle component, as in the lower part is relatively more mass loss. Fortunately there is flow of ice, due to gravity, from higher parts to compensate for this local loss.

The net balance is an integral over the production term (β), but does not incorporate the dynamics within a glacier. However if surface measurements are differenced from each other they include a dynamic signal. This is seen, if a glacier is expressed as a system that has a conservation of mass. Every element within the glacier has density (ρ), and velocity ($\vec{u}$). For every element the continuity equation states [Paterson, 1994];

$$\frac{\partial \rho}{\partial t} + \nabla \cdot (\rho \vec{u}) + \beta = 0; \tag{2.6}$$

If this relation is taken over a whole column, the equation should be integrated from the surface height (h_s), down to the bottom height (h_b). Integration of the production term results in a composition of the surface net balance (b_s) and the basal melt (b_b). The velocity term transforms into a flux ($\nabla \vec{q}$) [Nuth et al., 2012];

$$\frac{\partial h}{\partial t} = \frac{\partial}{\partial t}\int_{h_b}^{h_s}(\rho)dz = b_s + b_b + \nabla\vec{q} \tag{2.7}$$

If elevation changes over the entire glacier surface (A) are known, then these changes can be related to volume changes. This is done through multiplication with the density of ice (ρ), resulting in volume change in water equivalent units;

$$\frac{\partial V}{\partial t} = \int_A (\frac{\partial h}{\partial t} \cdot \rho)da \tag{2.8}$$

If the other terms in equation 2.7 are also integrated over the whole glacier area, it is possible to relate volume change to the climatic-basal mass-balance (B) and its flux divergence ($\nabla\vec{\hat{q}}$) [Cogley et al., 2011];

$$\frac{\partial V}{\partial t} = \frac{1}{A} \cdot B + \int_A (\nabla\vec{\hat{q}})da \tag{2.9}$$

The measurements from photogrammetric or photoclinometric elevation estimates are point measurements, on a given place and time ($H_{x,y,t}$). Repeated measurement can approximate the elevation change over a given point through,

$$\frac{dh}{dt} = \frac{H_{x,y,i} - H_{x,y,j}}{\Delta t_{ij}} \tag{2.10}$$

For elevations products extracted into a grid, the transformation to volumetric change is done through multiplication with the dimension of the grid cell (r^2). This is followed by a summation over all grid cells of the glacier (n_A) [Etzelmüller, 2000];

$$\frac{dV}{dt} = \sum^{n_A} \frac{dh}{dt} \cdot r^2 \tag{2.11}$$

In this manner geodetic measurement can be translated to meaningful glaciological concepts. The relations mentioned above, and specifically the relation in equation 2.9, may be used in different manners. For example, if the the velocity regime doesn't change, then the volume change is equal to the mass balance and can be estimated by photogrammetric products [Krimmel, 1999]. It may also be inverted, if the kinematics of the mass is known, it is possible to estimate the volume change and dynamics. This is case is possible for rock glaciers, as its material is incompressible [Debella-Gilo and Kääb, 2012].

In the following section highlights geodetic methodologies applied in glaciology. They highlight the possibilities optical and laser remote sensing instruments, and their applicability for photoclinometry and registration.

2.3.1 Optical Remote Sensing

The influence of topography on reflectivity within satellite imagery is addressed in many textbooks and this component is corrected to normalize radiometric measurements [Richter, 1998]. In glaciology, these reflection fluctuations were identified with undulations [Dowdeswell and Mc Intyre, 1987], and topographic fluctuations [Rees and Dowdeswell, 1988]. Optical images have mostly been used to enhance a wide spaced elevation model into a high resolution product [Bingham and Rees, 1999], [Bindschadler et al., 2002] and [Scambos and Haran, 2002]. Or local topographic profiles along the direction of the sun [Raup et al., 2005].

Due to the low orbit of optical satellites, a visit to polar regions is brought more often than to low latitudinal regions. Thus if the instrument has a broad field of view, a location with a high latitude can be sampled with different sun angles. If two scenes are taken with a different sun angle, its terrain shape is extractable. Thus the gradient over both axis is estimated. Double integration will give a elevation model. Then a course elevation model can be used for absolute orientation [Scambos and Fahnestock, 1998].

With the theory of photoclinometry it is also possible to detect and interpret topographic surface changes. If two acquisitions are selected with a similar sun angle, and equal illumination and reflection function, the only prominent free parameter is the surface slope. The small undulations on the snow surface can be detected [Bindschadler et al., 2010].

2.3.2 Laser Ranging

Spacing of ICESat GLAS transects widens the further one moves away from the pole. However, already a few transects can give a comprehensive estimate of a glacier mass balance [Sauber et al., 2005], [Kääb, 2008]. Thus ICESat GLAS is not only capable of measuring the great ice masses, but smaller ice fields and glaciers mass balances can also be estimated [Nuth et al., 2010].

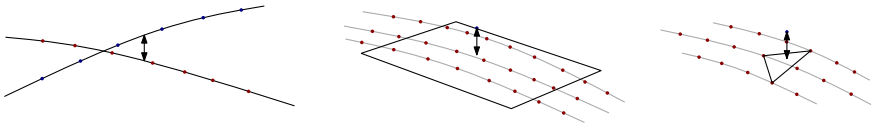

Figure 2.10: Drawings illustrating several methodologies to extract elevation differences between different profiles. From left to right; interpolation to its intersection [Slobbe et al., 2008], zonal plane fitting [Moholdt et al., 2010b] and a local plane fitting methods [Pritchard et al., 2009].

Most glaciological studies use the transects, or the intersections. Several methods are developed to estimate surface elevation differences. As the pointing positioning has an accuracy of within a few meters, and secondly the footprints are not perfectly overlapping. Thus interpolation over transect can be used [Slobbe et al., 2008], triangulation [Pritchard et al., 2009]. Or by the use of plane fitting over multiple transects [Moholdt

et al., 2010b].

2.3.3 Aggregating both acquisition systems

The two satellite systems have been used together before for glaciological purposes. In the parts where reliable image matching is difficult, differencing ICESat GLAS measurements can give an estimate of volume change over the wide upper part. In the lower part of the glacier optical imagery can produce reliable elevation models of the narrow glacier snout. By these means a balanced estimate of the volume change is constructed [Howat et al., 2008]. However both system only complement each other, there is no integration between both measurement methods.

An example of cooperation is found in the use of ICESat GLAS footprint as ground control. Distinct features, e.g.: nunataks and ridges , are selected from the imagery and ICESat GLAS profiles. The extracted elevations from ICESat GLAS are used for ground control, to calculate the registration parameters of the aerial triangulation [Schenk et al., 2005].

A combination of altimetry and optical remote sensing measurements has been used to assess subglacial hydrolic systems in Antarctica [Fricker et al., 2010]. The altimetric measurements could identify elevation differences along a profile. With these candidate areas, image differencing techniques could identify the spatial extent of these lakes. Combined with bedrock and elevation data, water pressure potential could be estimated and an increased understanding of the sub-glacial drainage system was obtained.

Elevation changes derived from repeated ICESat GLAS tracks lack the fine sampling of the photogrammetric method. Additionally, they are less robust on a local scale [Moholdt et al., 2010b]. A combination of both methods may produce a more reliable estimate out of ICESat transects. Extracting a elevation model by a combination of ICESat GLAS and photoclinometry is recently conducted [Bindschadler et al., 2011a]. These products were used to estimate the grounding line along the coast of Antarctica.

Chapter 3

Computational theory

The measurement configuration and its implementation for this work was described in the former chapter and gives an understanding of the acquisition process. This understanding is needed to interpret the different computational techniques that can be applied to the measurements. Thus this chapter will focus on the methods that can be used for the proposed implementation. After this chapter, the implementation of the algorithms and methods can be presented.

3.1 Forward model

The first entity is the forward model, where a model predicts an observation that is based on a theory. It relates physical parameters from the natural world to observable quantities. For this study the physical parameter is elevation, and together with the suns position an observable relief shading is constructed.

3.1.1 Shading function

The input for the forward model is a digital elevation grid ($\mathbf{H}$). This is a sampling pattern of points in a regular rectangular interval (dx, dy). Those samples are elevation values of the earth surface. At every point at this surface, there is a normal vector. This normal vector is the vector perpendicular to the tangent of the surface. The shading function is described on these points. The tangent can be estimated using the neighboring points. The change along both axis of the grid composes a gradient vector;

$$\nabla \mathbf{H} = \left(\frac{\partial \mathbf{H}}{\partial x}, \quad \frac{\partial \mathbf{H}}{\partial y} \right) \tag{3.1}$$

The planar gradients of a spot on the surface is estimated through convolution, *i.e.*[Young et al., 1995]:

$$\mathbf{K}_{\partial x} \otimes \mathbf{H} \approx \nabla_x \quad \mathbf{K}_{\partial y} \otimes \mathbf{H} \approx \nabla_y \tag{3.2}$$

The result from the kernel (**K**) is change in grid units, the gridspacing (l) is used to transform to a metric unit. With these terms known it is possible to compose the normal vectors ($\vec{n}$) on each elevation point. A dot product with the sun vector ($\vec{s}$) gives the amount of sunlight received at a unit area of the tangent plane;

$$\cos(\theta) = \frac{\vec{n} \cdot \vec{s}}{|\vec{n}| \cdot |\vec{s}|}, \qquad \text{where} \quad \vec{n} = \begin{bmatrix} -\nabla_x \\ -\nabla_y \\ 1/l \end{bmatrix} \tag{3.3}$$

Topography along the suns' direction has the most influence on the resulting brightness. Surfaces with another orientation do influence the shading, but to a lesser degree. Therefore the information content extractable from a shading, is dependent on surface orientation.

3.1.2 Photoclinometric lane

The shading function prominently uses information along one direction, it is an area based approach. However the model may be described along the solar direction, in a one dimensional relation. The sensitivity of the sensed samples (DN) to undulations of the terrain perpendicular ($\psi_\perp$) or along ($\psi_\parallel$) the azimuth of the sun is given by [Bindschadler and Vornberger, 1994],

$$\frac{\partial DN / \partial \psi_\parallel}{\partial DN / \partial \psi_\perp} = \frac{\cos^2 \psi_\perp}{\cos^2 \psi_\parallel} \cdot \frac{\tan\psi_\parallel \cdot \tan\varphi - \tan^2 \psi_\perp - 1}{\tan\psi_\perp \cdot (\tan\varphi + \tan\psi_\perp)} \tag{3.4}$$

In this relation the elevation of the sun (φ) is in most cases $30°$, a lower elevation increases the ratio. Furthermore the function is most sensitive in small variations in topography. For slopes more than $10°$ the ratio has dropped significantly. Variations in topography perpendicular to the suns' direction have nearly no impact on the ratio. Thus the shading function can be simplified if certain criteria are met. Terrain variation should be low sloped, the suns' elevation low, and topographic orientation mainly in the direction of the sun. Stating this the samples along a profile are transformed to elevation change (dZ) along the suns direction through,

$$\cos(\theta) = \cos((\frac{\pi}{2} - \tan\frac{dZ}{dL}) + \varphi) \tag{3.5}$$

3.2 Model inversion

A linear relation (**A**) between the observations ($\vec{y}$) and its model parameters ($\vec{x}$) can be written in the following way;

$$\vec{y} = \mathbf{A}\vec{x} \tag{3.6}$$

The use of this system can be in three ways. If the parameters and their relation to the real world are known, one can model a real world situation. By these means it is possible to do predictions and model different scenarios. A second way to use this system, is by regression. If both vectors are known, one can construct a model, fitting a relation between both entities. The third usage of this relation is the estimation of unknown parameters.

3.2.1 Leveling model

An implementation of this model into geodetic practice is the estimation of height through leveling. The situation is illustrated on the right. There are four points (x_i) where the upper left point has a known height. In total there are five height differences ($\underline{y}_i$) that are measured between these points. The model describing the relation is given as,

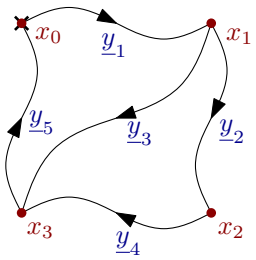

$$\underbrace{E\{\begin{pmatrix} \underline{y}_1 \\ \underline{y}_2 \\ \underline{y}_3 \\ \underline{y}_4 \\ \underline{y}_5 \end{pmatrix}\}}_{\underline{\vec{y}}} = \underbrace{\begin{pmatrix} 1 & 0 & 0 \\ -1 & 1 & 0 \\ -1 & 0 & 1 \\ 0 & -1 & 1 \\ 0 & 0 & -1 \end{pmatrix}}_{\mathbf{A}} \underbrace{\begin{pmatrix} x_1 \\ x_2 \\ x_3 \end{pmatrix}}_{\vec{x}} \tag{3.7}$$

If the unknown heights of $x_1 \dots x_3$ want to be estimated in a least squares sense this is done through[1],

$$\underline{\hat{\vec{x}}} = \left(\mathbf{A}^\top \mathbf{A}\right)^{-1} \mathbf{A}^\top \underline{\vec{y}} \tag{3.8}$$

There are more height measurements than unknown parameters. Due to noise in the observables, consequently its relation will not be exact. However with more measurements the quality of the estimation is improved, both in precision and in reliability. This is done through least squares adjustment and the possibility of hypotheses testing.

3.2.2 Weighted model

The leveling example above assumes that the variances of the measurements are of equal magnitude. Every measurement has the same contribution within the estimation of the unknown parameters. Alternatively, a weighting matrix ($\mathbf{W}$) can be inserted into the least squares estimation. This matrix shifts the importance to certain measurements that compose the model. The parameter vector ($\underline{\vec{x}}$) with the smallest error is chosen, thus the weighting matrix allows to define the smallest fit [Strang and Borre, 1997]. Including the

[1] $\mathbf{A}\vec{x} = \vec{y}, \quad \mathbf{A}^\top \mathbf{A}\vec{x} = \mathbf{A}^\top \vec{y}, \quad \vec{x} = (\mathbf{A}^\top \mathbf{A})^{-1} \mathbf{A}^\top \vec{y}$

weighting matrix into the estimation results in,

$$\hat{x} = \left(\mathbf{A}^\top \mathbf{W} \mathbf{A}\right)^{-1} \mathbf{A}^\top \mathbf{W} \underline{\vec{y}} \tag{3.9}$$

For a Best Linear Unbiased Estimate (BLUE), the weighting matrix is equal to the inverse of the covariance matrix ($\mathbf{Q}_{yy}^{-1}$). On the diagonal of the covariance matrix the variations of the measurements are placed (σ_i^2), while correlations between the measurements are listed off-diagonal (σ_{ij}). If a weight is increased up to infinity, it becomes a constraint on the parameters. However there are other ways to implement constrainted models. For example one can subdivided the procedure into several iterative steps. At first, there is a normal estimation, in the form of equation 3.8 or 3.9. At the second phase a new system of equations is added to the model, *i.e.:*

$$E\{\underline{\vec{y}}\} = \mathbf{A}\vec{x} \qquad \mathbf{C}^\top \vec{x} = \vec{k} \tag{3.10}$$

The matrix $\mathbf{C}$ describes the relation of the parameter with a property ($\vec{c}_0$). This relation is input for the fundamental equation (3.8) again. However the variance matrix is changed into the variance matrix of the estimate ($\mathbf{Q}_{\vec{x}_A \vec{x}_A}$).

$$\hat{x} = \vec{x}_A - \mathbf{Q}_{\vec{x}_A \vec{x}_A} \mathbf{C} \left(\mathbf{C}^\top \mathbf{Q}_{\vec{x}_A \vec{x}_A} \mathbf{C}\right)^{-1} \mathbf{C}^\top \left(\vec{x}_A - \vec{k}\right) \tag{3.11}$$

This procedure is computer friendly, as the matrix size is kept as small as possible. However the constraints can also be included into the model all at once, *i.e.:*

$$\begin{pmatrix} \left(\mathbf{A}^\top \mathbf{Q}_{yy}^{-1} \mathbf{A}\right)^{-1} & \mathbf{C} \\ \mathbf{C}^\top & 0 \end{pmatrix} \begin{pmatrix} \underline{\hat{x}} \\ \underline{\lambda} \end{pmatrix} = \begin{pmatrix} \mathbf{A}^\top \mathbf{Q}_{yy}^{-1} \underline{\vec{y}} \\ \vec{k} \end{pmatrix} \tag{3.12}$$

In this sense there is a constraint on the minimum value to be found. The constraint is incorporated by Lagrange's method. The illustration on the right illustrates the method for a two dimensional case. There is a function $f(x, y)$ and a constrain, given in the form of $g(x, y) = k$. Thus if a maximum value is to be found for the function, it can only be on the line $g(x, y) = k$. This maximum is found when they have a common tangent line, and can be written as; $\nabla f(x, y) = \lambda \nabla g(x, y)$, for a given scalar λ [Teunissen et al., 2005].

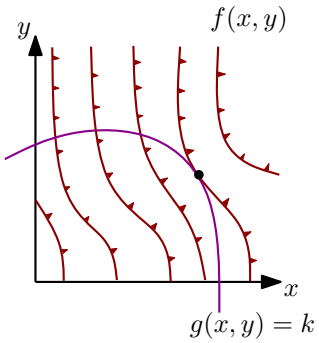

3.2.3 A priori knowledge and relations

Taking the former property into account it is possible to add constrains into the relation, for example a constraint on elevation curvature, as glaciers are gradually fluctuating in

height. Their curvature is very low, thus relations like these can easily be included into the **A**-matrix *e.g.*:

$$\begin{pmatrix} \vdots \\ 0 \\ \vdots \end{pmatrix} = \begin{pmatrix} \vdots & \vdots & \vdots \\ -1 & 2 & -1 \\ \vdots & \vdots & \vdots \end{pmatrix} \begin{pmatrix} h_{i-1} \\ h_i \\ h_{i+1} \end{pmatrix} \tag{3.13}$$

By appending these constrains into the model, the iteration will propagate to a function with a minimal curvature. This relation is a discrete Laplace operator, relating neighboring points to their second order partial derivative. The relation is valid for surfaces that are flat or have a constant slope [Gorte, 2006].

The relation is a condition that is not extractable from the imagery. However this extra property is known *a priori* by the observer. Another property of the elevation model is its potential field, where the curl operator of the elevation estimation would result in zero ($\nabla \times \mathbf{H} = \vec{0}$). This relation can also be implemented in the design matrix, or it can be put forward as a constrain.

Information about the parameters can also be integrated in the relation. If certain coordinates are known, they can be concatenated under the design matrix. The estimate of the parameter used together with its precision to help to stabilize the adjustment. The precision of the parameters can be simplified to a diagonal matrix and a scalar, where this scalar value can be used to steer the iteration. This extension is known as the *Tikhonov* regularization [Vermeer, 2010]. Its general form is written in the relation as follows:

$$\begin{pmatrix} \vec{y} \\ \vec{x} \end{pmatrix} = \begin{pmatrix} \mathbf{A} \\ \mathbf{I} \end{pmatrix} \hat{\vec{x}} + \begin{pmatrix} \vec{e}_y \\ \vec{e}_x \end{pmatrix} \tag{3.14}$$

3.2.4 Non-linear models

The former model used a linear relationship. However, a relation is not always linear. To still use the least squares adjustment, the relation can be approximated through linearization of the function. In that case, the non-linear function is described as a power series. This is made possible through *Taylor*-series expansion.

$$\begin{aligned} T_k(x) &= \sum_{i=0}^{k} \frac{f^{(i)}(x_0)}{i!} \cdot x^i \\ &= f(x^0) + \frac{f'(x_0)}{1!} \cdot (x - x_0) + \frac{f''(x_0)}{2!} \cdot (x - x_0)^2 + \dots \end{aligned}$$

If the degree (k) of a *Taylor*-polynomial increases, it will increasingly conduct the behavior of $f(x)$. When a *Taylor*-polynomial has a certain degree, its sequent terms are

concatenated into a remainder (R_k). This gives the following relation,

$$f(x) = T_k(x) + R_k(x) \qquad \lim_{k\to\infty} R_k(x) = 0 \quad \text{than} \qquad f(x) = T_k(x) \tag{3.15}$$

If the approximation (x_0) is relatively close to x, then the *Taylor*-series can be truncated after the second-order term [Teunissen, 2003], as the remainder is negligible small. When a function is multivariate, it is not only the variation over one variable that is of importance, also its relation to other variables that should be taken into account. The structure of all the variables' first order variations and their influences on each other is stated within the Jacobian;

$$\mathbf{J}_F(\vec{x}) = \begin{pmatrix} \frac{\partial y_1}{\partial x_1} & \cdots & \frac{\partial y_1}{\partial x_n} \\ \vdots & \ddots & \vdots \\ \frac{\partial y_m}{\partial x_1} & \cdots & \frac{\partial y_m}{\partial x_n} \end{pmatrix} \tag{3.16}$$

Equation 3.15 gives a one dimensional case. If this relation is transformed into a multivariate relation, with the help of equation 3.16, one gets a linearized estimation in the form of,

$$\vec{y} = \mathbf{A}\vec{x}_0 + \mathbf{J}(\vec{x}_0)(\vec{x} - \vec{x}_0) + R_1(\vec{x}) \tag{3.17}$$

3.3 Iteration strategies

A linear least squares problem can be computed directly. In a non-linear case, an initial guess should be given first, after which it is approximated by a linear system. The result is a new estimate, being a new guess; an iteration is at hand. The principle of an iteration is to migrate to a (local) minimum (x^*) or (local) maximum. And terminated when a certain threshold is passed, *i.e.:* the difference between estimated and measured are negligibly small ($e = y - \mathbf{A}x$ or e^2).

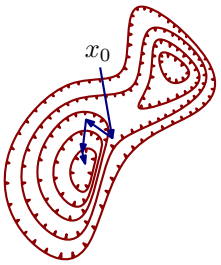

In the former paragraph *Taylor*-expansion was constructed from an approximation and its derivatives, see equation 3.15. However the series expansion can also be used to describe the behavior of the function within a neighborhood, *i.e.:*

$$f(x + \Delta x) = f(x) + \frac{f'(x)}{1!} \cdot (\Delta x) + \frac{f''(x)}{2!} \cdot (\Delta x)^2 + \ldots \tag{3.18}$$

For the multiple valued case, up to the first order, this gives the gradient-descent method [Madsen and Tingleff, 2004];

$$f(\vec{x} + \vec{\delta}) \approx f(\vec{x}) + \mathbf{J}(\vec{x})\vec{\delta} \tag{3.19}$$

At first *Newton-Raphson*'s method is given in a one dimensional case, this can give a handhold for the methods later on. The method starts with an approximation, and calculates its first derivative, the tangent of this function. The crossing of this tangent line with the *x*-axis is used as the next approximation. This procedure starts all over again until a crossing of the function with the *x*-axis is found. At first the triangle of the approximation *k* is given and after rearranging the terms gives the new approximation;

$$f'(x_k) = \frac{f(x_k)}{x_k - x_{k+1}} \quad \rightarrow \quad x_{k+1} = x_k - \frac{f(x_k)}{f'(x_k)} \tag{3.20}$$

This same method can be used with the derivative of the function. Through this means a local minimum or maximum can be found. Extending this method to the second derivative and in a multivariate case, it becomes a *Gauss-Newton* iteration:

$$\vec{x}_{k+1} = \vec{x}_k + \left(\mathbf{J}^\top \mathbf{J}\right) \mathbf{J}^\top \left(\vec{y} - \mathbf{A}\vec{x}_k\right) \tag{3.21}$$

Here the multiplication of the two first order derivative of the function ($\mathbf{J}(\vec{x})$) is an estimation of the Hessian ($\mathbf{H}(\vec{x})$), the second order derivative of the function. This multiplication is a faster implementation and gives a reliable estimation.

For very nonlinear functions it is necessary to have a good approximation, otherwise the iteration can converge into a local minimum. The *Newton-Raphson* is a good method for the last stage of an iteration [Madsen and Tingleff, 2004]. It can also end up in a loop, thus a threshold on the number of iteration steps can be necessary.

If the initial guess is far from the minimum, a faster approach is preferable. This can be done through adjustment on the diagonal elements of the normal matrix. The scalar convergence factor [Milman, 1999] is dynamical. Thus when the estimation comes closer to a local minimum, the convergence factor minimizes. Changing the gradient descent method back to a *Gauss-Newton* iteration, *i.e.:*

$$\vec{x}_{k+1} = \vec{x}_k + \left(\mathbf{J}^\top \mathbf{J} + \mu \mathbf{I}\right) \mathbf{J}^\top \left(\vec{y} - \mathbf{A}\vec{x}_k\right) \tag{3.22}$$

where,

$$\mu = \tau \cdot max\{diag\{\mathbf{J}^\top \mathbf{J}\}\} \tag{3.23}$$

Here τ is a coefficient describing a measure of closeness of the estimation. Where a small value indicates an estimate close to the true value.

3.3.1 Batch estimation

Everything is related to everything else, but near things are more related than distant things. That is the first law of geography according to Mr. Tobler [Harvey, 1969]. This law should be recognizable in the design, as there is an aim to model a geographic entity. So if the influence of far away phenomena is of less importance, this should be represented

in the design matrix. Therefore the design matrix will have a fairly sparse appearance.

This sparsity of the design matrix can be an advantage for the computation of the estimation. Smaller blocks of normal matrices can be made, constructed from parts along the diagonal. These blocks can be solved faster, as big matrix inversions are avoided. However the estimates should eventually be stitched together and result in a coherent estimation. Regulating the overall estimate is done through the inclusion of global parameters in the adjustment, these are composed into the matrix $\mathbf{G}$. This batch processing is known as *Helmert-Wolf* blocking, and it splits the normal equation as [Teunissen, 1985], [Lavallée, 2005]:

$$\begin{pmatrix} \mathbf{A}_{11}^\top \mathbf{A}_{11} & 0 & \cdots & 0 & \mathbf{A}_{11}^\top \mathbf{G}_{11} \\ 0 & \mathbf{A}_{12}^\top \mathbf{A}_{12} & \cdots & 0 & \mathbf{A}_{12}^\top \mathbf{G}_{12} \\ \vdots & \vdots & \ddots & 0 & \vdots \\ 0 & 0 & 0 & \mathbf{A}_{ij}^\top \mathbf{A}_{ij} & \mathbf{A}_{ij}^\top \mathbf{G}_{ij} \\ \mathbf{G}_{11}^\top \mathbf{A}_{11} & \mathbf{G}_{12}^\top \mathbf{A}_{12} & \cdots & \mathbf{G}_{ij}^\top \mathbf{A}_{ij} & \sum_{ij} \mathbf{G}_{ij}^\top \mathbf{G}_{ij} \end{pmatrix} \begin{pmatrix} \hat{\underline{x}}_{11} \\ \hat{\underline{x}}_{12} \\ \vdots \\ \hat{\underline{x}}_{ij} \\ \hat{\underline{g}} \end{pmatrix} = \begin{pmatrix} \mathbf{A}_{11}^\top \underline{\vec{y}}_{11} \\ \mathbf{A}_{12}^\top \underline{\vec{y}}_{12} \\ \vdots \\ \mathbf{A}_{11}^\top \underline{\vec{y}}_{11} \\ \sum_{ij} \mathbf{G}_{ij}^\top \underline{\vec{g}}_{ij} \end{pmatrix} \tag{3.24}$$

This blocking is mostly used to solve border crossing triangulations. Where enormous national triangular networks should be adjusted. Fortunately the blocks can be solved independent from each other. The estimated global parameter is used within the global adjustment. Followed by an update within the regional adjustment.

3.4 Classification

For now the mathematical strategy and some of its aids are highlighted. Hence it is time to discuss the manners of implementing these strategies onto real world observable data. Before these methods can be applied to them, there is some preprocessing needed, for example the identification of snow covered or shadow casted terrain. This identification is done by classification of reflections or properties related to their neighborhood.

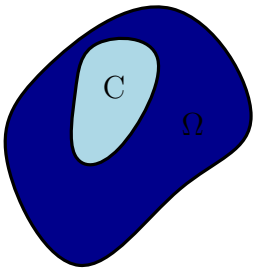

With an optical acquisition we sense reflections, again this is the *effect* of interaction of the sun with a certain *cause*. One can assume that objects within the same class will have a similar reflection pattern. Thus reflection values can help in the discrimination of these classes. Again a corrupted sample space is sampled instead of the intended reflection domain. These corruptions are present within the data, due to for example the atmosphere, and sensor noise. Secondly the sensing system may have mixed pixels, it records a weighted sum of reflections from other classes within the sensed (sub)surface.

3.5 Photoclinometry

Section 3.1.1 described the theory of the shading function. This section will implement its inverse theory, by describing the different components that make up the model.

The relation between intensity differences and topographic change is intuitive. When these values are to be used in a quantitative manner a model needs to be constructed. It relates the reflection function to the interaction of sun vector ($\vec{s}$), normal vector ($\vec{n}$) and observation vector ($\vec{e}$). Thus two spatial relations need to be established; a sensor and a reflection model. The sensor model is used to estimate the exitance vector, while the reflection model quantifies the amount of reflection to that direction.

3.5.1 Sensor model

To estimate the observation vector, the position of the instrument with respect to the topography needs to be known, *i.e.*:, attitude and position information of the flight path over time. This is measured during the overpass of the platform, by the aid of GNSS navigation and star-trackers, among others. The measurements give the position vector within an terrestrial reference frame, *e.g.:* WGS84. However for simplification of the relation, a camera centered coordinate system is used. Here the planar axes are aligned with the sensor frame, *i.e.*: rows and columns of the imagery. Perpendicular to this frame, is the vertical axis. An example of a camera coordinate system for a pushbroom sensor is illustrated in figure 3.1.

For a pushbroom sensor this reference frame changes every sampling interval, this does simplify the calculation of the observation vector. Due to the perspective projection, the changes of the observation vector only occurs perpendicular to the flightpath, where the extent is dependent on the focal length (f). The transformation of row elements into the displacement from the focal point (x), is calculated through parameters (dx) that are given by the interior orientation estimation of the sensor.

$$x = (\text{row} \cdot \text{pixelspacing}) - dx, \qquad \vec{e} = \begin{bmatrix} e_x \\ e_y \\ e_z \end{bmatrix} \approx \begin{bmatrix} \frac{x}{f+x} \\ 0 \\ \frac{f}{f+x} \end{bmatrix} \tag{3.25}$$

The sun vector can be approximated for every point on earth. Therefore one needs the latitude, longitude, approximate height and time. These can be extracted from the ephemeris of the satellite acquisition. This sun vector is defined in a global reference frame, and a transformation to the local system is needed. This transformation is calculated through the rotational angles. The sun angle changes, in position and time, but if a small terrain is sampled, one can simplify and use a far field approximation. The transformation into a camera based reference frame can be described as three successive elementary rotations along the three primary axis (θ, ϕ, κ), *e.g.*: *Cardano* rotations [Klees, 2009];

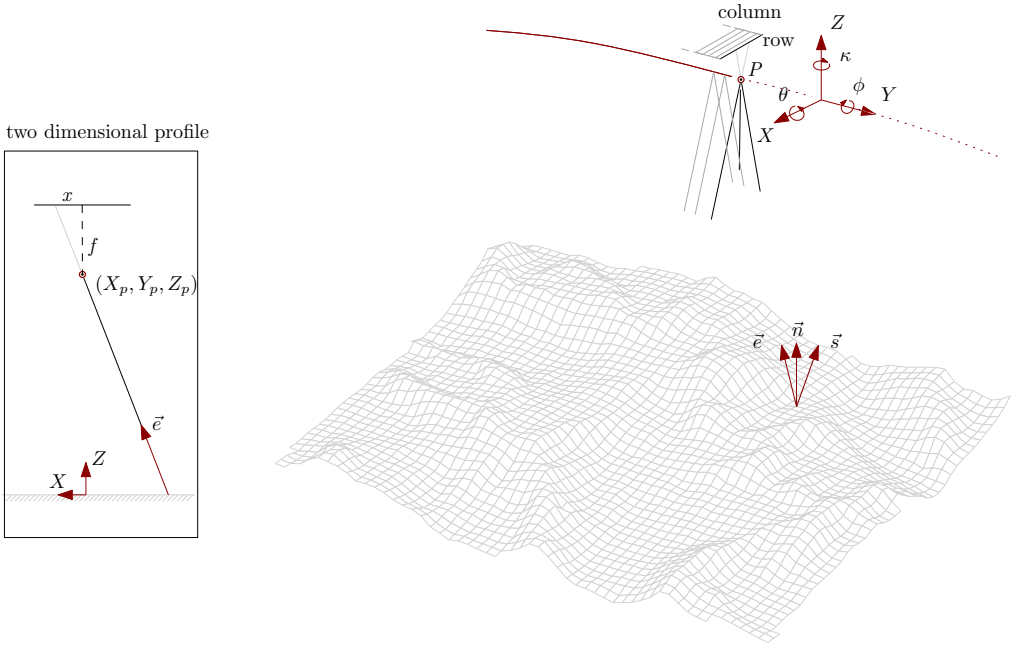

Figure 3.1: *left*) planar view of a line sample of a pushbroom sensor. *right*) Schematic view of surface orientation in respect to a pushbroom sensor at time and position P.

$$\vec{s} = \begin{bmatrix} s_x \\ s_y \\ s_z \end{bmatrix} = \mathbf{R} \cdot \begin{bmatrix} s_X \\ s_Y \\ s_Z \end{bmatrix}, \quad \text{where} \tag{3.26}$$

$$\mathbf{R} = \begin{bmatrix} \cos\phi \cdot \cos\kappa & \cos\theta \cdot \sin\kappa + \sin\theta \cdot \sin\phi \cdot \cos\kappa & \sin\theta \cdot \sin\kappa - \cos\theta \cdot \sin\phi \cdot \cos\kappa \\ -\cos\phi \cdot \sin\kappa & \cos\theta \cdot \cos\kappa - \sin\theta \cdot \sin\phi \cdot \sin\kappa & \sin\theta \cdot \cos\kappa + \cos\theta \cdot \sin\phi \cdot \sin\kappa \\ \sin\phi & -\sin\theta \cdot \cos\phi & \cos\theta \cdot \cos\phi \end{bmatrix}$$

In this sense the sensor vector and sun vector can be aligned, if the satellite attitude and position is known.

3.5.2 Reflection model

Due to the sensor model it is now possible to have for every point on the image acquisition a known observation and sun vector. Of coarse this is up to a certain degree of precision. With these known parameters a reflection function of the phenomena need to be included to extract the unknown topography. This section will highlight only some simple photometric models, a more broader view on this topic is given by [Rees, 2001].

Section 2.2.1 described general reflection properties of snow. Apart from the geographic orientation, other components like grain size did influence the reflection properties. The behavior of the snowpack can be approximated by a mathematical function. A

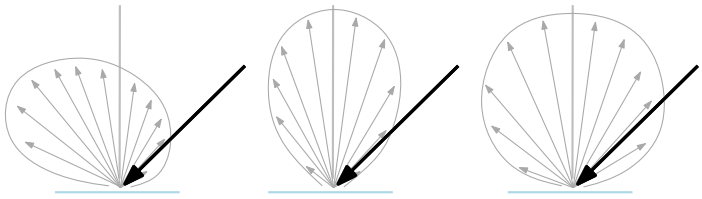

(a) Henyey-Greenstein (b) Minnaert (c) Lambertian

Figure 3.2: Planar view of different simple bidirectional reflectance distribution function (BRDF) models. The black arrow indicates the energy incident to the surface, while the gray arrows represent the reflection function.

simple surface radiation model is the *Lambertian* reflection function. In these models the local incidence (θ_0) and exitance (θ_1) angles are used with respect to the surface normal. The *Lambertian* reflection function reads;

$$R \propto \cos\theta_0 \tag{3.27}$$

A more complex model is found in the *Minnaert* reflection function. This function is often used to describe lunar surfaces. The limb-darkening parameter (κ) can be adjusted to fit the right specific lunar surface [McEwen, 1991]. It can adjust the amount of reflection to or from the local surface normal.

$$R \propto (\cos\theta_0 \cdot \cos\theta_1)^{\kappa-1} \tag{3.28}$$

The functions above have a diffuse scattering, while this may not always be the case. Dependence on the relative angle in the plane, using the azimuthal angles (ϕ_0, ϕ_1), can also be included. In the *Henyey-Greenstein* reflection model an asymmetry parameter (Θ) can be included. This parameter can be used to describe a more backward or forward scattering, *i.e.*:

$$R \propto \frac{1-\Theta^2}{(1+2\cdot\Theta\cdot\cos\theta_0\cdot\cos\theta_1+\sin\theta_0\cdot\sin\theta_1\cdot\cos(\phi_1-\phi_0)+\Theta^2)^{\frac{3}{2}}} \tag{3.29}$$

If the sensor model is combined with a reflection model a formulation of the problem is described in a mathematical manner. The observation and sun vector are known, and the reflection values are measured, thus now one has a mathematical framework to estimate the topographic signal within the imagery.

3.6 Absolute elevation

Any estimation of shape through photoclinometry will have an arbitrary height. Measurement from laser altimetry may be used to estimate the transformation parameters, to get the shape from a local frame to a georeferenced frame. This procedure is known

as registration, or absolute orientation [Polman and Salzmann, 1996]. It uses similar features in both frames to estimate the unknown rotations, translations and scale factors.

Rotational transformation A transformation of coordinates changes the coordinates of points from one datum to the other. Each datum has a origin where each axis can be defined by a unit vector ($\vec{e}$). Here only three dimensional *Euclidean* spaces are considered. A coordinate frame is defined by three unit-vectors that span an orthogonal triad ($[e_x \quad e_y \quad e_z]$). If two coordinate system have the same origin, the transformation from one system to the other is done through multiplication with a Rotational matrix ($\mathbf{R}$). Entities within the rotational matrix are composed by the multiplication of individual unit vectors, for example, the rotation from datum *a* to *i* is given by:

$$u^i = (e_i \cdot e_a)v^a = R_i^a v^a \quad \rightarrow \quad \vec{u} = \begin{pmatrix} R_1^1 & R_1^2 & R_1^3 \\ R_2^1 & R_2^2 & R_2^3 \\ R_3^1 & R_3^2 & R_3^3 \end{pmatrix} \vec{v} \tag{3.30}$$

A rotation along one axis can also be described as a function. In this way an axis is fixed and the rotation is described by an angle (γ). An rotation along the vertical axis is than composed through;

$$\mathbf{R}_\gamma = \begin{pmatrix} \cos\gamma & -\sin\gamma & 0 \\ \sin\gamma & \cos\gamma & 0 \\ 0 & 0 & 1 \end{pmatrix} \tag{3.31}$$

Rotations along an arbitrary vector is also possible. For this study this may be of interest, as there may be a systematic bias in the photoclinometric estimate perpendicular to the suns' direction ($\vec{s}_\perp$). A rotation (κ) along a vector, the rotational matrix is composed in the following way [Klees, 2009];

$$\mathbf{R}_\kappa = \mathbf{E} + (\mathbf{I} - \mathbf{E}) \cdot \cos\kappa - \mathbf{D} \cdot \sin\kappa \qquad \text{where,} \tag{3.32}$$

$$\mathbf{E} = \begin{pmatrix} s_x^2 & s_x s_y & s_x s_z \\ s_y s_x & s_y^2 & s_y s_z \\ s_z s_x & s_z s_y & s_z^2 \end{pmatrix} \quad \mathbf{D} = \begin{pmatrix} 0 & -s_z & s_y \\ s_z & 0 & -s_x \\ -s_y & s_x & 0 \end{pmatrix} \tag{3.33}$$

Translational transformation If two frames have no common origin, a translation is needed. This displacement are the terms within the vector that goes from the first to the second origin. In that sense a rigid coordinate transformation has the form of,

$$\vec{u} = \mathbf{R}\vec{v} + \vec{T} \tag{3.34}$$

Scale transformation There might be a difference in the length of the unit vector in respect to the other frame. For that case a scaling transformation is needed, and only the diagonal of the transformation matrix has entries;

$$\vec{u} = \mathbf{\Lambda}\vec{v}, \quad \text{where} \quad \mathbf{\Lambda} = \begin{pmatrix} \lambda_x & 0 & 0 \\ 0 & \lambda_y & 0 \\ 0 & 0 & \lambda_z \end{pmatrix} \tag{3.35}$$

The extracted photoclinometric elevation model is a product of satellite acquisition. This image is a central projection of the surface onto its sensor. If for simplicity an orthogonal projection is used for the surface, the transformation are in respect to a planar surface. In that case only elevation measure change, while the planar coordinates stay fixed. Consequently, rotations will transform into linear trends superimposed onto the *xy*-plane. Now transformation parameters can be written in a polynomial manner. In that case the estimation can be done through linear least squares estimation.

Chapter 4

Methodology

This chapter is composed out of three sections, they all embody the elaboration of an idea. Each section starts with the main idea rooted from the research question. Assumptions on this idea are given, followed by the implementation of the idea. At the end of each section the data used for the methodology is given.

4.1 Theme I - Photoclinometry

4.1.1 Idea

With a hillshading function it is possible to construct a shading from a elevation model. If inverse theory is used it may be possible to estimate a elevation model from a shading.

4.1.2 Assumptions

The idea above implies a relation that shall be integrated into a model. This model will describe the connection between intensity and surface orientation. For the implementation of this model, certain assumptions need to be made to formalize the relation. The following assumptions and limitations are taken,

- ⋆ *Reflections properties over the snow surface are uniform*
  Apart from surface orientation, the albedo of snow is mostly influenced by grain size and windblown features. The model does not incorporated effects caused by these components. And it is assumed that the snow is fresh and sastrugi is absent.

- ⋆ *The photoclinometric relation is a Lambertian function*
  Variation of incoming solar radiation over mountainous terrain can be described by a *Lambertian* function [Dozier and Outcalt, 1979]. Then this energy is reflected by snow in an isotropic manner. Finally the instrument senses the terrain from a

nadir view. Combining all these effects, the relation may best be described by a *Lambertian*-function.

- ⋆ *The scene is illuminated with a point light source*
  The sun is the major illumination source for a normal optical acquisition. However multiple reflection or blackbody radiation is also sensed by the instrument. For this implementation these effects are assumed to be neglectable, or well below the noise level.

- ⋆ *Atmospheric effects are neglectably small or constant over the scene*
  Different frequencies of electromagnetic energy is absorbed or scattered within different atmospheric layers. These effects are considered to be constant over the optical acquisitions, and within the noise level.

- ⋆ *Only snow covered terrain is considered*
  Compared to other terrain types, snow has a fairly simple reflection pattern. Therefore the model only uses terrain covered with snow that is directly enlighten. Furthermore, shadowing is not considered in the surface modelling.

4.1.3 Implementation

The following text describes the function relating topography to shading, *i.e.:* forward model. Then the methodology of the inverse function is highlighted. This is followed by a section on regularization processes. And finishes with classification procedures to include only snow covered terrain.

Forward model Starting point of the forward model is a square spaced elevation grid. The kernel estimating the planar gradient over this grid, see equation 3.2, only uses the direct neighbor at the bottom and leftside. If a gradient at the border should be calculated, it uses the neighbor at the top or rightside instead. Together with the gridspacing of the elevation model, the planar gradients compose the normal at every point within the elevation grid. The dot-product of these components with the sun vector make up the shading function, as in equation 3.3. In this manner the number of elevations is related to an equal number of shading values. The function is provided in the Appendix in algorithm 1.

The estimation of curvature is done through the use of direct neighbors. For this study the curvature perpendicular to the suns' orientation is used as regularization, as described in section 3.2.3. But, at the border the curvature can not be calculated, and is therefor not estimated. Algorithm 2 in the Appendix describes its implementation for a regular grid.

Inverse method Two approaches are possible in the model inversion, as illustrated in figure 4.1. An inverse approach can try to estimate the gradient field (h^{-1}), and in a second step transfer to a elevation model (g^{-1}). Transformation from a gradient field to a elevation model is done through integration [Frankot and Chellappa, 1988]. Another

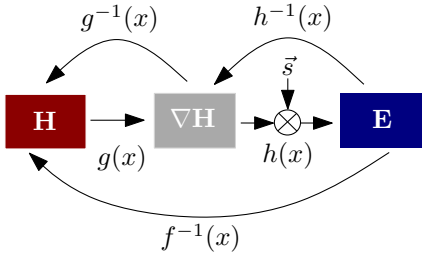

Figure 4.1: Strategy of extracting the shading (**E**) from a gradient field (∇**H**), that is defined through a elevation model (**H**), and their inverse relations.

approach formulates a direct relation between a shading and a elevation model (f^{-1}).

The shading function is a non-linear function, direct estimation through linear least squares adjustment is not possible. The function is linearized and *Levenbergh-Marquardt* iteration is used to estimate the elevation model. The algorithm is written down at the Appendix in algorithm 3. Its Jacobin (∂**A**) is found in a numerical manner, it changes one elevation post and looks at the resulting difference. By incorporating all these relations of elevation values with each other, it will compose a coherent elevation model in one step.

A closer look into theory reveals two components of importance. As described in the former chapter, the estimation through photoclinometry is worked out along lanes. Thus the photoclinometric relation estimates these lanes, see section 3.1.2, and these result in elevation values within the grid. If the sun vector is not aligned with one of planar axis, the profiles are connected with each other, as their relation is based on their neighbors. Thus along the sun's direction the elevation is estimated by the physical properties of photoclinometry. While perpendicular to this direction, the profiles are attached through their mathematical estimation of the gradient. The unknowns that are estimated are; 1) the photoclinometric scale factor (λ), and 2) the relative integration constant for each profile (C).

Regularization The iteration process aligns the photoclinometric lanes next to each other. In order to ensure the iteration converges into a model that conforms reality, regulation may be used. Two regulations can be used; 1) a local regularization on curvature, and 2) global regularization build from a patchwork.

In most photoclinometric algorithms a constraint is formulated on the overall curvature in the planar direction of the estimated function. This is to resolve the ambiguity in azimuth, however it is not the overall curvature that should be minimized, it is the curvature perpendicular to the sun, that should be minimized. In this manner the iteration tries to align the photoclinometric lanes with a difference as small as possible.

The shading function is calculated through local information, but all the equations are solved in one step. Especially the computation of the Jacobian matrix become in-

tense, as its size increases quadratically. To prevent large computing time, it is more convenient to process small blocks. But every block may have its own systematic bias and tilt, which can make aggregation of the estimates more difficult. Thus a procedure is needed to aggregate or stitch these estimates together. Two approach are possible with the global regularization; 1) top-down ,and 2) bottom-up.

A quad-tree can be used in a top-down approach. Different levels of an image pyramid are constructed. It starts with an estimate of a elevation model on the highest level. This approximation can be used as an initial estimate in a lower level. It eventually stops when the lowest level has calculated an estimate.

A bottom-up strategy is a *Helmert-Wolff* blocking, see formula 3.24. The imagery is split into blocks with overlap. Elevation grids are estimated for these blocks, and elevation values of there overlap are selected. These are used in a global adjustment, as these overlaps need to have the same elevation values. After the adjustment, the calculated property is brought back to the individual blocks and used as regulation. This recursion is stopped when the global estimate reaches a certain threshold, mostly based on iteration steps or changes in parameter size.

Classification To select the snow covered area from a satellite acquisition, different methods can be used. If an acquisition has multiple bands, a classification over the spectral response can be used. The reflectivity of snow within the spectrum is illustrated in figure 4.2. The reflection is high in the range around 0.55 μm and there is a low reflection in the range of 1.65 μm. A ratio function on these bands can result in an index, *i.e.:* [Dozier, 1989]:

$$\text{NDSI} = \frac{\lambda_{0.55} - \lambda_{1.65}}{\lambda_{0.55} + \lambda_{1.65}} \tag{4.1}$$

This Normalized Difference Snow Index (NDSI) produces a continuous range, but a binary index is needed to have a distinct selection. Therefore a threshold should be chosen, but is an educated guess. Due to the mostly unknown ground situation, *e.g.:* grainsize, small scale topography. Misinterpretation of the threshold can result in holes or islands within the selection. However snow cover on glaciers are mostly big patches of snow. Thus these margins within the selection can be included or excluded by mathematical morphology of opening and closing.

The NDSI includes shadowed areas, however these measurements should be excluded as well. Thus an other cell-based operation can be used to exclude shadow covered terrain. Snow has a high reflectance in the visible spectrum, except from shadowed covered terrain. This property goes on up to the short wave infrared. Thus the product of the digital number for all bands will be low if there is a shadow casted terrain. While areas directly enlightened by the sun will have high values. Thus to indicate the cell is shadow cased, the total value is subtracted from this product, *i.e.:* [Ranson and Daughtry, 1987]:

$$\text{SI} = 1 - \prod_{i=1}^{k} \text{DN}_i/255 \tag{4.2}$$

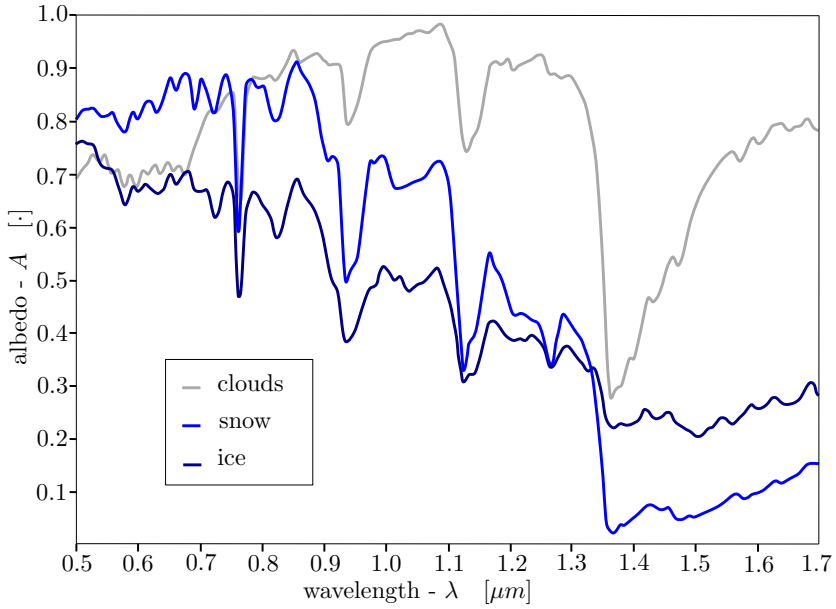

Figure 4.2: Directional hemispherical reflectance of clouds, snow and ice over different wavelengths, adopted from [Dozier, 1989].

If clouds lay over snow covered areas, the distinction is found by selecting an upper and lower bound of the NDSI. Or a ratio image of bands with a wavelength of 0.55 μm and 1.25 μm may be sufficient, as can be seen in figure 4.2. Through this burdening the bulk of clouds can be detected, however cirrus clouds can be difficult to detect through this manner [Choi and Bindschadler, 2004]. Thus other relations need to be applied to identify cirrus or bordering clouds from fresh snow. The cirrus clouds may lay over the snow, and they are detectable as there is a small change in reflection. This is due to shadow, or the difference in reflection of the older snow with respect to the fresh snow in the cirrus cloud. Therefore the range within a small neighborhood might identify the borders of cirrus clouds. Again this is highly dependent on the situation, and thresholding is done through visual interpretation.

These classifications can be bundled to create a subset that only includes measurements of snow covered and shadow free terrain. A pixel based topological union operator can be used for this selection.

4.1.4 Data

All optical acquisitions are interpolated to an UTM projection, using the WGS84 ellipsoid. For Landsat ETM+ data the level 1G product is used. Geometric accuracy should be within 250 meters. The pixel size is 30 meters, intensity values are provided in 8-bit length. For EO1 ALI data the level 1Gst product is used. Acquisitions are corrected for parallax error due to topography. Radiometrically the instrument sampler with 16-bit

length, and has a pixel size of 30 meters. These instruments are multiband imagers, for the photoclinomertic processing band 4 was used (0.775-0.900 μm and 0.775-0.805 μm). It has best contrast of all bands and is mostly used in photoclinometry for glacier surfaces, [Bindschadler and Vornberger, 1994], [Bingham and Rees, 1999].

4.2 Theme II - Registration

4.2.1 Idea

A surface calculated through photoclinometry can be registrated with laser measurements. It may eliminated unknowns as, integration constant, planar trends, and scale factor.

4.2.2 Assumptions

- ⋆ *The horizontal alignment of both products is error less.*
  The coordinates of an optical imagery are described onto a certain projection, within a terrestrial reference frame. The same goes for the laser ranging measurements. Planar registration errors occur along the processing of this data, but for this case these are assumed to be absent.

- ⋆ *The local change of the surface is neglectably small over time.*
  The derived photoclinometric surface model is rooted from the local surface topography at the moment of acquisition. It is assumed this is a representative estimation for the timespan of several years.

4.2.3 Implementation

The surface model needs to be oriented from a local system to a known coordinate system. If a linear relationship is used, an estimation is directly obtained. Fortunately this is easily implemented, as in some cases the unknown parameters can be written down in a polynomial manner. Topographic parameters can be included, like a tilt over two axis [Moholdt et al., 2010b]. Also parameters in the time domain can be added [Slobbe et al., 2008]. In such a case, this model should represent the surface conditions (β), as stated in formula 2.6, through time.

The topographic parameters describe different corrections; at first the uplift (Z) over the vertical axis is unknown. Then there could be a rotational bias (α), due to the sensitivity perpendicular to the sun direction. For temporal variations parameters (*e.g.:* a) could also be inserted into the relation. An option for such a model can have the following polynomial fashion;

$$\vec{y}_{N,E,t} = \alpha_u \cdot N + \alpha_v \cdot E + a \cdot t + \lambda \cdot f(x, y) + Z \tag{4.3}$$

Here the measurement vector ($\vec{y}$) is the elevation of a known location. It is related to the estimated photoclinometric elevation model ($f(x, y)$) by a rotation in northing (N) and easting (E). A linear relation over time (t), a scale factor (λ) and an additional height (Z).

The linear relation over time may be an over simplification within the time span of the ICESat campaign. A more detailed description for the surface conditions may be found in a sinusoidal function [Slobbe et al., 2008]. Though this may not be the most suitable model for glacial surface changes. For example, on Svalbard glaciers the surface pattern is slowly gaining elevation, up to the end of the winter season. Then there is a rapid decline, due to melt in spring and summer. To include a relation like that in a polynomial manner, a function based on a multiplication of sine functions can be used. If multiple sinusoidal functions are added together, an asymmetric triangle wave can be constructed [Weisstein, 2012]. Due to its linear relation within the model, this triangular pattern has a fixed phase. Therefore such a model assumes no variation in the unset of the summer and winter season, or variation in its amplitude, *e.g.:* strong summers or winters.

Concerning topographic parameters; the tilt of the surface model is different along two directions. At first there is the rotational bias perpendicular to the sun direction. This is arbitrary, as multiple answers can be right, due to the mathematical connectivity. A second rotation is related to the miss-alignment of the relation between intensity and inclination. If the axis are aligned along the suns's principle plane, the estimated parameters are these rotations. This principle is the major idea beyond the registration of surface model into elevation estimates.

The tracks of ICESat GLAS profiles can be separated several kilometers of each other. A surface model that would be of this size may have accumulated too much error to be a reliable representation of the surface. Smaller patches can only cover a small part of the glacier. The pattern of laser profiler measurements will be a stripe for these small surface models. This linear sampling pattern is unreliable for estimation of the rotation perpendicular to this track. If one rotational axis is already known, this will help in the stability of the orientation estimation.

The method starts with describing the rotational axis within the model in alignment with the suns direction. A surface model is estimated on the location of a crossing point of two tracks. In that situation the distribution of known elevations is reliable for an estimation of the two rotational angles. This known elevation model can now function as a calibration set. In this process the shading function is related to the elevation model, and the coefficients describing the transition of shading to digital numbers are estimated. The shading of the estimated models should relate one to one with the satellite acquisition. The estimation of these coefficients is done on multiple crossings, to have a redundancy in the estimation. With these coefficients it is now possible to estimated other parts over the track, as now the rotational angle perpendicular to the sun is the only unknown angle. This methodology is illustrated in figure 4.3.

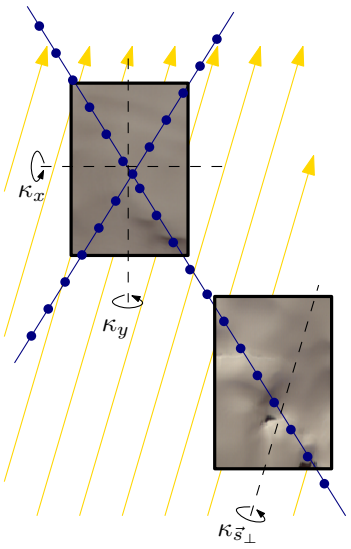

Figure 4.3: Visual illustration of the orientation procedure of photoclinometric elevation models, aided by ICESat GLAS tracks.

4.2.4 Data

ICESat GLAS data of release 33 is used in this study, its GLA06 product gives elevation data in respect to the WGS84 ellipsoid. Binary files were converted to tables by NSIDC GLAS Altimetry elevation extractor Tool (NGAT) version 0.13. This resulted in measurements and a correction table that indicates the height of the geoid in respect to the ellipsoid for every point. This correction term is used to transform to orthometric heights [Strang van Hees, 2006].

4.3 Theme III - Topographic correction

4.3.1 Idea

A topographic correction can be calculated along photoclinometric lanes to align laser data onto a reference track. In that manner, photoclinometry can complement laser profile data.

4.3.2 Assumptions

This methodology makes use of the relation given in section 3.1.2, where the change of the terrain within the solar plane is directly related to brightness values. To justify this relation, some assumptions need to be be taken.

- ⋆ *Small slope criteria*
  The topography is close to flat, but has small undulations, which cause the intensity variation within an optical acquisition.

- ⋆ *Topographyic features are mostly aligned with the sun*
  The sensitivity of a shading function is prominant along the direction of the sun, as is formulated in equation 3.4. Therfore, the topography should be directed into the sun's direction.

- ⋆ *Fresh snow*
  Fresh snow has an homogeneous reflection function, in that sense the *Lambertian* reflection function is a good approximation of the reflection pattern seen in optical imagery.

- ⋆ *Stable topography*
  Dynamics of the topography should be not be locally, like for example, drainage of a sub glacial lake. Changes in elevation may occur, but its magnitude should be on a wide scale, like a glacier surge.

4.3.3 Implementation

Initialization is needed before the estimation of the photoclinometric profiles to the reference track can be applied. The unknown parameters can be estimated or assumed [Bindschadler and Vornberger, 1994]. Most studies use known topography [Pope, 2009], or assume a flat area to train the parameters [Bindschadler et al., 2002]. This study uses the laser profile measurements on a cross-over to extract these parameters.

The estimation set-up is illustrated in figure 4.4. It is composed of two components, the elevation measurements from ICESat GLAS, and the elevation profile from photoclinometry. Starting with the position of a laser point, a bearing along the direction of the sun is taken. Points along on this bearing are estimated through kriging interpolation [Wackernagel, 2003]. This transect will eventually cross the other transect of the laser profiler. At this point the elevation is linearly interpolated, from the two neighboring laser measurements. The second component is the photoclinometric relation over this path.

These two estimates should have the same elevation difference, both measurements should differ each other out. The relation can be stated in an equation, and the unknown parameters can be estimated. However there are two unknowns to be solved, thus at least one more equation is needed into the model. With these profiles in the equation an estimation can be made of these parameters.

This parameter estimation is a similar procedure as is done in the ASAID software [Bindschadler et al., 2011b]. However these parameters are then used to extract a grid of elevation values [Bindschadler et al., 2011a]. While in this proposed method the photoclinometric relation is used to correct the miss-alignment of the laser profiles. If coefficients are known, then ICESat GLAS measurements can be interpolated onto the reference track. This correction is done along a photoclinometric line.

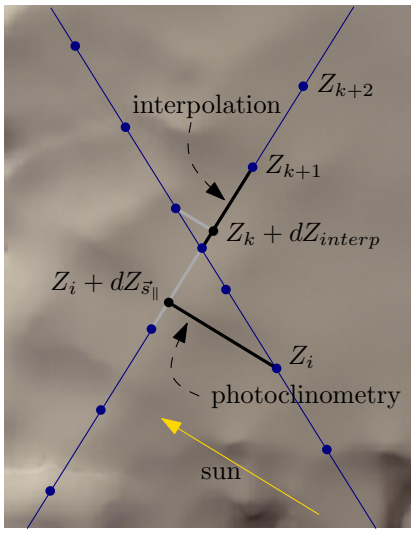

Figure 4.4: Visual illustration of the estimation procedure to extract the photoclinometric coefficients, with the help of ICESat GLAS tracks.

4.3.4 Data

All laser altimetry campaigns of the ICESat GLAS instrument are used for this study. For the optical part, a Landsat ETM+ georeferenced image of the level 1G product is used.

Chapter 5

Results & Discussion

In the previous chapters possible methods and approaches were shown that extracted elevation data from optical and laser measurements. This chapter will focus on the use of these methods. Its implementation will show the applicability of the different methods, applied on different case studies. In the first section the photoclinometric procedure is tested. In the second part of this chapter, there will be an inclusion of satellite laser altimetry, to assess precision and reliability. The last section will include an application of topographic correction for spaceborne laser profilers.

5.1 Synthetic data

Inverse modelling In section 4.1.1 the idea was postulated to use inverse theory with the help of a hillshading function. The implementation of this idea was later on described in that chapter. The resulting estimation procedure will first be tested on synthetic data. In that sense the inverse relation and its side effects are more clearly observable, as the shading is not corrupted with noise.

Figure 5.1 illustrates two elevation models. The model at the left is input for the calculation of a shading image. This image is used for the inverse estimation. The resulting estimated elevation model is illustrated at the right of the figure. If the relation would be one-to-one both elevation models would be exactly the same. As can be seen in the figures, the inclinations of the models correspond well along the direction of the sun. However, perpendicular to this direction a trend is observable. Thus the *Levenbergh-Marquardt* iteration gives a minimum, of which many are possible. The connectivity perpendicular to the suns' direction is weaker than on the solar plane.

Stepwise estimation The estimation of a elevation model can also be split up into two steps, as is illustrated in figure 4.1. First the gradient field is estimated, basically this is a projection of a one dimensional vector onto a two dimensional plane. After this estimation the gradient fields are doubly integrated to extract a elevation model [Frankot and

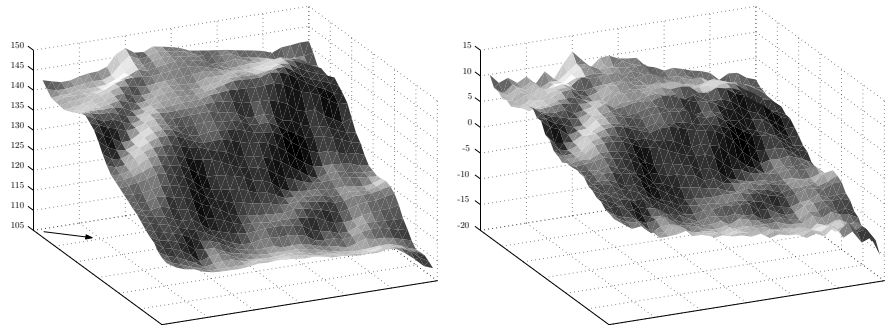

(a) original (b) estimated

Figure 5.1: *left*) Original elevation model, with the shading colored on the surfaces. The black arrow indicates the direction of the sun *middle*) Elevation model calculated through inverse estimation of synthetic shading.

Chellappa, 1988]. An example of result through this procedure is illustrated in figure 5.2.

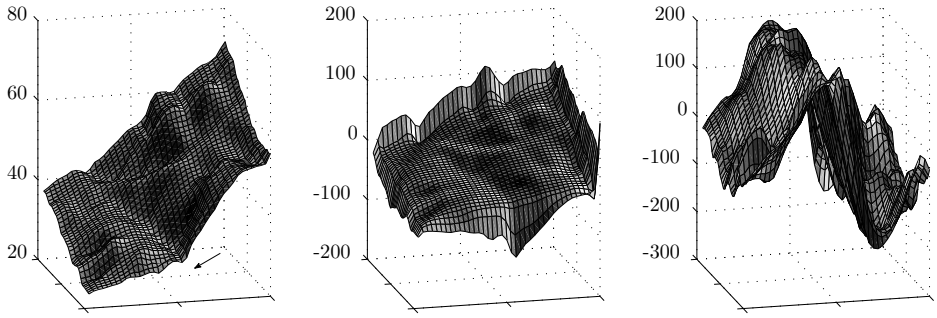

Figure 5.2: *left*) Original elevation model, with the shading colored on the surfaces. The black arrow indicates the direction of the sun *middle*) Direct inverse estimation of the elevation model. *right*) Estimation of elevation model used in two steps; first a gradient field, then integration.

The cause of the artifacts may lie in the integration of discrete estimates, while it is a continues function. Secondly, errors accumulate as the method is not restricted by the photoclinometric profiles. Thus it seems as the full integrated approach of an inverse function is more robust. Furthermore, another artifact of the direct method is observable in the figure. As the estimation in the middle of the model correspond with the input, its border elevations are out of sync. This discrepancy is due to the formalization of the gradient function within the forward model. Elevations values not at the border of the model are attributed to be reliable measurements.

With these relations known, the methodology is applied to spaceborne measurements. This is done through case studies on two different glaciers and an icefield. These case studies follow for a large part the themes from the last chapter.

5.2 Case study I - Zhadang glacier

On the Tibetan plateau, nordwards from Lhasa lies the Nyainqêntanglha mountain range. It is roughly 150 kilometers long, and spans at most about twenty kilometers in width. The elevation of most mountains stand about thousand meters above the plateau. However there are tops that range far higher up, as Mount Nyainqêntanglha with an elevation of 7162 meter. Most northern glaciers of this mountain range drain into Nam Tso lake, that lies at an elevation of 4716 meter. The glaciers are of a summer accumulation type, where both accumulation and ablation processes merge within each other [Kang et al., 2009].

Zhadang glacier ($30.5°$N $90.6°$E) is a high mountain glacier located in the middle of the mountain range, with a surface area of about 2.5km^2. It is oriented northwards, and its elevation ranges from 5500 to about 6000 meter. Temperatures range from $-15°$C in winter, up to $7°$C in summer, at the glacier terminus [Immerzeel et al., 2010]. At the upper part, the glacier is merged on the ridge with the Tangtse glacier, this glacier system is draining southwards.

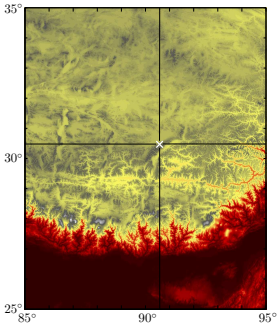

From 2005 onwards there is a glacier mass balance program, maintained by the Institute of Tibetan Plateau of the Chinese Academy of Science. A total of 30 stakes are distributed on the glacier, and snow samples are taken on a regular basis and three Automatic Weather Stations are installed. At the end of the summer of 2011, a geometric survey campaign over the surface of Zhadang glacier was performed. A map is given in the Appendix at figure A.1.

5.2.1 Classification

Before photoclinometry can be applied to the optical acquisition a selection of snow covered area need to be made. Secondly, shadow casted terrain need to be excluded. All this is done through classification of ratio images.

NDSI The ratio image of the Normalized Difference Snow Index over the Zhadang glacier is illustrated in figure 5.3(a). Snow and ice surfaces have high values, even if these surfaces are overcased with shadow. For the extraction of the extent of a glacier, one needs expert or *a-priori* knowledge to find a hard threshold. The extraction of snow covered terrain is done by setting a threshold with the interpretation of other optical acquisitions.

The age of the snow is not easily extractable, but if non glacial terrain has large patches of snow, one can assume the snow surface is not old. Again this is highly depen-

dent on the season and the location and local climate of the glacier.

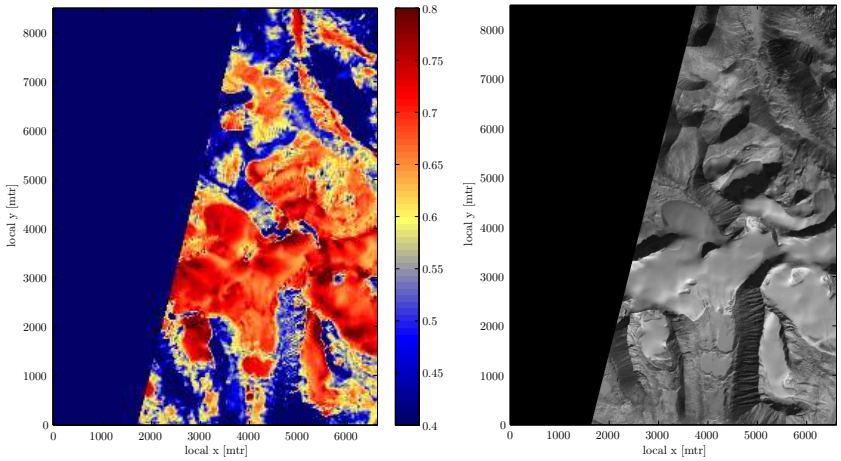

(a) NDSI (b) panchromatic

Figure 5.3: Classification results of the Normalized Difference Snow Index and a subset of a panchromatic acquisition of EO1 ALI over Zhadang glacier.

Shadow Index The sensitivity of the NDSI for shadow casted surfaces is low. However these areas will not be of use in the photoclinometric estimation. The shadow index described in the previous chapter may be of help in the identification. Its computational results are illustrated in figure 5.4(a).

If the result is compared with the panchromatic image illustrated in figure 5.3(b), or the hillshading in figure 5.4(b), one can see a clear correspondence and agreement. Even the shadowy lanes caused by gullies, on the mountain ridge in the South, can be identified. Conscience should by taken when thresholding is applied for the classification. If this is done loosely, mixed pixel will be included, which do not follow the photoclinometric relation.

5.2.2 Surface estimation

An elevation model was estimated over the tongue and the middle part of the Zhadang glacier. The EO1 ALI acquisition is from the 29^{th} of January 2004, when the sun stood in South East direction, at an azimuth of $147.4°$, its elevation was $34.8°$ above the horizon. One can assume that the glacier is covered by snow, though it may not be fresh, as the surrounding terrain is free of snow. However it may not be old snow as the winter of 2004 had prevailing snowcover [Kropáček et al., 2010], and it seems as if there were at least three snow events occurring that month in the Nam Co region. The resulting estimate is illustrated in figure 5.5.

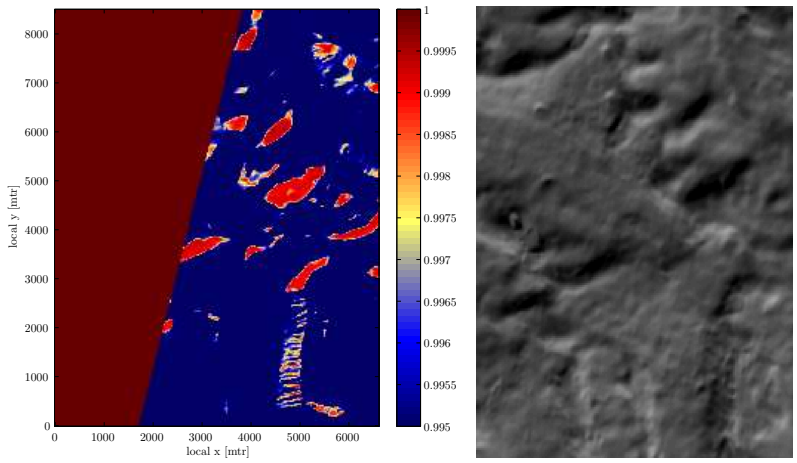

(a) Shadow Index (b) ASTER GDEM hillshading

Figure 5.4: Classification results of the Shadow Index and an hillshading calculated with the elevation model ASTER GDEM, the orientation of the sun is in the same direction as the EO1 ALI acquisition, of which the index is derived.

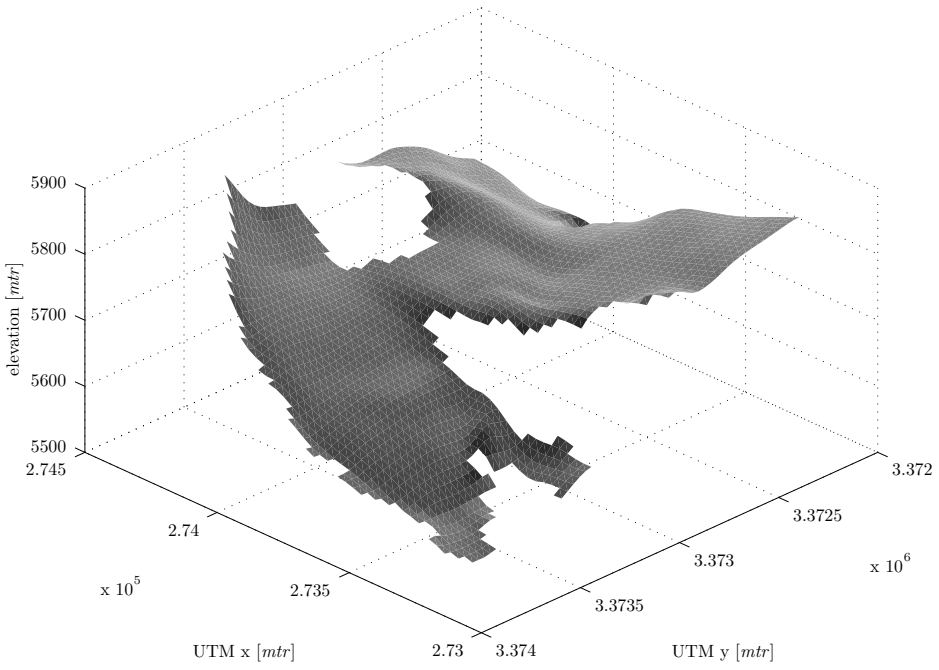

Figure 5.5: Optical imagery draped over photoclinometric estimation of Zhadang glacier.

Gaps in the estimate are the result of exclusion through classification, as previously described. In the figure, the sun is opposite of the viewing direction. Here one can see that the overall shape of the glacier tongue and saddle seems to be in correspondence

with its real world appearance. This is apart from a small section at the leftmost side, where the estimation gradually gains elevation. Discrepancy of this estimate is partly due to the low connectivity to the rest of the shading. The ambiguity in azimuth is solved, but results in a hillside in an opposite direction. Relative surface angles with the sun variate widely for this glacier ($\approx 5° \ldots 45°$), this may have an effect the reflection pattern as volume scattering may be taken into account, as can be seen in figure 2.7.

Qualitative verification of the estimated shape is rooted from two independent sources. First the spatial coherence of the estimate can be checked by an ASTER GDEM. ASTER GDEM is a dataset constructed from stacked automatic created spaceborne DEM's [Tachikawa et al., 2011]. These automatic constructed DEM's are based on satellite photogrammetric procedures done by SILCAST software [Fujisada et al., 2011]. The specified precision of the product is one meter, while horizontal and vertical accuracy is respectively 20 and 30 meters.

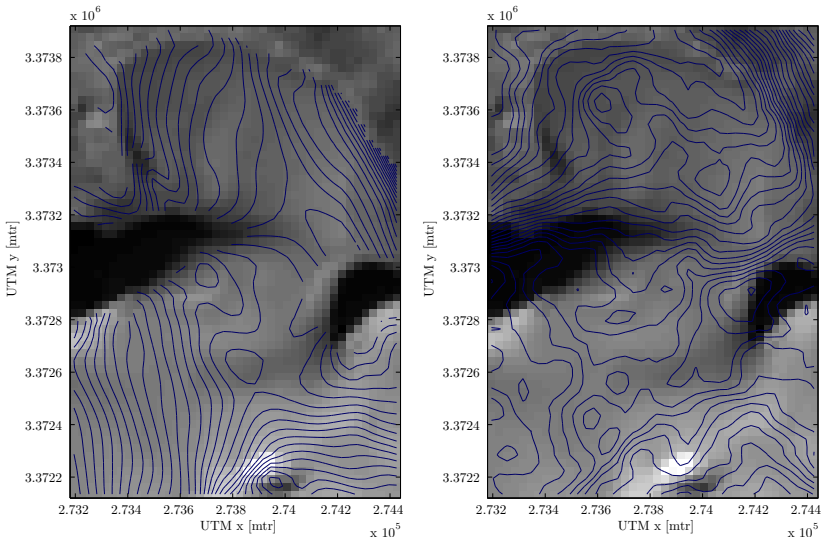

(a) shape estimation (b) GDEM

Figure 5.6: Contour plot of surface estimation, and ASTER GDEM2. In the background is the EO1 ALI scene used for the estimation. The interval of the photoclinometric elevation model is arbitrary, the ASTER GDEM2 contour interval is 12.5 meters.

The different elevation models are illustrated in figure 5.6. Holes and edges clearly corrupt the global shape. Local trends along the sun direction do correspond with the shape of the glacier. But strong tendencies are visible perpendicular to the sun direction. These artifacts seem to have an linear trend.

The estimated shape is first translated to be aligned in line with the ASTER GDEM. In that sense, it can be compared with other measurements. To compare the shape with the elevation model the scale factor and vertical offset are estimated through linear least squares adjustment. The strong correlation between the vertical offset and scale factor

may be of concern. The least squares adjustment of a elevation model with a bias within, does strongly influences the reliability of the unknown parameters.

Other registration methodologies did not seem to be possible, as the photoclinometric estimation is an irregular patch, including holes. Hard classification excluded mixed pixels, consequently eliminating other elevation data that may be used to register the surface model. Especially the mixed pixels of shadow and snow corrupt the shape estimation. This property is unfortunate for the alignment with other elevation products, these have mostly reliable elevation estimates at these edges, e.g.: rock outcrops, glacier terminus. Thus an area based registration was applied.

Other ground truth is available by means of a survey transect. This transect is measured during a field campaign in September 2011. First terrain features where selected, and jalons were placed. These were measured with a dual frequency GPS receiver. Tachymetric angles and distances were measured to these features, to estimate the orientation and coordinate parameters of the tachymeter, *i.e.:* backward intersection. With this known orientation it was possible to sample other terrain features, to extend the network of known points, *i.e.:* forward intersection. Rock outcrops and boulders were used, that during the campaign were measured from multiple positions. After the orientation was completed, measurements were taken to a prism. A transect along the major flow line was measured and coincides with a ground radar campaign, that was measured at the same time. Its trajectory runs from the snout almost up to the saddle. Measurement precision of the data was estimated a RMSE of vertically 2.8 and horizontally 1.4 meters.

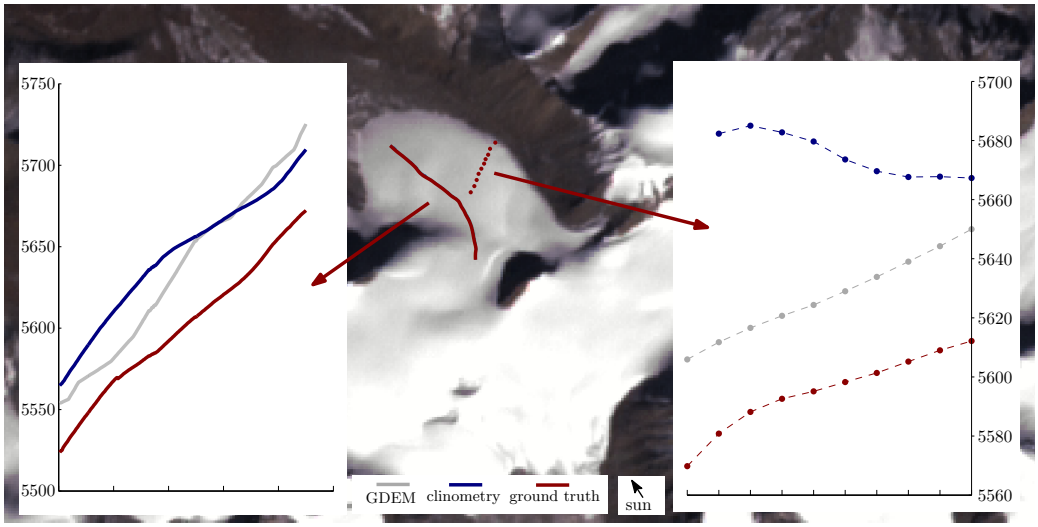

Figure 5.7: Optical satellite image of Zhadang glacier. Survey results are indicated in dark red. The estimated elevation model is outlined in darkblue and the ASTER GDEM in gray.

The elevation profiles of the datasets are illustrated in figure 5.7. The leveling profile

is mostly in the same direction as the sun vector, while the stakes are oriented roughly perpendicular to that. A bias is observable for the leveling profile in respect to the elevation estimate. This is probably due to the wrong orientation in respect to the GDEM.

Leveling started at the snout of the glacier, however as can be seen in the figure, it does not on the imagery. This may be due to a retreat of the snout, and a misalignment of the satellite acquisition. Glacier outlines indicate a retreat of up to 200 meters for Zhadang glacier over recent years [Bolch et al., 2010]. Consequently the estimate can be seen as a good relative approximation for its time stamp. The ASTER GDEM shows a different pattern, it has more bumps and is steeper. Stake measurement that stand perpendicular to the sun show a systematic bias, this was also observed in figure 5.6(a). Here the ASTER GDEM is globally of better reliability, while the photoclinometric elevation estimate gives a good local estimation.

Local regularization Trends perpendicular to the direction of the sun occur, as is observable in the estimations above. These artifacts are caused by the connection of photoclinomtric lanes to each other. Regularization within the iteration process may influence this stitching process. A constraint on minimal curvature, as described in section 3.2.3, may force the iterator to end up into a local minimum with a linear trend, instead of one with a higher order trend.

A result of the implementation of constraints within the shape estimation is illustrated in figure 5.8. The constrain on curvature is only imposed to the elevations in the middle of the elevation model. Elevations at the border of the grid or classification selection are excluded. Therefore these elevation are extremely large compared to their neighbors. Weighting of the regularization was applied, but due to the non-linear relation this was difficult to implement. Therefore, the use of constrains is not of benefit to a good shape estimate. Thus these constrains are left out of the estimation procedure. This formalization problem may be solved by describing the orientation in term of position on the unit sphere [Ikeuchi and Horn, 1981].

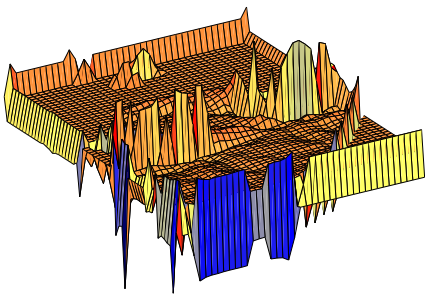

Figure 5.8: Shape estimation of Zhadang glacier with the use of a constraint on curvature.

Photoclinometry can give inferences about the surface shape. Large local variations are visible in the difference image with ASTER GDEM. This may be due to the ASTER GDEM noise, the registration, volume scattering, or the photoclinometric computation. An artifact observable in the leveling and ASTER GDEM is the hillside in the NorthEast. Due to classification, this part has low connectivity with others. It deviated as the azimuth ambiguity was solved in an opposing direction.

The following case study will be on a low sloped icefield, normal vectors will not change dramatically in respect to the sun, as with Zhadang glacier. In that case, the *Lambertian* reflection function may be more fitted. Secondly, an attempt will be made to

approximate the registration unknowns, *i.e.:* scale factor (λ), planar rotation (v, u), and vertical bias (Z).

5.3 Case study II - Lomonosovfonna

On the central island of Svalbard, Spitsbergen, lies the Lomonosov icefield, at roughly $78.5°$ North $17°$ East. It is the main accumulation area for several tidewater glaciers, *e.g.:* Mittag-Lefflerbreen, Nordenskiöldbreen, Negribreen, Hinlopenbreen and Tunabreen. The hypsometry for this glacial system ranges from its highest point on 1250 meters and ranges down to sea level.

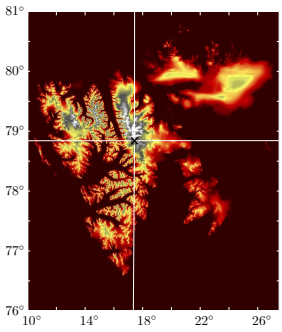

Up to the year 2000 Nordenskiöldbreen lost ice due to iceberg formation. However, nowadays its production stopped as the front of the glacier terminates on land. The calving process may start again, as RADAR measurements revealed bedrock topography below sea level that was situated just after the snouts position [van Pelt et al., 2012].

Research is mostly conducted on Nordenskiöldbreen where since several years different instruments are placed. Stand alone single frequency GPS measurements conducted in recent years measured an annual surface speed of 40 to 55 meters along the central flow line [den Ouden et al., 2010]. Stake measurements over a period of 1989 to 2010 indicated a mean net mass balance of -0.39 *m w.e.* [van Pelt et al., 2012]. Topographic surface conditions on Lomonosovfonna can change rapidly due to the strong polar eastern winds coming directly from the Barentz sea [Pohjola, *pers. com.*]. A map illustrating some of the data is included in the appendix, *i.e.:* figure A.2.

5.3.1 Classification

Cloud detection In the optical acquisition of the EO1 ALI sensor over Lomonosovfonna clouds are hanging above the topography. The distinction between snow and clouds in the visible imagery or NDSI is not able to distinct these different phenomena enough. A ratio image over wavelength centered at $0.55\mu m$ and $1.25\mu m$, resulted in a better distinction, as can be seen in figure 5.9, this is based on figure 4.2.

The bulk of clouds can be identified, but on these edges are cirrus clouds that have a fairly similar reflection in respect to fresh snow. Thus apart from a threshold on the ratio image, a local range filter was used to detect the edge. To ensure all cirrus clouds were eliminated, mathematical morphology was used to buffer the detected clouds. The result of all classifications are showcased in figure 5.10. Here one can see that even smaller cirrus clouds on the icefield were identified, like in the right part of the figure.

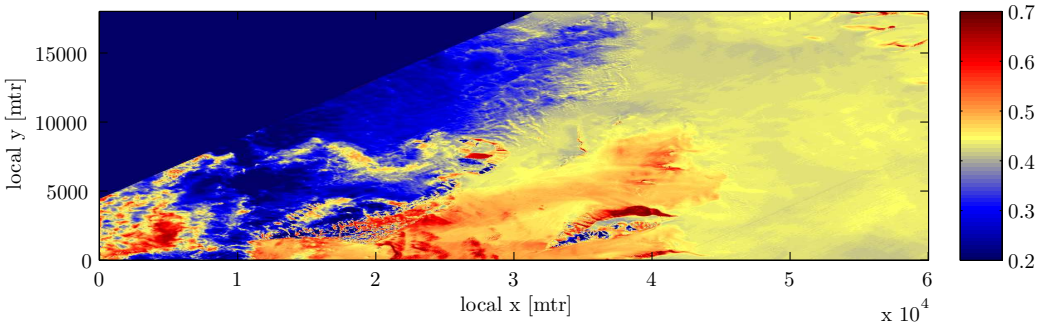

Figure 5.9: Subset of EO1 ALI image over northern part of Lomonosov icefield. The darkblue patches are clouds, in the bottom right is the Nordenskiöldbreen located. In the center is an rock outcrop visible, and on the right is the icefield.

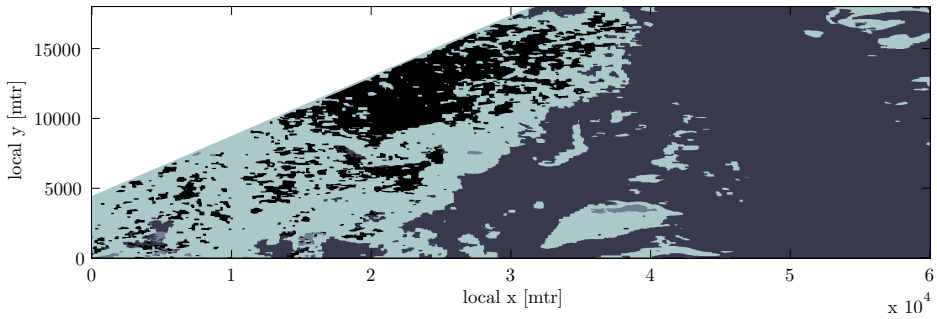

Figure 5.10: Classification of EO-1 ALI acquisition over northern part of Lomonosovfonna. Different colors indicate water (*black*), snow (*darkgray*), shadow (*gray*), and clouds (*lightgray*).

5.3.2 Global regularization

The size of the design matrix for a elevation estimation increases quadratically in respect to the size of the shading. Thus computational limits can be crossed when big matrices need to be inverted. Therefore only small patches of shading can be input for the estimation. If a elevation model over the whole of Lomonosovfonna should be calculated, more advanced estimation processes are needed. Two approaches were tested, a top-down method (quad-tree) and a bottom-up method (recursive).

Every higher level within the quad-tree is constructed from interpolation over four lower lying neighboring image cells. At the highest level a elevation grid is estimated over the total area. This elevation is split into four grids and brought into the grids that have a finer resolution. They function as an initial elevation estimation, where τ is set to a high level, to steer the iteration into a local iterator, see fula 3.23. In that sense the global shape of the terrain is brought into the estimation, and finer elements are included along the way down the quad-tree. However the estimation at the border has a small offset, as was mentioned in the former section. Due to this offset the resulting elevation esti-

mate gets a blocked shaped pattern over the elevation model. A structure of overlapping quad-tree cells may solve this problem, but this structure was considered to be too complex to implement.

A bottom-up approach was implemented in the form of a *Helmert-Wolff* blocking structure. To overcome the problems of the bordering offset an overlapping structure was created. Individual blocks were calculated and the elevation estimates aligned in a global estimation. These estimates were brought back into the local estimation and refined through *Tikhonov*-regulation. After some recursive steps a global consistent elevation estimation was pursued. Resulting estimates had higher order trends within the model. If local divergence of a elevation patch occurred it could hardly be turned around.

Occurring artifacts within the estimation of both approaches do not seem to outweigh the benefit of implementing them. Consequently the size of a elevation model estimation through photoclinometry with an inverse function will be limited. Thus only small patches can be estimated, depending on the computation power of the system.

5.3.3 Registration

If the iterator can only solve small surface patches it has consequences for the type of registration. Glacier wide registration, using multiple ICESat GLAS tracks separated kilometers apart, is not possible. The spatial resolution of the imagery resolve in surface models with a spacing of at least 30 meters. This resolution is insufficient to model within-footprint profiles. Therefore, the only range at which registration with laser remote sensing seems possible is along profiles. Methodologies within this extent are worked out below.

Different approaches can be chosen to orient the shape estimation into a elevation model. To assess these procedures a site off 900 by 900 meter was chosen on the upper part of Nordenskiöldbreen. Two photoclinometric elevation estimates were calculated. One originated from an EO1 ALI image, that acquisition has a high radiometric resolution and a spatial resolution of 30 meters. The sun had an azimuth of $198.6°$ and an elevation of $31.1°$. The other estimate is rooted from a TERRA ASTER image, which has a lower radiometric resolution, but a spatial resolution of 15 meter. During the acquisition the suns stood $31.8°$ degrees above the horizon with an azimuth of $212.4°$. To assess the orientation and shape estimates, a DGPS track of a snowscooter was used. The data is illustrated in figure 5.11.

The absolute orientation can be done by writing registration parameters in a polynomial fashion and estimate them through least squares adjustment, as in formula 4.3. A simple manner is found in using all elevation measurements that are along an ICESat GLAS profile. The surface grid is related to the ICESat GLAS measurements by interpolation using a *Delaunay*-triangulation. These measurements are used to solve the registration unknowns. If the instrument is seen as an radiometer some unknowns can be resolved by calibration coefficients. Radiometric coefficients relate the reflection function to the digital numbers. Standard calibration coefficients and solar reflective correction were used into the estimation computation [Chander et al., 2009], [Thome et al., 1998].

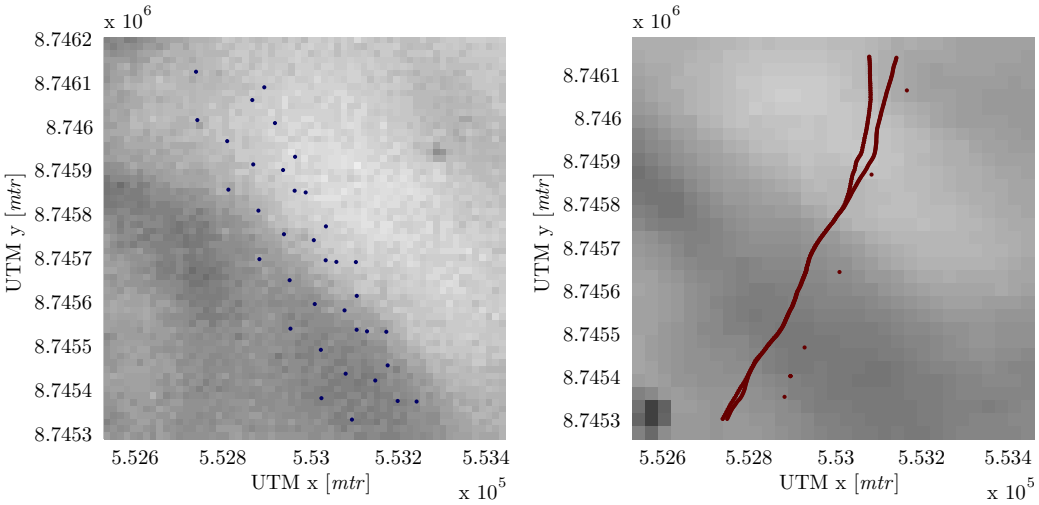

Figure 5.11: *left*) optical acquisition over Nordensskiöldbreen of TERRA ASTER. The darkblue dots indicate ICESat GLAS measurements. *right*) subset of EO1 ALI image over the same area. The darkred dots indicate snowscooter tracks measured in April 2011, with courtesy of Veijo Pohjola, Uppsala University

The atmospheric term is unknown and set to zero, similar to [Bindschadler and Vornberger, 1994]. The resulting range is the at-sensor spectral radiance, directly used to estimate the shape. But as is already denoted in section 3.5.2, the reflection model is proportional. Thus the reflection of snow should be multiplied by the at-sensor range, to have a good correspondence between the measurements and the model. This reflection is estimated to be 0.8, this factor is taken from figure 2.6. The resulted shape estimate for the sample site is shown in figure 5.12

The estimated elevation models do not correspond well with the measured elevations from the snow scooter or the laser profiler. This is mostly due to a scale factor that seems to be to large. Errors in the radiometric coefficients may be present, but these would not produce offsets in this order of magnitude. Most probably the error is rooted from a miss-quantification of reflection. This factor is highly related to the scale factor, but the in situ reflection of the surface is unknown.

The scale factor can also be included into orientation estimation as an unknown parameter. In this manner the radiometric coefficients are of good help for a rigid approximation of the shape. Again the orientation can be estimated by linear least squares adjustment. If all ICESat GLAS measurements are brought into the equation, the horizontal distribution of the samples is more spread. Results from this type of registration is illustrated in figure 5.13. Consistency is present in the middle of the image, due to the ICESat GLAS measurements at that position. At the outer side of the figure, the shape is in correspondence with the original, however a systematic deviation is present. A better distribution of ground control points is needed to minimize these effects. Difference in radiometric and spatial resolution gives different outcome to the surface estimation. It

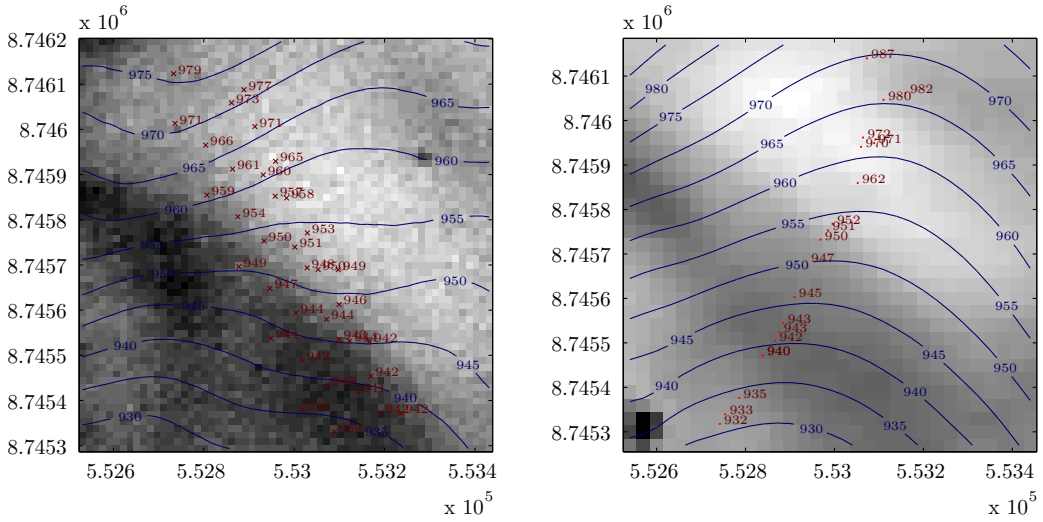

Figure 5.12: The satellite imagery is illustrated on the background of the site illustrated in figure 5.11. Axis of the figures have the same scale. A contour lines in darkblue of an oriented elevation model are draped over. For the orientation only a trend in both axis and absolute elevations were used, the scale factor was extracted from radiometric coefficients. *left*) TERRA ASTER elevation estimate, The darkred crosses illustrate the ICESat GLAS measurements. *right*) EO1 ALI elevation estimate. The darkred dots indicate some DGPS measurements from snowscooter tracks measured in April 2011, with courtesy of Veijo Pohjola, Uppsala University

seems as if a higher spatial resolution is of more benefit then a higher radiometric sampling rate. Spatial details are better observable in the estimate of the ASTER scene, while better inclination accuracy, due to the sampling rate, is not clearly observable. The panchormatic band of Landsat could have been used as it has also a high spatial resolution, however its information content seem to be in the same order as the normal bands [Heid and Kääb, 2012].

In the registration formalization and estimation, the scale factor is heavily correlated with the other components. These components can be approximated in a piecewise manner, but this will result in a suppression of the scale parameter. This is due to the profiles that have high elevation values and are slowly undulating, their approximation is close to planar. Secondly, deviations are present in the ICESat GLAS profiles, due to temporal surface changes. Measurements were taken at different time stamps, while the estimated surface geometry is an estimation from optical imagery somewhere acquired within the ICESat GLAS measurement campaign.

To take seasonal and annual changes into account, parameters for time may be included into the model. A simple manner is by assuming a linear trend. This model may be applicable for large time spans of several decades. In that case the glacial retreating or advancing signal may be larger then its seasonal gain and loss. However the time span

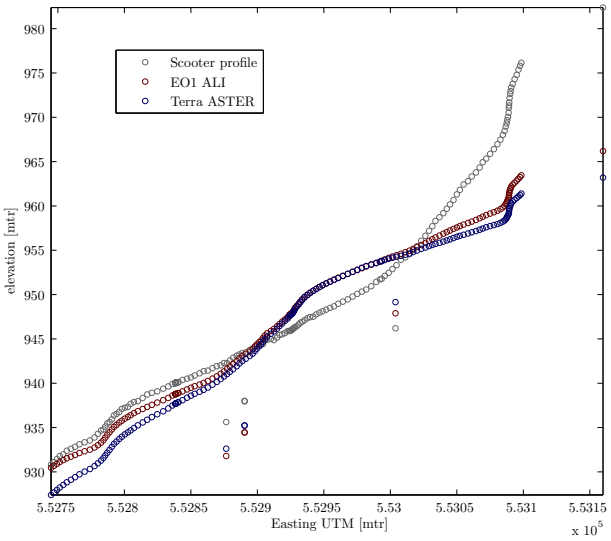

Figure 5.13: Elevation values of the scooter transect, as shown in figure 5.12.

for this study is to short for a rough model approximation like that.

A simple model over time can be used, if the selection of ICESat GLAS measurements are chosen wisely. For example, measurements taken in autumn have a high chance of being snow free, thus during that period the the seasonal signal is minimal [Kääb, 2008]. However surface conditions need to be known in that case. As this is not totally valid for this case study, the model in the time domain needs improvement. An option of an annual sinusoidal curve can be included into the model, similar to [Slobbe et al., 2008].

Surface elevation measurements of a sonic ranger on an automatic weather station on Nordenskiöldbreen over 2006 showed a triangular wave pattern [den Ouden et al., 2008]. Other snow surface measurements over a longer period on the Austfonna icecap did show a similar periodicity [Østby *pers. com.*]. The precipitation pattern and surface conditions seem to be similar for the weather station of Austfonna and Lomonosovfonna [Rotschky et al., 2011]. Thus a skewed triangular wave is brought into the orientation estimation, as formulated in [Weisstein, 2012]. The phase of the wave is not adjustable, however the onset of the summer melt seems to have deviations of 10 days over recent years [Rotschky et al., 2011].

The constructed models described above becomes more and more complicated. They aim at a better representation of the real world situation, mostly done by including more parameters. Due to this increase in parameterization the distribution of samples within the sampled site becomes more important. The sampling of the profiles of the laser ranger is along one certain track. If time dependency is included into these models, the tilt perpendicular to this track is also influenced by a function through time. By including an annual sequence into the registration only short term processes are modeled. The more annual or decadal trends should also be included into the registration. However,

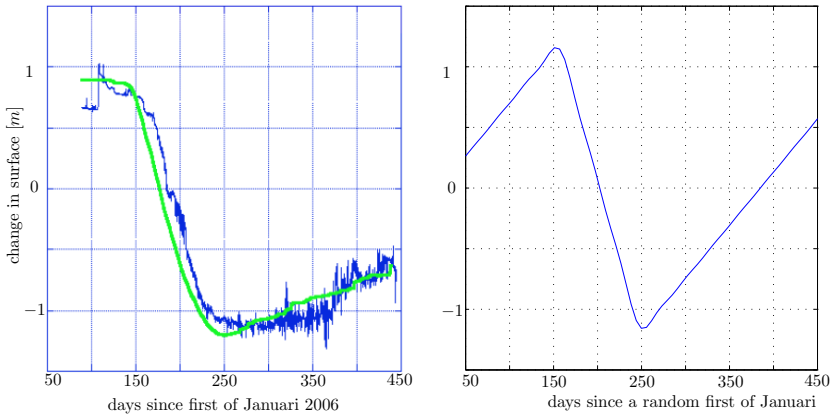

Figure 5.14: *left*) Graph of sonic ranger measurements from an automatic weather station, situated on the upper part of Nordenskiöldbreen. The illustration is taken from [den Ouden et al., 2008]. *right*) A skewed triangular wave describing the topographic variation observed by the sonic ranger measurements.

for the Svalbard peninsula the annual elevation changes do not seem to be fitted by a linear trend over the period of the ICESat GLAS campaigns, as can be seen in figure 5.15. More complicated polynomial function need to be included, but this results in over parametrization. Furthermore, the campaigns of ICESat GLAS are fairly limited over time to reliably estimate the pattern of the triangular wave, as can be seen in the figure. The inclusion of temporal short term surface change within the registration model, seems to be to difficult.

Another approach is found in the integration of photoclinometry and registration. A better distribution of ground points is needed, as the aligned sampling pattern of a profile may have no influence on the photoclinometric function. Therefore, a crossing of two lanes is taken on the upper part of Lomonosovfonna. All ICESat GLAS elevation measurements are brought into the estimation. Applying this idea resulted in a elevation model with irregular bumps and spikes. These irregularities are rooted from the noise in the image and laser profiler, but also simplifications within the model. The estimated photoclinometric constants are a global parameter, there they are less effected by these bumps. However this integrated approach is computer intensive and the results are discouraging.

If a crossing of two ICESat GLAS profiles is approximated by a planar surface, the residuals assemble the shape. These points can be related to the elevation model, where the scale factor and trends can be estimated. The estimated shape and its parameters are combined with the planar surface resulting in a elevation model. This model is used to estimated the photoclinometric coefficients. Multiple unknowns need to be solved, one crossing is not sufficient, hence two profile crossings scattered over Lomonosovfonna were brought into the calibration process. Their elevation estimation is illustrated in figure 5.16.

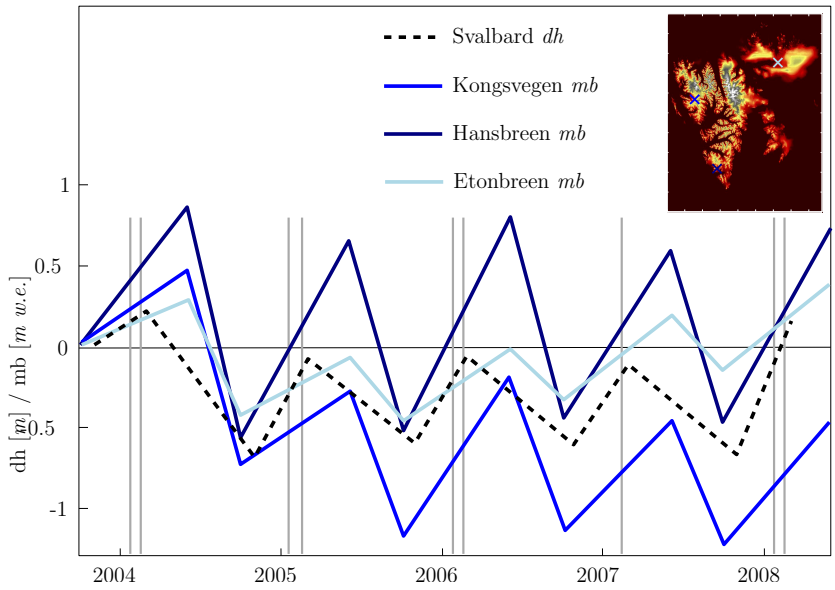

Figure 5.15: The dotted black line connects averaged elevation changes (dh) of ICESat GLAS measurements over whole Svalbard. The measurements are grouped into seasons (October $\leftrightarrow$ March). The other lines connect mass balance measurements over three different glaciers, as are indicated in the inset. These measurements are in meters water equivalent, also the time interval is different (September $\leftrightarrow$ May). The illustration is taken from [Moholdt et al., 2010b]. The vertical dark gray lines indicate when measurements of ICESat GLAS where conducted over Lomonosovfonna.

The resulted elevation models can now be used for calibration. Where the shading of the estimated elevation model should be equal to the digital numbers of the satellite acquisition. Their relation to the optical acquisition is linear but a bias exists, as can be seen in figure 5.17. This may suggest the relation is not heavily correlated, and a direct relation is not possible to formalize. The reflection model may be unfit as the snow may be old, or the snow state may be different on both places. Other components may interfere with this relation, and while in Antarctica ($R^2 = 0,67$) [Bindschadler and Vornberger, 1994], and Austfonna ($R^2 = 0,84$) [Bingham and Rees, 1999] high correlation values are found. It may not be the case for glaciers and smaller icefields, as this study shows and is also found on Langjökull ($R^2 = 0,45$) [Pope, 2009].

Thus photoclinometric coefficients can not be estimated in a reliable manner. Therefore, the estimation idea as shown in figure 4.3, is not possible to implement. Consequently, only crossings of ICESat GLAS tracks can be oriented in a robust manner, if the time interval of a crossing is short enough. For glaciological research this may not be of much interest. If an idea of the distribution of volume change is wanted, the information is limited. The tracks on itself give more information, however these measurements are not repeated perfectly. Although, the orientation of a photoclinometic elevation model is limited, photoclinometry may still be used to extract information. If elevation measurements over an ICESat GLAS track are plotted the differences are partly caused by

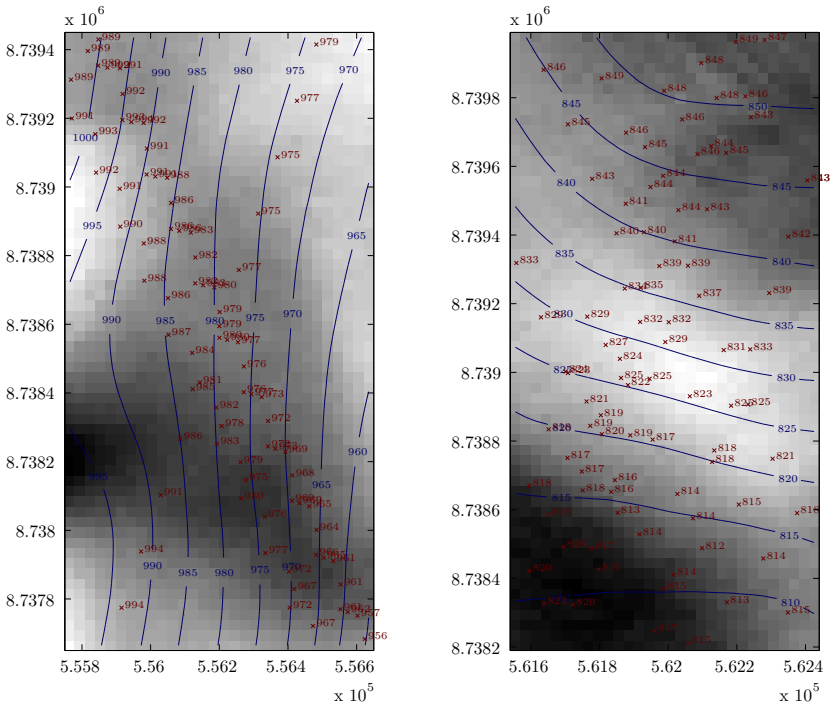

Figure 5.16: An EO1 ALI imagery is illustrated on the background, axis of the figures have the same scale. Contour lines in darkblue of an oriented elevation model are draped over. For the orientation a cross over was used, the parameters estimated are trends in both axis, absolute elevation and the scale factor on the vertical axis. The darkred crosses indicated ICESat GLAS measurements over different time stamps.

the mass balance and flux, see formula 2.7. But the other part is caused by the horizontal miss-alignment of the profiler. Topographic correction for these measurements might by extracted through photoclinometry. In that sense the observed elevation change is directly related to surface dynamics. For the implementation of this idea a site on Austfonna is chosen.

5.4 Case study III - Basin 3

On the eastern part of Svalbard archipelago lies Nordauslandet, at roughly 79.5° North 25° East. The majority of this island is covered by icefields, where the icecap of Austfonna is the largest piece of land ice, with an surface area of 8450km^2. Basin-3 is one of the several outlet glaciers of Austfonna with a size of roughly 1271km^2 [Hagen et al., 1993].

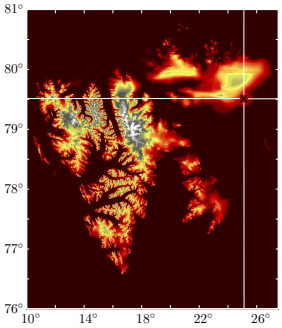

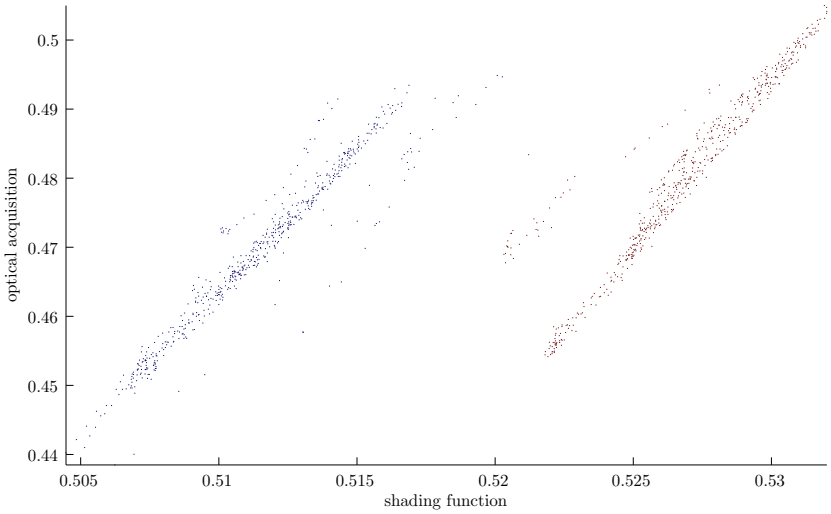

Figure 5.17: The relation between an synthetic elevation model function and reflection values of an optical acquisition. The darkred scatters are related to the sampling site on the left side of figure 5.16, the darkblue scatters are related to the figure on the right.

This outlet glacier ends at the Barents Sea where it produces icebergs. In the mid nighties surface velocities shortly increased to 140m/yr [Dowdeswell et al., 1999]. Later on its velocity regime declined to 80m/yr, indicating a mini surge. In recent years another speed-up has been observed [Dunse et al., 2011].

On most of the islands of Svalbard aerial oblique photographs were taken in 1936 and 1938. These images were used for the topographic map series at scale of 1: 100 000. More aerial campaigns were conducted in the period between 1960 - 1971. A more detailed map series was produced based on phototgrammetric principles on these vertical aerial images. However all the time the island of Nordaustlandet was not included.

Eventually in 1983 a elevation model was constructed from airborne radio echo-sounding measurements [Dowdeswell et al., 1985]. The newest topographic dataset is constructed from differential SAR Interferometry (DinSAR) controlled by the aid of ICE-Sat GLAS measurements [Moholdt and Kääb, 2012]. Again this elevation model has a limited accuracy, as RMSE estimates are in the order of ten meters. Thus detailed topographic information is absent, therefore making a ideal test case for the proposed methodology in this work. An overview of the glacier is illustrated in figure A.3.

The Landsat ETM+ imagery was taken at June 17, 2001. During the acquisition the sun had a elevation of $32.4°$, and an azimuth of $206.9°$. A transect from the upper part of the Austfonna ice cap up to the calving front was selected. For calibration the intersection of two transects were taken. New horizontal coordinates for the measurements were at the intersection of the track along the direction of the sun and the reference track. The corrected measurements are shown in in figure 5.18.

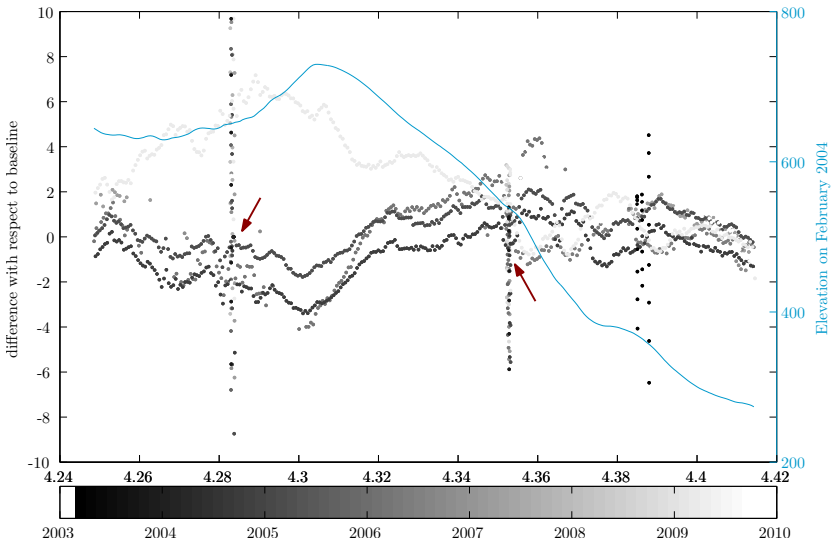

Figure 5.18: Difference in elevation measurements from ICESat GLAS which are corrected to lay inline with its reference track, in respect to the samping in Februari 2004. The absolute elevation of this profile is indicated in lightblue in the background.

For a large part this profile crosses the glacier of Basin-3. A gradient of elevation change should be observable, as the flux term has changed in recent years. To assess if the presented results can reliably interpreted the raw measurements are shown in figure 5.19. In both figures a group of elevation measurements is highlighted by a darkred arrow. These are measurements of a crossing, and were included in the estimation as a buffer selection around the transect was made. In the figure 5.19, these measurements are at the same level, while in 5.18 these deviate. Thus the correction applied to the ICESat GLAS measurements made the estimation worse.

Errors in this methodology may be rooted from different sources. The orientation of the calibrated sites may have a different orientation. Secondly, the prominent topography may not lie in the direction of the sun. Thirdly, grain size may affect the direct relation with inclination.

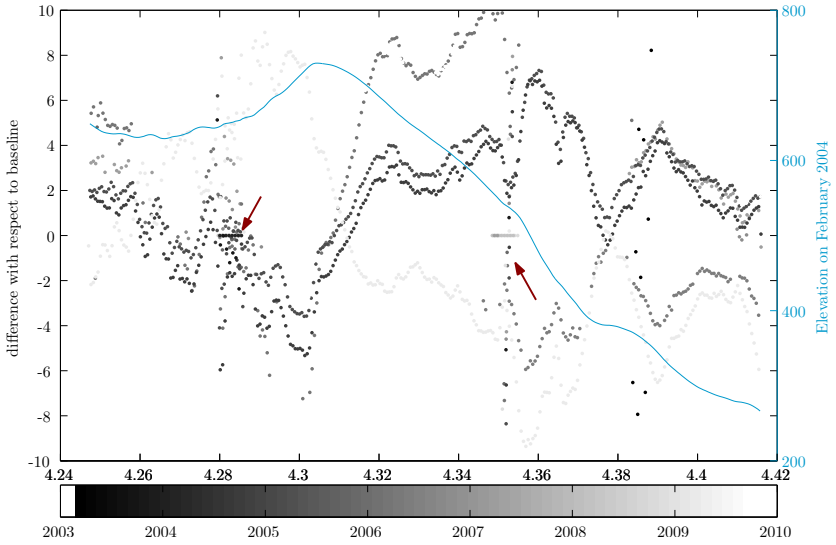

Figure 5.19: Similar illustration as figure 5.18, however the measurements are not corrected though photoclinometric information.

Chapter 6

Conclusion & Recommendation

Model based inversion of the shading function into a elevation grid is a simple idea, but has several practical challenges. An attempt was made to increase the level of information content by integration of spaceborne laser profile measurements. This chapter will highlight the main conclusions, by answering and discussing the research questions, which were given in section 1.2. Recommendations concerning further in depth research or different approaches and applications of this work are given afterwards.

The main research question of this work is,

Can elevation measurements of a glacier surface be extracted through a combination of optical and laser remote sensing techniques?

In glacier mapping the use of (spaceborne) photogrammetric principles is normal practice for extracting elevation models. The aid of spaceborne laser profilers for ground control points in remote areas are of great value. In the snow-covered upper part of a glacier the optical sensors senses less contrast, due to the homogeneous reflection of the surface. Therefor photoclinomtery can complement these areas where image matching becomes troublesome, or improve the spatial resolution.

In this study an iteration process based on inverse hill-shading was used to estimate a relative elevation model. The unresolved parameters for absolute registration where extracted from laser profile measurements. Three different scales can be distinct, a glacier wide mapping, transect based estimation and within footprint elevations. The first and last option have both theoretical and practical objections.

If a glacier-wide estimation covering different transects is applied, this will lead to an enormous design matrix. These heavy sized matrix inversions that are needed to solve the systems of equations are limited by computer memory. Trying to solve a patchwork of elevation models in a recursive manner did not resolve in a stable estimation. Estimating through individual profiles is more computer friendly and can result in a elevation model [Bindschadler et al., 2011b]. In this manner the practical objection is bypassed, but the resulting product is effected by accumulating errors. Thus this product is useful for detecting changes or breaklines, but less interesting for volume change estimation.

A local approach would be found in the withinfootprint estimation of an ICESat GLAS measurement. For this study the used sensors have a too big spatial resolution to estimate a detailed elevation model for this purpose. Other sensors should be used, like ALOS PRISM. Another challenge is found in the uniqueness of the elevation estimate. It is not a linear mapping, as the same waveform can be the result of different elevation models.

The drawbacks mentioned above justify the approach taken in this study; assessing the potential of regional glacier elevation estimation. Photoclinometry seems to be applicable in local sampling sits that have small variations in height. Due to the dynamic behavior of glaciers, the surface changes rapidly, thus repeated ICESat GLAS passes are difficult to combine. A profile can only be used, resulting in an unfavorable sampling distribution. If a crossover of two profiles is used a local elevation model can be oriented. However, using these overpasses to estimate the photoclinomteric constants for global purposes seems unsatisfiable. Thus this method is only usable on cross-overs, which is only of interest for the two big icesheets. Therefor one can conclude that combining photoclinometry and spaceborne laser profilers may be less applicable. But this method has potential as more advanced spaceborne laser profilers are launched, like ICESat2.

An area based approach is a complicated simplification and its product is difficult to interpret. Furthermore, over parameterization is easily accomplished. It even seems as if some proposed methods result in estimations that are within the noise level of the instruments or model errors. Therefore an other approach is also taken within the work, focusing on topographic adjustment within different tracks. By these means it is possible to extract more clearly other signals then glacier elevation. But the model used in this study was to simple, however if an area based approach is used, it may have potential.

Apart from the general conclusions outlined above, some more specific research questions were asked, these and there answers are given below.

- ⋆ *What kind of information is needed for glaciological research?*
  The registration of an photoclinometric elevation model is possible at crossings. On other part of the glacier, this may be troublesome. Thus volume change estimates may not be the best product to produce with photoclinomtery. This method may better be used for individual elevation measurements, like topographic correction, as in this study.

- ⋆ *Is it possible to derive a unique surface of normals from a optical image of snow covered terrain, through photoclinometry? And what are the preferable circumstances concerning surface characteristics, sun direction and sensor?*
  Different optical acquisitions of different sensors, with different sun angles result in a similar estimation of shape. Most area based photoclinometric methodologies use constraints on curvature to enforce the solution to a smooth model. If the sun's orientation is not aligned with one of the image axis, the estimation will give a smooth estimation. For cases the special case where this is valid, a planar rotation may solve this computational problem. The information content perpendicular to

the sun's direction is low, therefor the cumulative elevation errors are bigger in this direction. Due to the connectivity of the elevation grid, these errors have the form of simple trends. Thus after adjustment a unique surface may be extractable.

Photoclinometry may not be the best option for small high mountain glaciers. Outcrops and ridges result in an irregular patch of shading, this may be a disadvantage for the coherence with the photoclinometric relation. Secondly, the *Lambertian* reflection may not be valid due to their steeper slopes.

Practically, a low sun angle is preferable. Furthermore, spatial detail seems to be of more benefit then a high radiometric resolution. Assumptions are made about the physical state of the snow surface. In this study these conditions were not derived first handedly, but other remote sensing data can give an idea about local weather conditions. The unset of snow melt can be identified by RADAR reflections, indicating big grains of snow. Coarse multi-band optical imagery can be used to identify regional dumps of snow, giving idea of the age of the snow surface. Finally, the data from automatic weather station can be of good use in understanding the seasonal characteristics of the surface.

- *Can additional information from laser remote sensing resolve the ambiguity present in the estimation of a photoclinometric elevation model?*
  As noted in the subquestion above, trends are present in photoclinomtric estimations. These need to be solved, together with other geometric unknowns. However the topography of a glacier is dynamical, thus the temporal dimension should be taken into account. These accumulating unknowns and assumptions restrict the potential for elevation estimation. Additionally, the sampling of ICESat is to sparse in between lanes to resolve all unknowns.

- *Is photoclinometry capable of improving the information content of measurements from a spaceborne laser profiler?*
  Photoclinometry is dominant in information extraction along one dimension. A simple model was applied in this study, to correct laser profile measurements from miss-alignment from the reference track. However, a more improved model (area-based) may be more reliable.

Apart from conclusions derived from this work, there still lies potential both in the methods, as in its applications. The following ideas may be of interest for future research.

The area based photoclinometric estimation is very computer intensive. The configuration of the design matrix is very simple, most entities are close to the diagonal of the matrix. This arrangement can be an advantage to the computational speed through for example *Cholesky*-decomposition, as is done in Sparse bundle adjustment.

If the surface topography is known, the shading of this surface can be estimated. If this is normalized to an optical acquisition, the residue will also include the deviation

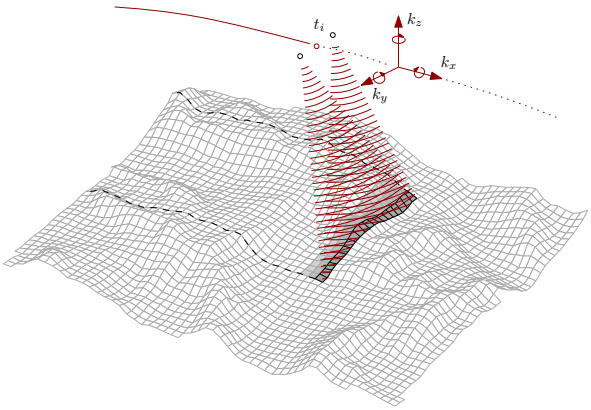

Figure 6.1: schematic view of the SIRAL-2 instrument on board of the CRYOSAT2 platform.

from the reflection function. One cause of this reflection is sastrugi. This residue has thus the potential to show a pattern in the local dominant wind direction. This information can give a better understanding of the accumulation patterns on dry ice sheets, as these receive most of their accumulation through wind transport.

As mentioned before, image matching is troublesome at the upper part of a glacier. And if contrast is not present, parallax measurements will fail. This drawback is accepted, and off-the-shelf photogrammetric products, like ASTER GDEM, keep some of these errors within their products. Photoclinometry can however be of use to adjust these errors and fill in the gaps where contrast is low.

Slopes profiles derived from ICESat GLAS have shown to be capable of estimating surface velocity [Marsh and Rack, 2012]. The method relies on undulations between footprints that are along the flightpath of the satellite. As the repeating passes are not following the exact pass, topographic structures that are not perpendicular, interfere the measurements. Thus these features are included into the equation, by a model of linear features, and consequentially result in an extra unknown. Photoclinometry could be of help for this method. The topographic knowledge reduces the unknowns, this makes the method more robust. If the terrain situation stays stable, it is likely that only one optical acquisition could already be sufficient.

In the field of microwave remote sensing the topographic information derived from photoclinometry can be useful for unwrapping. For example, CryoSat has the SIRAL-2 instrument on board. This instrument has a small baseline of two RADAR antennas. As the platform swaps over, it samples the terrain. The received signals is differenced and these phase changes make up an interferogram. Each strip will have it's own interferogram, being different from normal two dimensional unwrapping for imaging RADARs. However if information about the topography is known, this can help solving the ambiguities.

Clinometry can also be used for imaging RADAR, its mathematical footing was al-

ready laid out in the eighties [Wildey, 1988]. The accuracy of this method seems to have a similar quality as photoclinometry. Therefor, its benefit will lay in contributing information, helping in resolving inSAR mapping or interferometric unwrapping.

Bibliography

[Abdalati et al., 2010] Abdalati, W., Zwally, H., Bindschadler, R., Csatho, B., Farrell, S., Fricker, H., Harding, D., Kwok, R., Lefsky, M., Markus, T., et al. (2010). The icesat-2 laser altimetry mission. *Proceedings of the IEEE*, 98(5):735–751. [pg. 18]

[Beyer et al., 2003] Beyer, R., McEwen, A., and Kirk, R. (2003). Meter-scale slopes of candidate mer landing sites from point photoclinometry. *J. Geophys. Res*, 108:8085. [pg. 17]

[Bindschadler et al., 2011a] Bindschadler, R., Choi, H., Wichlacz, A., Bingham, R., Aberdeen, A., Bohlander, J., Brunt, K., Corr, H., Drews, R., Fricker, H., et al. (2011a). Getting around antarctica: new high-resolution mappings of the grounded and freely-floating boundaries of the antarctic ice sheet created for the international polar year. *The Cryosphere*, 5(3):569–588. [pg. 22, 44]

[Bindschadler et al., 2010] Bindschadler, R., Scambos, T., Choi, H., and Haran, T. (2010). Ice sheet change detection by satellite image differencing. *Remote Sensing of Environment*, 114(7):1353–1362. [pg. 21]

[Bindschadler et al., 2002] Bindschadler, R., Scambos, T., Rott, H., Skvarca, P., and Vornberger, P. (2002). Ice dolines on Larsen Ice Shelf, Antarctica. *Annals of Glaciology*, 34(1):283–290. [pg. 21, 44]

[Bindschadler and Vornberger, 1994] Bindschadler, R. and Vornberger, P. (1994). Detailed elevation map of ice stream c, antarctica, using satellite imagery and airborne radar. *Annals of Glaciology*, 20(1):327–335. [pg. 24, 41, 44, 57, 61]

[Bindschadler et al., 2011b] Bindschadler, R., Wichlacz, A., and Choi, H. (2011b). An illustrated guide to using asaid software. Technical report, NASA Antarctic Snow Accumulation and Ice Discharge project. [pg. 44, 66]

[Bingham and Rees, 1999] Bingham, A. and Rees, W. (1999). Construction of a high-resolution dem of an arctic ice cap using shape-from-shading. *International Journal of Remote Sensing*, 20(15):3231–3242. [pg. 21, 41, 61]

[Bolch et al., 2010] Bolch, T., Yao, T., Kang, S., Buchroithner, M., Scherer, D., Maussion, F., Huintjes, E., and Schneider, C. (2010). A glacier inventory for the western nyainqentanglha range and the nam co basin, tibet, and glacier changes 1976-2009. *Cryosphere*, 4(3):419–433. [pg. 53]

[Carabajal et al., 1999] Carabajal, C., Harding, D., Luthcke, S., Fong, W., Rowton, S., and Frawley, J. (1999). Processing of shuttle laser altimeter range and return pulse data in support of sla-02. *International Archives of Photogrammetry and Remote Sensing*, 32(3214):65–72. [pg. 11]

[Chander et al., 2009] Chander, G., Markham, B., and Helder, D. (2009). Summary of current radiometric calibration coefficients for landsat mss, tm, etm+, and eo-1 ali sensors. *Remote Sensing of Environment*, 113(5):893–903. [pg. 56]

[Choi and Bindschadler, 2004] Choi, H. and Bindschadler, R. (2004). Cloud detection in landsat imagery of ice sheets using shadow matching technique and automatic normalized difference snow index threshold value decision. *Remote sensing of environment*, 91(2):237–242. [pg. 40]

[Cogley et al., 2011] Cogley, J., Hock, R., Rasmussen, L., Arendt, A., Bauder, A., Braithwaite, R., Jansson, P., Kaser, G., Möller, M., Nicholson, L., and Zemp, M. (2011). Glossary of glacier mass balance and related terms. Technical Report 86, International Association of Cryospheric Sciences, UNESCO-IHP, Paris, France. [pg. 20]

[Cuffey and Paterson, 2010] Cuffey, K. and Paterson, W. (2010). *The physics of glaciers*. Academic Press. [pg. 1]

[Debella-Gilo and Kääb, 2012] Debella-Gilo, M. and Kääb, A. (2012). Measurement of surface displacement and deformation on mass movement using least squares matching of repeat images. *Remote Sensing*, 4:43–67. [pg. 20]

[den Ouden et al., 2008] den Ouden, M., Reijmer, C., and Oerlemans, J. (2008). Surface mass-balance modeling of nordenskiöldbreen, svalbard. In IMAU, editor, *The dynamics and mass budget of arctic glaciers*, pages 28–31. [pg. 59, 60]

[den Ouden et al., 2010] den Ouden, M., Reijmer, C., Pohjola, L., van de Wal, R., Oerlemans, J., and Boot, W. (2010). Stand-alone single-frequency gps ice velocity observations on nordenskiöldbreen, svalbard. *The Cryosphere*, 4(4):593–604. [pg. 54]

[Dowdeswell et al., 1985] Dowdeswell, J., Drewry, D., Cooper, A., Gorman, M., Liestøl, O., and Orheim, O. (1985). Digital mapping of the nordaustlandet ice caps from airborne geophysical investigations. *Annals of Glaciology*, 8:51–58. [pg. 63]

[Dowdeswell and Mc Intyre, 1987] Dowdeswell, J. and Mc Intyre, N. (1987). The surface topography of large ice masses from landsat imagery. *Journal of Glaciology*, 33(113):16–23. [pg. 21]

[Dowdeswell et al., 1999] Dowdeswell, J., Unwin, B., Nuttall, A., and Wingham, D. (1999). Velocity structure, flow instability and mass flux on a large arctic ice cap from satellite radar interferometry. *Earth and Planetary Science Letters*, 167(3):131–140. [pg. 63]

[Dozier, 1989] Dozier, J. (1989). Spectral signature of alpine snow cover from landsat thematic mapper. *Remote Sensing of Environment*, 28:9–22. [pg. 39, 40]

[Dozier and Outcalt, 1979] Dozier, J. and Outcalt, S. (1979). An approach toward energy balance simulation over rugged terrain. *Geographical Analysis*, 11(1):65–85. [pg. 36]

[Dozier and Painter, 2004] Dozier, J. and Painter, T. (2004). Multispectral and hyperspectral remote sensing of alpine snow properties. *Annual Review of Earth and Planetary Sciences*, 32:465–494. [pg. 16]

[Dumont et al., 2010] Dumont, M., Brissaud, O., Picard, G., Schmitt, B., Gallet, J., and Arnaud, Y. (2010). High-accuracy measurements of snow Bidirectional Reflectance Distribution Function at visible and NIR wavelengths–comparison with modelling results. *Atmospheric Chemistry and Physics*, 10:2507–2520. [pg. 13, 15]

[Dunse et al., 2011] Dunse, T., Schuler, T., Hagen, J., and Reijmer, C. (2011). Seasonal speed-up of two outlet glaciers of austfonna, svalbard, inferred from continuous gps measurements. *The Cryosphere Discuss*, 5:3423–3453. [pg. 63]

[Duong, 2010] Duong, H. (2010). *Processing and application of ICEsat large footprint full waveform laser range data*. TUDelft Phd Thesis. [pg. 11, 18]

[Etzelmüller, 2000] Etzelmüller, B. (2000). On the quantification of surface changes using grid-based digital elevation models (dems). *Transactions in GIS*, 4(2):129–143. [pg. 20]

[Frankot and Chellappa, 1988] Frankot, R. and Chellappa, R. (1988). A method for enforcing integrability in shape from shading algorithms. *Pattern Analysis and Machine Intelligence, IEEE Transactions on*, 10(4):439–451. [pg. 37, 47]

[Fricker et al., 2010] Fricker, H., Scambos, T., Carter, S., Davis, C., Haran, T., and Joughin, I. (2010). Synthesizing multiple remote-sensing techniques for subglacial hydrologic mapping: application to a lake system beneath macayeal ice stream, west antarctica. *Journal of Glaciology*, 56(196):187–199. [pg. 22]

[Fujisada et al., 2011] Fujisada, H., Urai, M., and Iwasaki, A. (2011). Advanced methodology for aster dem generation. *Geoscience and Remote Sensing, IEEE Transactions on*, (99):1–12. [pg. 51]

[Garvin et al., 1998] Garvin, J., Bufton, J., Blair, J., Harding, D., Luthcke, S., Frawley, J., and Rowlands, D. (1998). Observations of the earth's topography from the shuttle laser altimeter(sla): laser-pulse echo-recovery measurements of terrestrial surfaces. *Physics and Chemestry of the Earth*, 23(9):1053–1068. [pg. 18]

[Gorte, 2006] Gorte, B. (2006). *Advanced Remote Sensing: image processing*. Lectures notes Delft University of Technology, The Netherlands. [pg. 27]

[Hagen et al., 1993] Hagen, J., Liestøl, O., Roland, E., and Jørgensen, T. (1993). *Glacier atlas of Svalbard and Jan Mayen*. Number 129. Norsk polarinstitutt. [pg. 62]

[Harding and Carabajal, 2005] Harding, D. and Carabajal, C. (2005). Icesat waveform measurements of within-footprint topographic relief and vegetation vertical structure. *Geophysical research letters*, 32(21):L21S10. [pg. 18]

[Harvey, 1969] Harvey, D. (1969). *Explanation in geography*. Edward Arnold London. [pg. 29]

[Heid and Kääb, 2012] Heid, T. and Kääb, A. (2012). Evaluation of existing image matching methods for deriving glacier surface displacements globally from optical satellite imagery. *Remote Sensing of Environment*, 118:339–355. [pg. 58]

[Horn, 1990] Horn, B. (1990). Height and gradient from shading. *International Journal of Computer Vision*, 5(1):37–75. [pg. 17]

[Howat et al., 2008] Howat, I., Smith, B., Joughin, I., and Scambos, T. (2008). Rates of southeast greenland ice volume loss from combined icesat and aster observations. *Geophysical Research Letters*, 35(17):L17505. [pg. 22]

[Hunt et al., 2009] Hunt, W., Winker, D., Vaughan, M., Powell, K., Lucker, P., and Weimer, C. (2009). Calipso lidar description and performance assessment. *Journal of Atmospheric and Oceanic Technology*, 26(7):1214–1228. [pg. 11]

[Ikeuchi and Horn, 1981] Ikeuchi, K. and Horn, B. (1981). Numerical shape from shading and occluding boundaries. *Artificial Intelligence*, 17(1):141–184. [pg. 53]

[Immerzeel et al., 2010] Immerzeel, W., Van Beek, L., and Bierkens, M. (2010). Climate change will affect the asian water towers. *Science*, 328(5984):1382. [pg. 48]

[Jóhannesson and Raymond, 1989] Jóhannesson, T. and Raymond, C.F. andWaddington, E. (1989). Time-scale for adjustment of glaciers to changes in mass balance. *Journal Of Glaciology*, 35(121):355–369. [pg. 1]

[Kääb, 2005] Kääb, A. (2005). *Remote sensing of mountain glaciers and permafrost creep*, volume 48. Geographisches Institut der Universität Zürich. [pg. 8, 9, 10]

[Kääb, 2008] Kääb, A. (2008). Glacier volume changes using ASTER satellite stereo and ICESat GLAS laser altimetry. A test study on Edgeøya, Eastern Svalbard. *IEEE Transactions on Geoscience and Remote Sensing*, 46(10):2823–2830. [pg. 21, 59]

[Kang et al., 2009] Kang, S., Chen, F., Gao, T., Zhang, Y., Yang, W., Yu, W., and Yao, T. (2009). Early onset of rainy season suppresses glacier melt: a case study on zhadang glacier, tibetan plateau. *Journal of Glaciology*, 55(192):755–758. [pg. 48]

[Kirk, 1987] Kirk, R. (1987). *A fast finite-element algorithm for two-dimensional photoclinometry*. California Institute of Technology Phd Thesis. [pg. 5]

[Klees, 2009] Klees, R. (2009). *Reference and Coordinate Systems*. Lectures notes Delft University of Technology, The Netherlands. [pg. 31, 34]

[Krimmel, 1999] Krimmel, R. (1999). Analysis of difference between direct and geodetic mass balance measurements at south cascade glacier, washington. *Geografiska Annaler: Series A, Physical Geography*, 81(4):653–658. [pg. 20]

[Kropáček et al., 2010] Kropáček, J., Feng, C., Alle, M., Kang, S., and Hochschild, V. (2010). Temporal and spatial aspects of snow distribution in the nam co basin on the tibetan plateau from modis data. *Remote Sensing*, 2(12):2700–2712. [pg. 49]

[Lavallée, 2005] Lavallée, D. (2005). *Inverse problems, sequential and step by step least squares methods*. Lectures notes Delft University of Technology, The Netherlands. [pg. 30]

[Leclercq et al., 2011] Leclercq, P., Oerlemans, J., and Cogley, J. (2011). Estimating the glacier contribution to sea-level rise for the period 1800–2005. *Surveys in Geophysics*, pages 1–17. [pg. 2]

[Lemke et al., 2007] Lemke, P., Ren, J., Alley, R., Allison, I., Carrasco, J., Flato, G., Fujii, Y., Kaser, G., Mote, P., Thomas, R., et al. (2007). Observations: changes in snow, ice and frozen ground. *Climate change*, pages 337–383. [pg. 1, 2]

[Madsen and Tingleff, 2004] Madsen, K. Nielsen, H. and Tingleff, O. (2004). *Methods for non-linear least squares problems*. Lectures Notes IMM Technical University of Denmark. [pg. 28, 29, 83]

[Marsh and Rack, 2012] Marsh, O. and Rack, W. (2012). A method of calculating ice-shelf surface velocity using icesat altimetry. *Polar Record*, 48(1):25–30. [pg. 69]

[Martin et al., 2005] Martin, C., Thomas, R., Krabill, W., and Manizade, S. (2005). Icesat range and mounting bias estimation over precisely-surveyed terrain. *Geophys. Res. Lett*, 32(21). [pg. 18]

[McEwen, 1991] McEwen, A. (1991). Photometric functions for photoclinometry and other applications. *Icarus*, 92(2):298–311. [pg. 33]

[Milman, 1999] Milman, A. (1999). *Mathematical principles of remote sensing: making inferences from noisy data*. CRC. [pg. 29]

[Moholdt et al., 2010a] Moholdt, G., Hagen, J., Eiken, T., and Schuler, T. (2010a). Geometric changes and mass balance of the austfonna ice cap, svalbard. *the Cryosphere*, 4:21–34. [pg. 5]

[Moholdt and Kääb, 2012] Moholdt, G. and Kääb, A. (2012). A new dem of the austfonna ice cap by combining differential sar interferometry with icesat laser altimetry. *Polar Research*, 31:18460. [pg. 63]

[Moholdt et al., 2010b] Moholdt, G., Nuth, C., Hagen, J., and Kohler, J. (2010b). Recent elevation changes of svalbard glaciers derived from icesat laser altimetry. *Remote Sensing of Environment*. [pg. 5, 21, 22, 41, 61]

[Molijn et al., 2011] Molijn, R., Lindenbergh, R., and Gunter, B. (2011). Icesat laser full waveform analysis for the classification of land cover types over the cryosphere. *International Journal of Remote Sensing*, 32(23):8799–8822. [pg. 18]

[Mondet and Fily, 1999] Mondet, J. and Fily, M. (1999). The reflectance of rough snow surfaces in antarctica from polder/adeos remote sensing data. *Geophysical Research Letters*, 26(23):3477–3480. [pg. 15]

[Nuth et al., 2010] Nuth, C., Moholdt, G., Kohler, J., Hagen, J., and Kääb, A. (2010). Svalbard glacier elevation changes and contribution to sea level rise. *Journal of Geophysical Research*, 115:2003–2008. [pg. 21]

[Nuth et al., 2012] Nuth, C., Schuler, T., Kohler, J., Altena, B., and Hagen, J. (2012). Estimating the long-term calving flux of kronebreen, svalbard, from geodetic elevation changes and mass-balance modelling. *Journal of Glaciology*, 58(207):119–133. [pg. 19]

[Paterson, 1994] Paterson, W. (1994). *The physics of glaciers*. Elsevier. [pg. 19]

[Paul, 2011] Paul, F. (2011). Automated glacier mapping. In Singh, P. and Haritashya, U., editors, *Encyclopedia of Snow, Ice and Glaciers*, pages 76–83. Springer. [pg. 2]

[Peltoniemi et al., 2005] Peltoniemi, J., Kaasalainen, S., Näränen, J., Matikainen, L., and Piironen, J. (2005). Measurement of directional and spectral signatures of light reflectance by snow. *Geoscience and Remote Sensing, IEEE Transactions on*, 43(10):2294–2304. [pg. 14, 16]

[Polman and Salzmann, 1996] Polman, J. and Salzmann, M. (1996). *Handleiding voor de Technische Werkzaamheden van het Kadaster*. Kadaster, Apeldoorn, the Netherlands. [pg. 2, 34]

[Pope, 2009] Pope, A. (2009). *Recent changes to Langjökull icecap, Iceland: an investigation integrating airborne LiDAR and satellite imagery*. University of Cambridge, Msc Thesis. [pg. 44, 61]

[Pritchard et al., 2009] Pritchard, H., Arthern, R., Vaughan, D., and Edwards, L. (2009). Extensive dynamic thinning on the margins of the greenland and antarctic ice sheets. *Nature*, 461(7266):971–975. [pg. 21]

[Ramond et al., 2011] Ramond, T., Saiki, E., Weimer, C., Applegate, J., Hu, Y., Delker, T., Ruppert, L., and Donley, B. (2011). Topographic mapping flash lidar for multiple scattering, terrain, and forest mapping. In *Proceedings of SPIE*, volume 8037, page 803710. [pg. 19]

[Ranson and Daughtry, 1987] Ranson, J. and Daughtry, C. (1987). Scene shadow effects on multispectral response. *Geoscience and Remote Sensing, IEEE Transactions on*, 25(4):502–509. [pg. 39]

[Raup et al., 2000] Raup, B., Kieffer, H., Hare, T., and Kargel, J. (2000). Generation of data acquisition requests for the aster satellite instrument for monitoring a globally distributed target: glaciers. *IEEE transactions on Geosciences and Remote Sensing*, 38(2):1–10. [pg. 3]

[Raup et al., 2005] Raup, B., Scambos, T., and Haran, T. (2005). Topography of streaklines on an Antarctic ice shelf from photoclinometry applied to a single Advanced Land Imager (ALI) image. *Geoscience and Remote Sensing, IEEE Transactions on*, 43(4):736–742. [pg. 21]

[Rees, 2001] Rees, W. (2001). *Physical principles of remote sensing*. Cambridge University Press. [pg. 12, 32]

[Rees, 2006] Rees, W. (2006). *Remote sensing of snow and ice*. CRC. [pg. 13]

[Rees and Dowdeswell, 1988] Rees, W. and Dowdeswell, J. (1988). Topographic effects on light scattering from snow. In *ESA, Proceedings of the International Geoscience and Remote Sensing symposium on Remote Sensing: Moving towards the 21st Century*, volume 1. [pg. 21]

[Richter, 1998] Richter, R. (1998). Correction of satellite imagery over mountainous terrain. *Applied Optics*, 37(18):4004–4015. [pg. 21]

[Rotschky et al., 2011] Rotschky, G., Schuler, T., Haarpaintner, J., Kohler, J., and Isaksson, E. (2011). Spatio-temporal variability of snowmelt across svalbard during the period 2000-08 derived from quikscat/seawinds scatterometry. *Polar Research*, 30. [pg. 59]

[Sagan, 1992] Sagan, H. (1992). *Introduction to the Calculus of Variations*. Dover Pubns. [pg. 17]

[Sauber et al., 2005] Sauber, J., Molnia, B., Carabajal, C., Luthcke, S., and Muskett, R. (2005). Ice elevations and surface change on the malaspina glacier, alaska. *Geophysical Research Letters*, 32:23. [pg. 21]

[Scambos and Fahnestock, 1998] Scambos, T. and Fahnestock, M. (1998). Improving digital elevation models over ice sheets using AVHRR-based photoclinometry. *Journal of Glaciology*, 44(146):97–103. [pg. 21]

[Scambos and Haran, 2002] Scambos, T. and Haran, T. (2002). An image-enhanced DEM of the Greenland Ice Sheet. *Annals of Glaciology*, 34(1):291–298. [pg. 21]

[Schenk et al., 2005] Schenk, T., Csatho, B., Van der Veen, C., Brecher, H., Ahn, Y., and Yoon, T. (2005). Registering imagery to icesat data for measuring elevation changes on byrd glacier, antarctica. *Geophysical research letters*, 32(23):L23S05. [pg. 22]

[Slobbe et al., 2008] Slobbe, D., Lindenbergh, R., and Ditmar, P. (2008). Estimation of volume change rates of greenland's ice sheet from icesat data using overlapping footprints. *Remote Sensing of Environment*, 112(12):4204–4213. [pg. 5, 21, 41, 42, 59]

[Steffen, 1987] Steffen, K. (1987). Bidirectional reflectance of snow at 500–600 nm. *Large-Scale Effects of Seasonal Snow Cover*, pages 415–425. [pg. 14]

[Stilla and Jutzi, 2009] Stilla, U. and Jutzi, B. (2009). Waveform analysis for small-footprint pulsed laser systems. In Shan, J. and Koth, C., editors, *Topographic laser ranging and scanning: principles and processing*, pages 215–234. Springer. [pg. 11]

[Strang and Borre, 1997] Strang, G. and Borre, K. (1997). *Linear algebra, geodesy and GPS*. Wellesley-Cambridge Press. [pg. 25]

[Strang van Hees, 2006] Strang van Hees, G. (2006). *Globale en lokale geodetische systemen*. Nederlandse Commissie voor Geodesie. [pg. 43]

[Tachikawa et al., 2011] Tachikawa, T., Kaka, M., Iwasaki, A., Gesch, D., Oimoen, M., Zhang, Z., Danielson, J., Krieger, T., Curtis, B., Haase, J., Abrams, M., Crippen, R., and Carabajal, C. (2011). Aster global digital elevation model version 2. Technical report, ASTER GDEM validation team. [pg. 51]

[Teunissen, 1985] Teunissen, P. (1985). *The geometry of geodetic inverse linear mapping and non-linear adjustment*. Rijkscommissie voor geodesie. [pg. 30]

[Teunissen, 2003] Teunissen, P. (2003). *Adjustment theory*. DUP Blue Print. [pg. 28]

[Teunissen et al., 2005] Teunissen, P., Simons, D., and Tiberius, C. (2005). *Probability and observation theory*. Lectures notes Delft University of Technology, The Netherlands. [pg. 26]

[Thome et al., 1998] Thome, K., Palluconi, F., Takashima, T., and Masuda, K. (1998). Atmospheric correction of aster. *Geoscience and Remote Sensing, IEEE Transactions on*, 36(4):1199–1211. [pg. 56]

[van Pelt et al., 2012] van Pelt, W., Oerlemans, J., Reijmer, C., Pohjola, V., Pettersson, R., and van Angelen, J. (2012). Simulating melt, runoff and refreezing on nordenskiöldbreen, svalbard, using a coupled snow and energy balance model. *The Cryosphere Discussions*, 6:211–266. [pg. 54]

[Vermeer, 2010] Vermeer, M. (2010). *Statistical methods in geodesy*. Lectures notes Helsinki University of Technology, Finland. [pg. 27]

[Wackernagel, 2003] Wackernagel, H. (2003). *Multivariate geostatistics: an introduction with applications*. Springer Verlag. [pg. 44]

[Warren, 1982] Warren, S. (1982). Optical properties of snow. *Reviews of geophysics and space physics*, 20(1):67–89. [pg. 13, 14]

[Warren et al., 1998] Warren, S., Brandt, R., and Hinton, P. (1998). Effect of surface roughness on bidirectional reflectance of Antarctic snow. *Journal of Geophysical Research*, 103(E11):25789–25807. [pg. 15]

[Weisstein, 2012] Weisstein, E. (2012). Fourier series - triangle wave. `http://mathworld.wolfram.com/FourierSeriesTriangleWave.html`. MathWorld - a Wolfram web resource [accessed 14-May-2012]. [pg. 42, 59]

[Wildey, 1988] Wildey, R. (1988). Radarclinometry: bootstrapping the radar reflectance function from the image pixel-signal frequency distribution and an altimetry profile. *Earth, Moon, and Planets*, 41(3):223–240. [pg. 70]

[Wiscombe and Warren, 1980] Wiscombe, W. and Warren, S. (1980). A model for the spectral albedo of snow. i: Pure snow. *Journal of the Atmospheric Sciences*, 37(12):2712–2733. [pg. 12]

[Young et al., 1995] Young, I., Gerbrands, J., and Van Vliet, L. (1995). *Fundamentals of image processing*. Delft University of Technology. [pg. 23]

[Zhang et al., 2011] Zhang, G., Xie, H., Kang, S., Yi, D., and Ackley, S. (2011). Monitoring lake level changes on the tibetan plateau using icesat altimetry data (2003-2009). *Remote Sensing of Environment*. [pg. 18]

[Zhou et al., 2003] Zhou, X., Li, S., and Stamnes, K. (2003). Effects of vertical inhomogeneity on snow spectral albedo and its implication for optical remote sensing of snow. *Journal of Geophysical Research*, 108(4738):10–1029. [pg. 14]

Postface & acknowledgments

For me, the start of the summer is home to a classic bicycle race. This race is held since the 1970's, and takes the competitors from Utrecht to Freyr. The 270 or so kilometers, start in the county of '*Maas & Waal*', and end in the hilly slopes of the '*Ardennes*'. The finish is on the top of the hill, where '*Chamonix*' is situated, the local pub.

Completing this race is an accomplishment, and the barbecue is well deserved. Although every year their are people that fail, it is not extraordinary accomplishment to accomplish. With some training and good luck, one will bike to the rocks of Freyr.

Thus why do I participate? The answer can be found somewhere early spring 2010. Rob and I are welding, grinding, sanding and assembling for more than a day. We found a cool bicycle design, and want to build the vehicle ourself. A bicycle is topped from its steering wheel, and its saddle is demolished. At each side comes a new steering wheel and saddle. Thus the vehicle is used as a tandem, but the alignment is ext to each other. This construction was later on crowned to '*duocapide*'. And together with my brother I attempted the adventure to reach Freyr.

This is just a short anecdote of an wonderful adventure. Its outcome is unknown, and success is not guaranteed. Another adventure is written down in the pages former

to this one. It is a journey I did not make alone, therefor I want to acknowledge some of the people that made this journey worthwhile.

At first, and foremost I want to thank Ben for being my daily supervisor. The weekly meetings gave me insights or despair. The opportunity to go on fieldwork to Tibet was of great value to me. And it was an honor to be one of Massimo's *picciotti*. The conversations with Andreas in Oslo gave more insights into the subject and implementation of my thesis. Chris forced me to look outside the box, brought in nice directions and humor.

Another source of happiness in the office was brought by Pierre-Marie. But most of the good times were spent with the Bavarian, Tobias. Sergi gave me distraction with his wonderful talk during running trips through the forest. And his awesome cooking, from reindeer burger up to octopus on campfire.

Other good cooking and running was provided by Piet, back in Utrecht. But the early mornings with Ineke really put me through this adventure. Especially our, or my enforced, experiment in the applicability of Bayes rule and early morning coffee, were of great enjoyment, at least to me. Other distraction was provided by the neighbors of *Buurland* and my alpine friends of *Vertical Dissidents*. The tedious job of correcting most of my English grammar was done by Kim, I surely owe her a lukewarm pint. Esther gave me clear insights and distraction in the last phase of the thesis, which was needed.

Finally, the support from my parents during my master was of great importance, their encouragement and advice were highly appreciated. Furthermore, the love and involvement of my sister helped me through this adventure. But also notified me of more important things then punching buttons. While my brother distracted me by physically finding our limits in climbing, running, biking and unfortunately inline-skating.

postscript: This years attempt to Freyr was again a failure, hopefully this thesis adventure will head to another direction.

Appendix A

Algorithms & Maps

Algorithm 1 Shading function

function SHADING($\mathbf{H}$, $\vec{s}$, spacing)
  $\mathbf{dX}_{\text{left}} = \mathbf{H}(all, 1 : end - 1) - \mathbf{H}(all, 2 : end)$
  $\mathbf{dX}_{\text{right}} = \mathbf{H}(all, 1) - \mathbf{H}(all, 2)$
  $\mathbf{gX} = [\mathbf{dX}_{\text{left}} \quad \mathbf{dX}_{\text{right}}]$ ▷ gradient along x
  $\mathbf{dY}_{\text{up}} = \mathbf{H}(2 : end, all) - \mathbf{H}(1 : end - 1, all)$
  $\mathbf{dY}_{\text{down}} = \mathbf{H}(2, all) - \mathbf{H}(1, all)$
  $\mathbf{gY} = [\mathbf{dY}_{\text{up}}; \quad \mathbf{dY}_{\text{down}}]$ ▷ gradient along y
  $\mathbf{gZ} = \text{spacing} \times \mathbf{1}$
  $\mathbf{Nx} = \mathbf{gX}/\sqrt{\mathbf{gX}^2 + \mathbf{gY}^2 + \mathbf{gZ}^2}$
  $\mathbf{Ny} = \mathbf{gY}/\sqrt{\mathbf{gX}^2 + \mathbf{gY}^2 + \mathbf{gZ}^2}$
  $\mathbf{Nz} = \mathbf{gZ}/\sqrt{\mathbf{gX}^2 + \mathbf{gY}^2 + \mathbf{gZ}^2}$ ▷ components of normal vector
  dotProduct $= \cos^{-1}(\mathbf{Nx} \cdot \vec{s}_1 + \mathbf{Ny} \cdot \vec{s}_2 + \mathbf{Nz} \cdot \vec{s}_3)$
  return dotProduct
end function

$\vec{s}$	sun vector
ψ	azimuth of the sun
$\mathbf{C}$	relational matrix
$\mathbf{E}$	shading
$\vec{x}_0$	initial estimation

Table A.1: Description of input parameters for algorithm 2 and 3

Algorithm 2 Estimate curvature perpendicular to sun direction

function KERNEL2SUN($\vec{s}$)
  $\psi = atan2(\vec{s}_y, \vec{s}_x)$ ▷ $-\pi < atan2(y, x) \leq \pi$
  $\vec{\phi} = -\pi, \quad \frac{\pi}{9}, \quad \pi$ ▷ compass rose of kernel
  $\vec{w} = 1 - \|(\vec{\phi} - \theta)/\frac{\pi}{9}\|$ ▷ weight
  $\mathbf{K}(i) = \vec{w}(i)$ ▷ create kernel
  for $n = 1, 9$ **do**
    $[\Delta x, \Delta y] = \|\vec{p}_{K(n)} - \vec{p}_{K(5)}\|$ ▷ deviation from middle
    for *row* $= 2, \quad \text{LENGTH}\{E\} - 1$ **do**
      for *col* $= 2, \quad \text{DEPTH}\{E\} - 1$ **do**
        $\mathbf{C}(row + \Delta x, col + \Delta y) = \mathbf{K}(n)$
      end for
    end for
  end for
  return $\mathbf{C}$
end function

$\mathbf{E}$	shading
dL	gridspacing
$\vec{s}$	sun vector
$\mathbf{L}$	ICESat GLAS coordinates

Table A.2: Description of input parameters for algorithm 4 and 5

Algorithm 3 Levenbergh-Marquardt algorithm, based on [Madsen and Tingleff, 2004]

procedure LEVMAR($\mathbf{E}$, $\vec{s}$, $\vec{x}_0$)
  ▷ initialization
  $\mathbf{C} = \text{KERNEL2SUN}(\vec{s})$ ▷ constrain on curvature
  $\partial\mathbf{A} = [\mathbf{J};\quad \mathbf{C}]$
  $\mathbf{W} = [\mathbf{I};\quad \alpha\mathbf{I}]$ ▷ weights
  $\partial^2\mathbf{A} = \partial\mathbf{A}^\top\mathbf{W}\partial\mathbf{A}$
  $\Delta\vec{y} = \mathbf{A}^\top\mathbf{W}f(\vec{x}_0);$ ▷ $\Delta\vec{y} \equiv \vec{y}_0$, linear approximation of shading
  $\mathbf{P} = \mathbf{A}(\mathbf{A}^\top\mathbf{Q}_{\underline{yy}}^{-1}\mathbf{A})^{-1}\mathbf{A}\mathbf{Q}_{\underline{yy}}^{-1}$ ▷ projection matrix
  $\delta_1 =? \leftarrow \mathbf{Q}_{\underline{\hat{y}\hat{y}}} = \mathbf{P}\mathbf{Q}_{\underline{yy}}\mathbf{P}^\top$
  $k = 0 \quad \upsilon = 2$
  found $= (\|\Delta\vec{y}\| \leq \delta_1);$
  $\mu = \tau \cdot max\{diag\{\partial^2\mathbf{A}\}\}$
  while (**not** *found*) **and** ($k < k_{max}$) **do** ▷ start iteration
    $k = k + 1$ ▷ counter
    $S_{lm} = \mu\mathbf{I}$ ▷ scaling matrix
    $\partial\mathbf{A} = [\partial\mathbf{A};\quad S_{lm}]$
    $\Delta\vec{y} = [f(x_k);\quad \mathbb{0}]$
    $\mathbf{W} = [\mathbf{I};\quad \alpha\mathbf{I};\quad \mathbf{I}]$
    $\mathbf{Q}_{\underline{\hat{x}\hat{x}}} = (\partial\mathbf{A}^\top\mathbf{Q}_{\underline{yy}}^{-1}\partial\mathbf{A})^{-1}$ ▷ estimate dispersion matrix
    $\Delta\vec{x} = (\partial\mathbf{A}^\top\mathbf{W}\partial\mathbf{A})^{-1}\partial\mathbf{A}^\top\mathbf{W}\Delta\vec{y}$ ▷ weighted least squares
    $\vec{\delta_2} = \text{diag}\{\mathbf{Q}_{\underline{\hat{x}\hat{x}}}\}$
    if $\|\Delta\vec{x}\| \leq \|\vec{\delta_2}(\vec{x}_k + \vec{\delta_2})\|$ **then**
      found $=$ **true**
    else
      $\vec{x}_n = \vec{x}_k + \Delta\vec{x}$ ▷ new estimation
      $F(\vec{x}_n) = f(\vec{x}_n)^\top f(\vec{x}_n)$
      $L(\vec{x}_n) = F(\vec{x}_n) + \mathbf{J}\Delta\vec{x} + \frac{1}{2}\Delta\vec{x}^\top\mathbf{H}\Delta\vec{x}$ ▷ Taylor expansion
      $\varrho = \frac{F(\vec{x_i}) - F(\vec{x}_n)}{L(0) - L(\Delta\vec{x}_n)}$ ▷ gain
      if $\varrho > 0$ **then**
        $x_k = x_n$
        update $\quad \mathbf{J} \quad \mathbf{A} \quad \Delta\vec{y} \quad \alpha$ ▷ with respect to the new estimate
        found $= (\|\Delta\vec{y}\| \leq \delta_1);$
        $\mu = \mu \quad max\{\frac{1}{3}, 1 - (2\varrho - 1)^3\}$
        $\upsilon = 2$
      else
        $\mu = \mu\upsilon \quad \upsilon = 2\upsilon$ ▷ steeper descent
      end if
    end if
  end while
  return x_k
end procedure

Algorithm 4 Topographic correction

procedure CROSSINGESTIMATE($\mathbf{E}$, dL, $\vec{s}$, $\vec{L}_x$, $\vec{L}_y$, $\vec{L}_z$)
  $crossing$ = INTERSECT($\vec{L}_x, \vec{L}_y$) ▷ crossing of two polylines
  $crossPoints$ = KNN($crossing, \vec{L}_x, \vec{L}_y$) ▷ k-Nearest-Neighbor
  $\vec{L}_\psi$ = ORIENTATION($crossing, \vec{L}_x, \vec{L}_y$) ▷ bearing with crossing
  $\psi_{\vec{s}}$, $\varphi_{\vec{s}}$ = ORIENTATION($\vec{s}$)
  for $i = 1 \ldots$ SIZE($crossPoints$) **do**
    $trackIntersect$ = INTERSECT($\vec{L}_x, \vec{L}_y, crossPoints_i, \psi_{\vec{s}}$)
    $\vec{S}_{x,y}$ = SPACING($trackIntersect, crossPoints_i, dL$)
    $\vec{E}_{x,y}$ = KRIGING($\mathbf{E}$, $\vec{S}_{x,y}$) ▷ interpolate shading values
    $\vec{H}_{1\ldots2}$ = BILINEAR($\vec{L}_z$, $\vec{L}_x$, $\vec{L}_y$) ▷ ICESat GLAS elevations
    stack $\vec{S}_{x,y}$ $\vec{E}_{x,y}$ $\vec{H}_{x,y}$
  end for
  f = clinoLane(A, B, $\vec{E}_{x,y}$ $\vec{H}_{x,y}$, $\varphi_{\vec{s}}$, dL)
  A, B = MINIMIZE($f(A$, $B)$)
  return A, B
end procedure

Algorithm 5 Estimate curvature perpendicular to sun direction

function CLINOLANE(A, B, $\vec{E}$, $\vec{H}$, φ, dL)
  for do$i = 1 \ldots$ SIZE(lanes)
    dZ = SUM(tan($\frac{\pi}{2} - \varphi + \cos^{-1}((A \cdot E_{i,:})\ B)) \cdot dL$)
    $dH = H_{i,1} - H_{i,2}$
  end for
  error $= dZ - dH$
  return error
end function

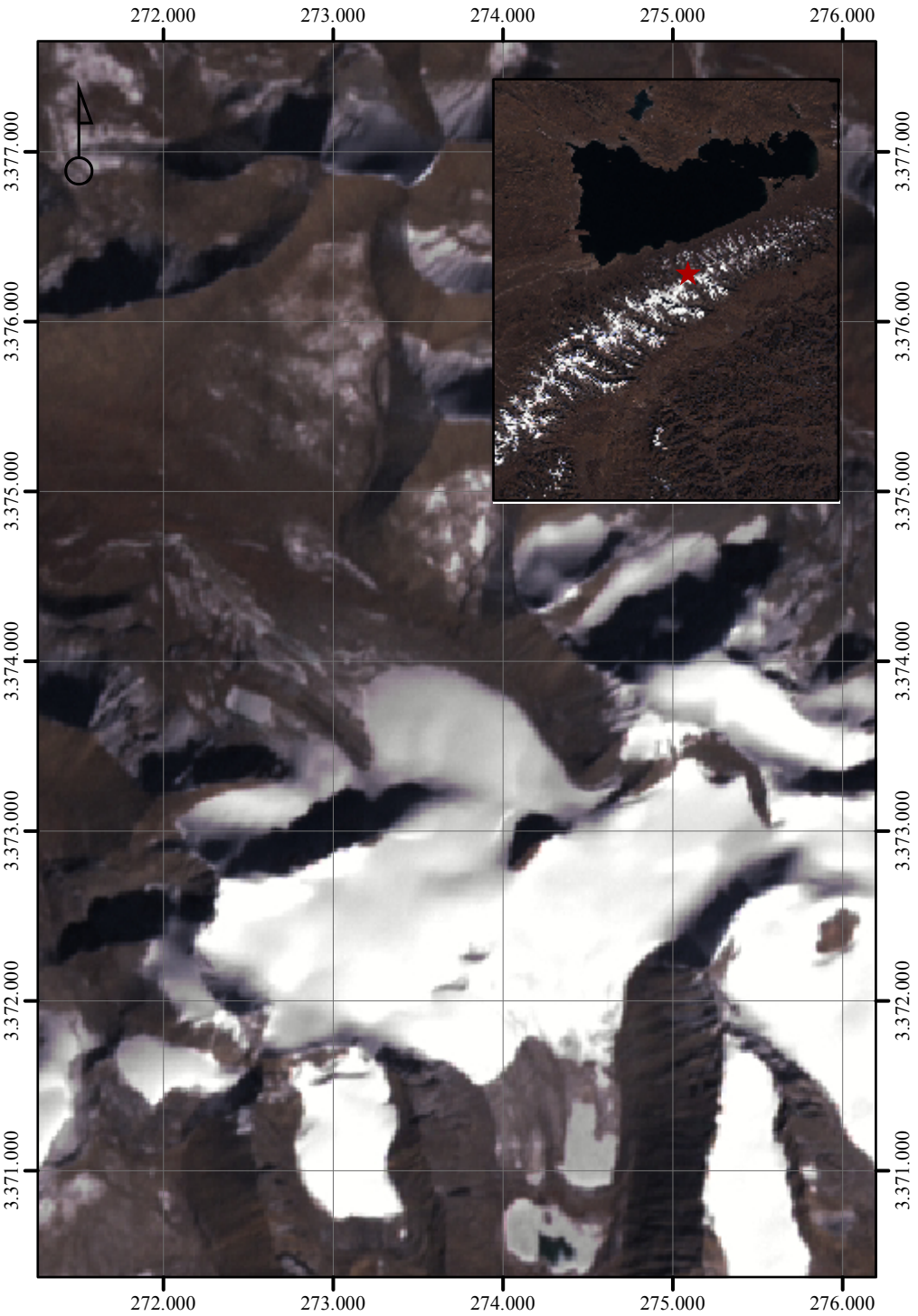

Figure A.1: *inset*) Color composite of Landsat ETM+ acquisition over Nyainqêntanglha mountain range, Tibetan plateau. The red star indicates the project area. *main*) Map of Zhadang glacier of Landsat ETM+ on November 17, 2001. The UTM grid has a spacing of one by one kilometer.

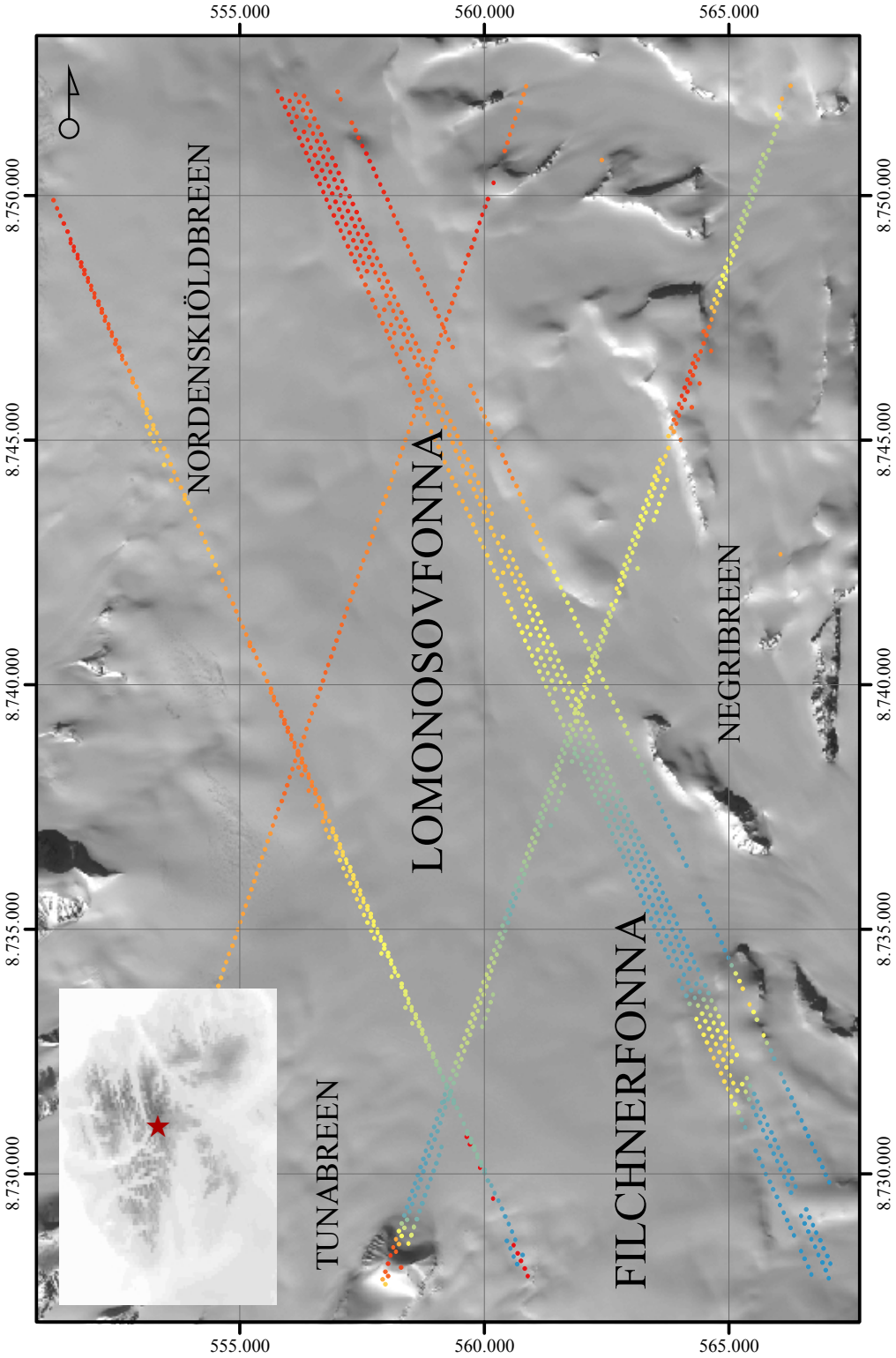

Figure A.2: *inset*) Elevation plot of the Svalbard peninsula, with an indication of the project area by a red star. *main*) Panchromatic acquisition over Lomonosovfonna from the EO1 ALI instrument on November 14, 2007. A selection of ICESat GLAS measurements are draped over the imagery, where the color is related to elevation (low, high). The UTM grid has a spacing of five by five kilometer.

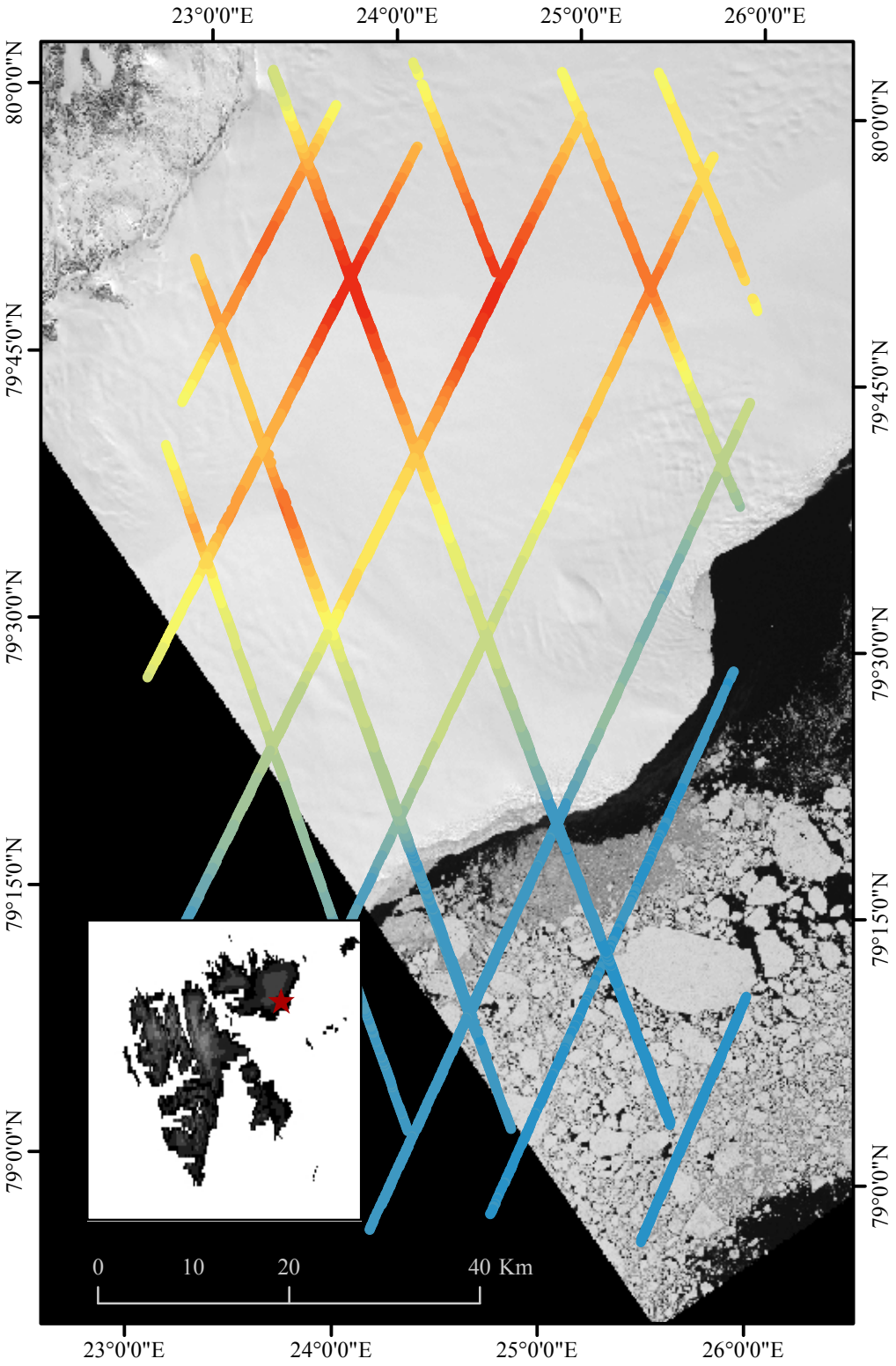

Figure A.3: *inset*) Elevation plot of the Svalbard peninsula, with an indication of the project area by a red star. *main*) Landsat ETM+ acquisition over Austfonna, with Basin-3 in the middle. The imagery was taken on June 17, 2001. A selection of ICESat GLAS measurements are draped over the imagery, where the color is related to elevation (low, high).